UNIVERSITY OF CALIFORNIA

SANTA CRUZ

CONTROLS ON PRIMARY PRODUCTIVITY AND ITS MEASUREMENT IN COASTAL UPWELLING SYSTEMS

A dissertation submitted in partial satisfaction
of the requirements for the degree of

DOCTOR OF PHILOSOPHY

in

OCEAN SCIENCES

by

Michael Geoffrey Jacox

September 2012

The Dissertation of Michael G. Jacox
is approved:

_____
Professor Christopher A. Edwards, Chair

_____
Professor Raphael M. Kudela

_____
Professor Jonathan P. Zehr

_____
Dr. John P. Ryan

_____
Tyrus Miller
Vice Provost and Dean of Graduate Studies

TABLE OF CONTENTS

ABSTRACT

CONTROLS ON PRIMARY PRODUCTIVITY AND ITS MEASUREMENT IN COASTAL UPWELLING SYSTEMS

by

Michael Geoffrey Jacox

Eastern Boundary Current systems, running along the west coasts of Africa and the Americas, are among the most biologically productive oceanic ecosystems. Their disproportionately large contributions to global marine primary productivity (photosynthesis) and fish catch are supported by upwelling of deep, nutrient rich water, a process driven by the interaction of surface winds and Earth's rotation. Upwelling in these systems may be forced by two mechanisms: equatorward winds at the coastal boundary (coastal divergence), or a cross-shore gradient in the magnitude of winds (wind stress curl). Though bulk estimates of upwelled volume and the individual contributions of coastal divergence and wind stress curl have been estimated, their roles in regulating productivity remain unclear. Similarly, while nutrient supply from upwelling has been measured or modeled in specific regions, its dependence on variability in physical factors including topography, stratification, and latitude has not been adequately addressed. The measurement of primary productivity itself is laborious and complicated *in situ*, and satellite-borne ocean color sensors currently represent our best option for obtaining the large-scale estimates needed to

constrain global carbon budgets. However, after over a quarter century of satellite primary productivity model development, performance has improved little.

The research in this dissertation employs a suite of cutting edge oceanographic tools – computer models, satellite sensors, and autonomous underwater platforms – to elucidate controls on primary productivity and its measurement in coastal upwelling systems. First, an idealized numerical model is used to evaluate the respective roles of stratification, continental shelf topography, latitude, and wind stress magnitude on upwelling source depth and nutrient delivery to the sunlit surface layer (Chapter 1). Next, this analysis is extended to investigate the impact of nearshore reduction in surface wind stress, a poorly constrained process with significant implications for bottom-up control of phytoplankton growth (Chapter 2). Finally, an extensive record of shipboard observations off the California Coast is analyzed to evaluate limitations on primary productivity estimation, and synergistic use of satellites with autonomous underwater gliders is identified as fertile ground for improvement (Chapter 3).

ACKNOWLEDGEMENTS

First, I would like to extend an enormous thank you to my Ph.D. advisor, Dr. Christopher Edwards. Regardless of my state going in, I always left his office with fresh ideas and optimism, which I think is the hallmark of a great mentor. He has continually encouraged, supported, and challenged me, for which I am forever grateful. He is a top-notch scientist, and one I eagerly anticipate counting among my colleagues.

I must also express a heartfelt thanks to the rest of my Ph.D. committee. Dr. Raphael Kudela enabled me to pursue interests outside of my core thesis research, and in doing so broadened both my understanding and curiosity about the oceans we study. Dr. Jonathan Zehr and Dr. John Ryan were there with open doors whenever called upon, and both offered perspectives and insight that strengthened both the work in this thesis and my abilities as a researcher.

Many thanks to my office mates, to the Edwards and Kudela lab groups, and to the PDP community for conversations both science and otherwise, and for company through the last four years. And to friends in Santa Cruz, Colorado, and beyond - running partners, climbing partners, roommates and bandmates - for helping me keep a balance in life.

Thanks to my family, as diverse in interests as in geography, for your support whether direct or otherwise. You've all taught me a lot and guided this journey in your own way.

And finally to Jenny, the best supporter and advocate one could ever hope for. For motivation, inspiration, love and companionship extending from the office to the trails and beyond - endless thanks.

The text of this dissertation includes reprints of the following previously published materials:

Jacox, M. G., and C. A. Edwards (2011), Effects of stratification and shelf slope on nutrient supply in coastal upwelling regions, J. Geophys. Res., 116, C03019, doi:10.1029/2010JC006547.

Jacox, M. G., and C. A. Edwards (2012), Upwelling source depth in the presence of nearshore wind stress curl, J. Geophys. Res., 117, C05008, doi:10.1029/2011JC007856.

The co-author (Edwards) listed in these publications directed and supervised the research which forms the basis for the dissertation.

DISSERTATION INTRODUCTION

At the eastern edge of ocean basins (i.e. along the western coasts of North America, South America, and Africa), cold water is carried equatorward in wide, slow-moving currents called Eastern Boundary Currents (EBCs). Through all or part of the year, for example in the spring and summer off the US west coast, these regions are associated with strong equatorward winds produced by land-sea air pressure gradients. Due to the rotation of the Earth and associated Coriolis acceleration, near-surface water is transported away from the coast during these times (to the right of the wind stress direction in the northern hemisphere, to the left in the southern hemisphere), a process known as Ekman transport. Cold, dense water from depth replaces the offshore flowing surface water, carrying with it nitrate, phosphate, and other nutrients vital to biological growth. Phytoplankton, the microscopic organisms that comprise the base of the marine food web, take advantage of this light- and nutrient-replete environment to photosynthesize and proliferate, making coastal upwelling ecosystems some of the most biologically productive oceanic regimes. Though they constitute less than 1% of the ocean's total area, these regions account for nearly 20% of global fish catch (Pauly and Christensen, 1995). It is no surprise then, that coastal upwelling is of great environmental and economic interest and has been the focus of much oceanographic research.

The upwelling mechanism described above, Ekman transport away from the coast driven by equatorward wind stress, is just one form of upwelling active in

EBCs. Another, Ekman pumping, is forced by wind stress curl (a near shore decrease in the magnitude of equatorward wind stress due to frictional effects) and produces lower upwelling velocities that may extend 200-300 km offshore in the California Current System (Pickett and Paduan, 2003). These two mechanisms are comparable in terms of total upwelling volume transport, though the latter is more distributed and less intense, and they seem to sustain different biological communities. For example, off the coast of California, the nearshore region of strong coastal upwelling appears to support larger plankton and anchovies, while smaller plankton and sardines are associated with the offshore region of weaker curl-driven upwelling (Rykaczewski and Checkley, 2008). The evolution of each upwelling component in the future is uncertain and possible trends in both, driven by climate change, have been proposed (Bakun, 1990; Snyder et al., 2003). Further, an increase in one component is likely to accompany a decrease in the other (i.e. a decrease in equatorward winds at the coast would reduce Ekman transport while increasing Ekman pumping). The relative importance of each has therefore been the subject of much debate (e.g., Capet et al., 2004; Albert et al., 2010; Song et al., 2011; Jacox and Edwards, 2012; Seo et al., 2012). From the perspective of this dissertation, the value of these studies is to inform questions regarding controls on primary productivity (phytoplankton growth) in EBCs, as well as changes that may be brought about in the future by natural or anthropogenic influences.

Though there are exceptions (e.g. varying degrees of iron limitation off the California coast in Hutchins et al., 1998), primary productivity (PP) in EBCs is

generally thought to be limited by the supply of nitrogen in the form of nitrate – they are "nitrate-limited" ecosystems. More specifically, the supply of nitrate limits new production, one component of primary production. The other is regenerated production, which is supported by recycling of nutrients in the euphotic zone (the sunlit regime near the surface). The relative contribution of new production is widely variable globally, but is most significant in EBCs, accounting for 50% or more of total PP (Eppley and Peterson, 1979). Upwelling of nutrients from below the euphotic zone is the dominant process supporting new production in EBCs (Dugdale and Goering, 1967), and upwelled nitrate is therefore the currency typically associated with investigations of bottom-up controls on productivity in these regions. In practice, however, quantification of upwelled nitrate is difficult and has been undertaken in several ways. Messié et al. (2009) multiplied *in situ* nitrate at 60 m depth by vertical transport inferred from wind stress to produce potential new production estimates for all four major EBCs. Dever et al. (2006) used a different approach, in which upwelling velocities were directly measured, nitrate was inferred from temperature, and vertical nitrate flux was estimated for a small area off the northern California coast. The first chapter of this dissertation employs yet another method, evaluating fluxes of an embedded nitrate component within a numerical ocean model (Jacox and Edwards, 2011). The latter is the first study to comprehensively examine how variability in physical parameters, which may vary considerably not only among and within EBCs but also through time (e.g., Palacios et al., 2004), influence nitrate fluxes and consequently potential new production.

Ideally, studies on potential new production should be considered in conjunction with observations of primary productivity. However, after nearly a century of research, field measurement of oceanic primary productivity remains extremely labor intensive and subject to large uncertainty. The most common technique employed today, measuring incorporation of radioactive carbon (^{14}C) by growing phytoplankton, was originally introduced over a half-century ago (Steeman-Nielsen, 1951). Briefly, a seawater sample is collected, inoculated with ^{14}C, and incubated for several hours to a day in an environment (temperature, light intensity) representative of where it was collected. Following incubation, the total ^{14}C assimilated by phytoplankton in the sample is measured, and total carbon uptake is estimated from the ^{14}C uptake. The entire process is time and resource intensive, and requires strict adherence to established measurement protocols. Understandably, observations are sparse in space and time. Even the California Cooperative Oceanic Fisheries Investigations (CalCOFI), a long-term continuous sampling program, has collected only ~1600 point measurements of primary productivity in a 25+ year data record. Consequently, the push for alternative methods, capable of synoptic regional and global productivity estimates, has been strong.

The 1978 launch of the Coastal Zone Color Scanner (CZCS) aboard the Nimbus 7 satellite heralded the beginning of the satellite ocean sensing era. As ocean color is indicative of its contents, in particular the pigment chlorophyll contained in phytoplankton, satellite ocean color instruments allowed the first frequent, large scale estimates of surface chlorophyll concentration (representing phytoplankton biomass)

in the ocean. Soon after, efforts expanded beyond chlorophyll measurement to attempts at estimating primary productivity. However, while chlorophyll concentration is a state variable, which can be observed directly from a snapshot in time, primary productivity is a rate variable. It describes how biomass is changing, and cannot be captured by a single point measurement. Its estimation from satellites therefore carries an added degree of difficulty, and typically relies on chlorophyll concentration along with ancillary data that may provide insight into growth rates. Over the past three decades, many algorithms have been developed to estimate primary productivity from satellites (see Saba et al., 2011 for 21 examples), typically utilizing other satellite-observable variables such as sea surface temperature (SST) and photosynthetically available radiation (PAR) to parameterize the relationship between chlorophyll and productivity. However, none of these models has established itself as superior to the others, and model performance does not reflect model complexity (Friedrichs et al., 2009).

Two relatively new oceanographic tools have enormous potential to further our understanding of upwelling dynamics, physical-biological interactions, and productivity in EBCs by effectively providing "everywhere, all the time" data. They are ocean circulation models, whose breadth of application increases as fast as our computational resources, and satellite-based optical sensors, which are at present our only viable platforms for obtaining consistent global ocean coverage. The research presented herein makes use of both to elucidate physical controls on primary productivity in EBCs, as well as the potential for improving our observation of it,

particularly in the California Current System (CCS) that runs the length of the US west coast. Chapter 1 is a numerical modeling study on the effects of stratification, latitude, wind stress magnitude, and continental shelf topography on upwelling circulation and nutrient supply in coastal upwelling regions. Chapter 2 expands the scope of this study to determine the impact of nearshore wind stress curl, an important contributor to coastal upwelling dynamics whose structure is uncertain due to sparse nearshore measurements. The focus in Chapter 3 is improvement of PP measurement capabilities, and analysis is based on satellite ocean color data in conjunction with *in situ* measurements from ships and emerging autonomous platforms.

References

Albert, A., Echevin, V., Lévy, M. and Aumont, O. (2010) Impact of nearshore wind stress curl on coastal circulation and primary productivity in the Peru upwelling system, Journal of Geophysical Research, 115, C12033, doi:10.1029/2010JC006569.

Bakun, A. (1990) Global climate change and intensification of coastal ocean upwelling, Science, 247, 198–201.

Capet, X. J., Marchesiello, P. and McWilliams, J. C. (2004) Upwelling response to coastal wind profiles, Geophysical Research Letters, 31, L13311, doi:10.1029/2004GL020123.

Dever, E. P., Dorman, C. E. and Largier, J. L. (2006) Surface boundary layer variability off Northern California, USA, during upwelling, Deep Sea Research Part II, 53, 2887–2905.

Dugdale, R. C. and Goering, J. J. (1967) Uptake of new and regenerated forms of nitrogen in primary productivity, Limnology and Oceanography, 12, 196–206.

Eppley, R. W. and Peterson, B. J. (1979) Particulate organic matter flux and planktonic new production in the deep ocean, Nature, 282, 677-680.

Friedrichs, M. A. M., Carr, M.-E., Barber, R. T., Scardi, M., Antoine, D., Armstrong, R. A., Asanuma, I., Behrenfeld, M. J., Buitenhuis, E. T., Chai, F., Christian, J. R., Ciotti, A. M., Doney, S. C., Dowell, M., Dunne, J., Gentili, B., Gregg, W., Hoepffner, N., Ishizaka, J., Kameda, T., Lima, I., Marra, J., Mélin, F., Moore, J. K., Morel, A., O'Malley, R. T., O'Reilly, J., Saba, V. S., Schmeltz, M., Smyth, T. J., Tjiputra, J., Waters, K., Westberry, T. K. and Winguth, A. (2009) Assessing the uncertainties of model estimates of primary productivity in the tropical Pacific Ocean, Journal of Marine Systems, 76, 113–133.

Hutchins, D. A., DiTullio, G. R., Zhang, Y. and Bruland, K. W. (1998) An iron limitation mosaic in the California upwelling regime. Limnology and Oceanography, 43, 1037-1054.

Jacox, M. G., and Edwards, C. A. (2012) Upwelling source depth in the presence of nearshore wind stress curl, Journal Geophysical Research, 117, C05008, doi:10.1029/2011JC007856.

Messié, M., Ledesma, J., Kolber, D. D., Michisaki, R. P., Foley, D. G. and Chavez, F. P. (2009) Potential new production estimates in four eastern boundary upwelling ecosystems, Progress in Oceanography, 83, 151–158, doi:10.1016/j.pocean.2009.07.018.

Pauly, D., and Christensen, V. (1995) Primary production required to sustain global fisheries, Nature, 374, 255–257.

Peterson, B. J. (1980) Aquatic Primary Productivity and the ^{14}C-CO_2 Method: A History of the Productivity Problem, Annual Review of Ecology and Systematics, 11, 359-385.

Pickett, M. H., and Paduan, J. D. (2003) Ekman transport and pumping in the California Current based on the U.S. Navy's high-resolution atmospheric model (COAMPS), Journal of Geophysical Research, 108(C10), 3327, doi:10.1029/2003JC001902.

Rykaczewski, R. R., and Checkley, D. M. (2008) Influence of ocean winds on the pelagic ecosystem in upwelling regions, Proceedings of the National Academy of Sciences, 105, 1965–1970.

Saba, V. S., Friedrichs, M. A. M., Antoine, D., Armstrong, R. A., Asanuma, I., Behrenfeld, M. J., Ciotti, A. M., Dowell, M., Hoepffner, N., Hyde, K. J. W., Ishizaka, J., Kameda, T., Marra, J., Mélin, F., Morel, A., O'Reilly, J., Scardi, M., Smith Jr., W. O., Smyth, T. J., Tang, S., Uitz, J., Waters, K. and Westberry, T. K. (2011) An evaluation of ocean color model estimates of marine primary productivity in coastal and pelagic regions across the globe, Biogeosciences, 8, 489–503, doi:10.5194/bg-8-489-2011.

Seo, H., Brink, K. H., Dorman, C. E., Koracin, D. and Edwards, C. A. (2012) What determines the spatial pattern in summer upwelling trends on the U.S. West Coast?, Journal of Geophysical Research, in press, doi:10.1029/2012JC008016.

Snyder, M. A., Sloan, L. C., Diffenbaugh, N. S. and Bell, J. L. (2003) Future climate change and upwelling in the California Current, Geophysical Research Letters, 30(15), doi:10.1029/2003GL017647.

Song, H., Miller, A. J., Cornuelle, B. D. and Di Lorenzo, E. (2011) Changes in upwelling and its water sources in the California Current System driven by different wind forcing, Dynamics of Atmospheres and Oceans, 52, 170–191.

Steemann-Nielsen, E. (1951) Measurement of the production of organic matter in the sea by means of carbon-14, Nature, 167, 684-85.

CHAPTER ONE

Effects of stratification and shelf slope on nutrient supply in coastal upwelling regions

M. G. Jacox[1] and C. A. Edwards[1]

Received 23 July 2010; revised 13 December 2010; accepted 10 January 2011; published 12 March 2011.

[1] An idealized, two-dimensional numerical modeling study is presented to investigate the effects of variable shelf slope and stratification on surface mixed layer (SML) nutrient supply during upwelling. As reported previously, the physical flow regime is governed by a topographic Burger number. Gradual shelf slope and weak stratification concentrate onshore transport in the bottom boundary layer (BBL) while steep slope and strong stratification increase the relative interior transport between the SML and BBL. In 20 day model simulations initialized with a linear nitrate profile, BBL nitrate flux decreases with increasing Burger number. The opposite is true for interior nitrate flux. Upwelling source depth is also investigated and increases more rapidly with weak stratification and steep slope. Both nitrate flux and source depth are well represented by an empirical model approaching an asymptotic value with time. Model experiments representing specific locations in major upwelling systems are analyzed to determine the impact of global variability in physical parameters on event-scale nitrate supply. After 5 days, nitrate flux into the SML is ~45 mmol s^{-1} m^{-1} of coastline at a Peru site, ~30 mmol s^{-1} m^{-1} at northern California and northwest Africa sites, and <2 mmol s^{-1} m^{-1} off Newport, Oregon. BBL flow dominates onshore transport in northwest Africa and northern California runs, while the interior contributes significantly at our Peru and Oregon sites. Nitrate flux estimates based on constant upwelling source depth are strongly dependent on source depth choice at our selected California Current sites and less so at selected Peru and Canary Current sites.

Citation: Jacox, M. G., and C. A. Edwards (2011), Effects of stratification and shelf slope on nutrient supply in coastal upwelling regions, *J. Geophys. Res.*, *116*, C03019, doi:10.1029/2010JC006547.

1. Introduction

[2] Wind-driven coastal upwelling in eastern boundary current systems (EBCs) transports cold, nutrient-rich water to the surface, placing these regions among the ocean's most productive in terms of both primary production and fish catch [*Chavez and Toggweiler*, 1995; *Pauly and Christensen*, 1995]. The biological importance of EBCs has long been known and they have been subject to intensive study, but questions remain about controls on productivity, which varies widely within and among upwelling systems [*Carr and Kearns*, 2003]. Although new production in EBCs is supported primarily by upwelling of deep nutrients to the euphotic zone [*Dugdale and Goering*, 1967], the relationship between nitrate supply and primary production is unclear [*Chavez and Messié*, 2009].

[3] The vertical structure of cross-shelf flow has obvious implications for nutrient supply to the euphotic zone, and mooring data show substantial variation in this structure among global upwelling regions [*Smith*, 1981]. Motivated by these observations, *Lentz and Chapman* [2004] (hereafter referred to as LC) developed a simple, steady state theory for two-dimensional wind-driven coastal upwelling as a function of the topographic Burger number

$$S = \alpha N / f, \tag{1}$$

where α is topographic slope of the continental shelf, N is buoyancy frequency, and f is Coriolis frequency. The theory describes the relative proportion of volume transport in the bottom boundary layer (BBL) and ocean interior. Lower Burger numbers yield cross-shelf flow more concentrated in the BBL. As Burger number increases, surface wind stress is increasingly balanced by the cross-shelf momentum flux divergence rather than bottom stress, and cross-shelf transport occurs increasingly in the interior. Though highly simplified, the steady state theory shows strong quantitative agreement with 2-D model experiments over a linearly sloping shelf and agrees qualitatively with mooring data from the California, Humboldt, and Canary upwelling systems.

[4] Burger number parameters (topography, stratification, and latitude) vary significantly worldwide (Table 1), motivating our study to investigate their respective roles in determining nutrient supply, and thus new production. While

[1]Department of Ocean Sciences, University of California, Santa Cruz, California, USA.

0148-0227/11/2010JC006547

Table 1. Model Input Parameters for Global Upwelling Regions[a]

Site	Upwelling Season	α (10^{-3})	N (10^{-3} s^{-1})	f (10^{-4} s^{-1})	τ (N m^{-2})	S
Peru	Jul–Sep	8.75	5.85	−0.38	0.11	1.35
Oregon	Jun–Aug	6.7	14.6	1.03	0.03	0.95
N California	May–Jul	5	7.75	0.91	0.18	0.43
NW Africa	Jun–Aug	1.5	6.7	0.54	0.13	0.19

[a]Here α is shelf slope, N is buoyancy frequency, f is Coriolis frequency, τ is surface wind stress, and S is Burger number. The α, N, and f are from *Lentz and Chapman* [2004], and τ is a mean of QuikSCAT alongshore wind stress averaged over the upwelling season.

two-dimensional models have been employed previously to elucidate physical characteristics of upwelling circulation [e.g., *Allen et al.*, 1995; *Lentz and Chapman*, 2004; *Chapman and Lentz*, 2005; *Estrade et al.*, 2008], we are unaware of any that examine the resultant effects on nutrient distribution. *Laanemets et al.* [2009] use the LC theory to explain greater nutrient input along the south coast of the Gulf of Finland than the north coast under equal upwelling favorable winds. While their study demonstrates the potential of the idealized model to explain real world observations, it considers only a single case with weak slope ($\alpha = 0.002 - 0.004$), strong stratification ($N = 0.025$ s^{-1}), and high latitude ($f = 1.25 \times 10^{-4}$ s^{-1}). Building on the results of LC, we examine how nutrient supply and upwelling source depth are affected by physical properties spanning those found in major global upwelling regions.

[5] Although physical transports are determined by the Burger number, nitrate flux is modulated by stratification, bottom slope, and Coriolis frequency independently. Changes to the Burger number through stratification alter the relative fraction of interior and bottom transport, and thus the nutrient supply. However, bottom slope effects are more complex. Weak slope (low Burger number) concentrates flow in the BBL, while a steep slope results in deep water being laterally closer to the coast. Though a greater fraction of transport will be near the bottom for $\alpha = 0.004$ than $\alpha = 0.008$, water of a given depth (and nitrate concentration) must travel only half as far to reach the coast in the latter case. Similarly, increasing Coriolis frequency decreases Ekman transport, but also shifts onshore flow to the BBL.

[6] There are several parts to this study. First, an idealized 2-D numerical model configured to approximate a wide range of upwelling regions is diagnosed for nitrate fluxes and upwelling source depth through time. Though nitrate is chosen here to represent nutrient availability, the approach and conclusions are generally applicable to other macronutrients such as phosphate and silicate. Total surface nitrate, its rate of change, and individual contributions of the BBL and interior are related to the physical constraints of the system, including stratification, shelf slope, wind stress, and latitude. Second, a set of analytical expressions, empirically obtained from model output, are presented to quantify the temporal evolution of upwelled nitrate and characteristic source depth of upwelled waters. Finally, the model is applied to specific locations in global EBCs to illustrate possible controls on nutrient availability.

2. Regional Ocean Modeling System Model

[7] Numerical model experiments are performed using the Regional Ocean Modeling System (ROMS [*Shchepetkin and McWilliams*, 2005; *Haidvogel et al.*, 2008]) with a two-dimensional (no alongshore variation) setup similar to that of LC. A periodic channel is constructed with two alongshore grid points, a wall 160 km offshore, and 1 km horizontal grid resolution. There are 100 vertical levels, concentrated near the surface and bottom to ensure adequate resolution of the boundary layers. While fewer vertical levels could be used without altering the model substantively, high vertical resolution allows for cleaner calculation of model diagnostics, specifically advective and diffusive tracer fluxes. Bottom depth increases linearly from a minimum of 20 m at the coast to a maximum of 1000 m offshore. Turbulence closure is handled by the Mellor-Yamada level 2.5 scheme, and there is no explicit lateral mixing. The domain is initiated from rest and forced by a spatially and temporally uniform upwelling-favorable alongshore wind stress. Except where otherwise noted, wind stress $\tau = 0.1$ N m^{-2} and Coriolis frequency $f = 10^{-4}$ s^{-1}.

[8] To determine sensitivity of the model to variations in its parameters, a number of configurations were explored. We examined several vertical mixing schemes ($k - \omega$ and $k - \epsilon$ in generic length scale [*Umlauf and Burchard*, 2003] and K profile parameterization [*Large et al.*, 1994]) in place of Mellor-Yamada level 2.5. Alternative offshore boundary conditions tested include a closed boundary 500 km offshore, a highly viscous sponge added near the boundary, and a radiation boundary condition. Finally, horizontal resolution was increased from the default 1 km to 0.5 km and 0.25 km. While small-scale circulation features are altered by these configuration changes, implications are negligible for the net transport processes of interest here.

[9] LC investigated the effect of Burger number on cross-shelf transport by varying stratification while holding both Coriolis frequency and shelf slope constant. Here, an initial set of 12 model runs intended to replicate their findings produced similar results and matched the theory well after several days of spin-up. Additionally, a set of 25 model runs were performed with shelf slopes of 0.002, 0.004, 0.006, 0.008, and 0.010 and buoyancy frequencies of 0.004, 0.008, 0.012, 0.016, and 0.020 s^{-1}. These parameters were chosen to cover the range of conditions found in the major global upwelling regions and to investigate stratification and slope effects independently. Sensitivity to changes in Coriolis frequency was not examined as thoroughly; however three model configurations with wide-ranging Burger numbers were run with Coriolis frequency varied between 0.4×10^{-4} and 1.3×10^{-4} s^{-1}. To track nutrient fluxes, a passive tracer representing nitrate (and herein referred to simply as nitrate) was introduced with an initial profile increasing linearly from 0 μM at the surface to 30 μM at 200 m depth and remaining constant below 200 m.

[10] Finally, several model runs were performed to more closely represent specific global upwelling regions. These runs are still idealized in that they are 2-D and have linearly

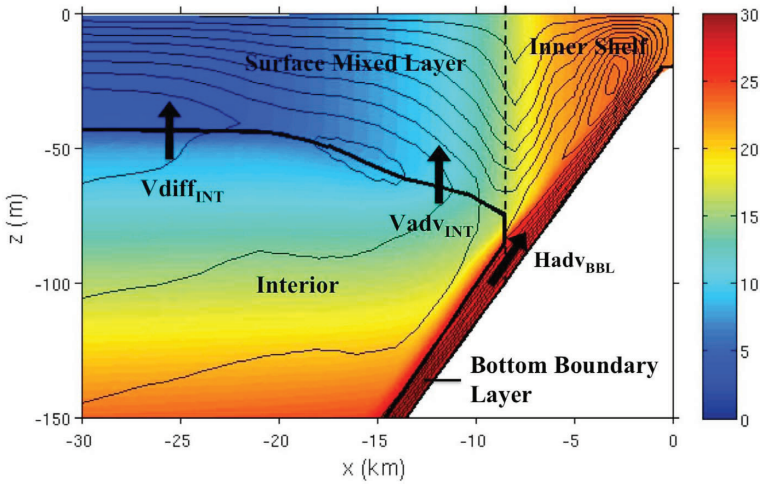

Figure 1. Streamlines (thin black lines) overlaid on nitrate concentration (μM, color) for model output on day 10, with $\alpha = 0.010$ and $N = .004$ s^{-1}. Thick black lines mark the surface and bottom mixed layers and extent of the inner shelf (dashed). Arrows indicate contributions to nitrate flux, which are horizontal advection in the bottom boundary layer (Hadv$_{BBL}$) and vertical advection (Vadv$_{INT}$) and diffusion (Vdiff$_{INT}$) in the interior. Offshore advection in the surface mixed layer (Hadv$_{OFF}$) and mixed layer deepening ($\mathcal{E}$) are not shown. These five terms make up the surface mixed layer budget as outlined in equation (5).

sloping bottom topography, surface wind forcing that is uniform in space and time, and constant stratification. However in each case, the buoyancy frequency, bottom slope, latitude, wind stress magnitude, and initial nitrate profile are characteristic of the region of interest. The locations chosen are those discussed in LC, where mooring data provide an accurate determination of stratification in the water column.

3. Methodology

[11] For budgeting purposes, we divide the model domain into four regions: the inner shelf, the surface and bottom mixed layers, and the interior between them. Near shore, bottom and surface mixed layers converge, and we define here the region where their boundaries are separated by less than 10 m as the inner shelf. Figure 1 illustrates these regions and also shows instantaneous streamlines of the flow superposed on nitrate concentration for a representative model run. In our configuration, x denotes cross-shelf distance with the coastal boundary, $x = 0$, located at the eastern edge. The vertical coordinate is z, directed upward, with the unperturbed ocean surface at $z = 0$. The ocean bottom is given by $z_b(x) < 0$, and the free surface is denoted $\zeta(x, t)$.

[12] Several approaches to define the surface mixed layer (SML) are possible. LC used the first zero crossing of cross-shelf velocity (the depth at which cross-shelf transport switches from offshore to onshore). An alternative is the depth at which temperature or density differs by a fixed amount from the surface value. A third definition, the PRT depth [*Pollard et al.*, 1973], scales mixed layer depth as $u_*/(Nf)^{1/2}$ where u_* is shear velocity. *Lentz* [1992] found the PRT depth to effectively capture subtidal mixed layer depth variability at locations in the California, Peru, and Canary Current systems. We found that surface layer offshore flow in our model is best diagnosed by high vertical viscosity coefficients and used a value of $10^{-3.5}$ m^2 s^{-1} to define the base of the SML (z_{sml}). This approach aligns this boundary well with streamlines near the upwelling front. The height of the BBL is defined in the same manner.

[13] We consider the total nitrate, $\mathcal{N}_\mathcal{T}$, contained within a control volume encompassing the SML and inner shelf region from a predefined offshore distance ($x_o = -100$ km) to the coast

$$\mathcal{N}_\mathcal{T}(t) = \int_{x_o}^{0} \int_{z_0(x,t)}^{\zeta(x,t)} N(x,z,t)\, dz\, dx. \tag{2}$$

Here $N(x, z, t)$ indicates nitrate concentration and

$$z_0(x,t) = \begin{cases} z_{sml}(x,t) & x < x_i \\ z_b(x) & x \geq x_i, \end{cases} \tag{3}$$

where x_i is the x coordinate of the inner shelf boundary.

[14] For a general control volume, Ω, and assuming no internal sources or sinks, changes to $\mathcal{N}_\mathcal{T}$ in time are given by the combination of advective and diffusive nitrate fluxes, $\mathcal{F}$, across the bounding control surface, Ω_S, and nitrate that is captured (or lost) by expansion (or contraction) of Ω

$$\frac{d\mathcal{N}_\mathcal{T}}{dt} = -\int_{\Omega_S} \mathcal{F} \cdot \mathbf{n}\, dS + \int_{\Omega_S} N(\mathbf{u_S} \cdot \mathbf{n}) dS. \tag{4}$$

The outward normal is denoted $\mathbf{n}$, and $\mathbf{u_S}$ represents the velocity of the control surface. To understand the meaning of the second term, it is helpful to consider the simple

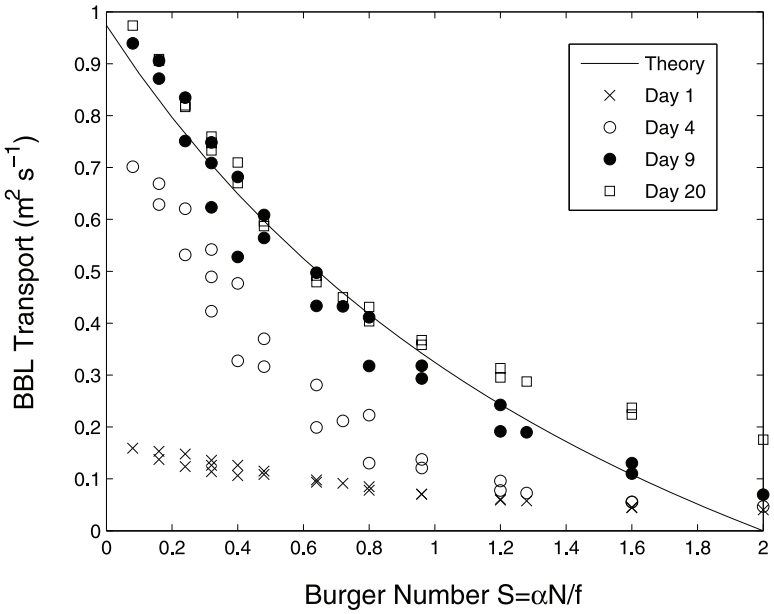

Figure 2. Evolution of bottom boundary layer transport as a function of Burger number. For each model run, transport is calculated at the offshore distance where bottom depth is 90 m, as with *Lentz and Chapman* [2004]. Shown for comparison is their steady state theory. Volume transport is per meter of coastline.

(though unrealistic) case in which $\mathcal{F} = 0$ (e.g., with zero velocity and constant nitrate distribution) but the control volume is expanding (i.e., $\mathbf{u_S} \cdot \mathbf{n} > 0$). In this circumstance, nitrate initially outside the control volume boundary accumulates within the volume as it expands, increasing total integrated nitrate, $\mathcal{N}_\mathcal{T}$.

[15] For our configuration, we neglect horizontal diffusion and decompose the first term on the right hand side of equation (4) into three advective fluxes and one diffusive flux, each illustrated in Figure 1. Thus,

$$\frac{d\mathcal{N}_\mathcal{T}}{dt} = \int_{z_b}^{z_{sml}} uN\Big|_{x_i} dz - \int_{x_o}^{x_i} (\mathbf{u}\cdot\mathbf{n})N\Big|_{z_{sml}} dx + \int_{z_{sml}}^{\zeta} uN\Big|_{x_o} dz + \int_{x_o}^{x_i} K_v \frac{dN}{dz}\Big|_{z_{sml}} dx + \mathcal{E}, \quad (5)$$

where u is the fluid velocity in the x direction and K_v represents the vertical diffusion coefficient for nitrate. The velocity normal to the SML boundary, $z_{sml}(x, t)$, is $\mathbf{u} \cdot \mathbf{n}$. Owing to the aspect ratio, $\mathbf{u} \cdot \mathbf{n}$ appears overwhelmingly vertical when viewed schematically, but horizontal transports across this boundary are numerically sizeable. The terms on the right hand side of equation (5) represent (1) transport across the inner shelf boundary associated with BBL advection (Hadv_{BBL}), (2) transport between the ocean interior and SML (Vadv_{INT}), (3) horizontal advection within the SML across $x = x_o$ (Hadv_{OFF}), (4) vertical diffusion between the interior and SML (Vdiff_{INT}), and (5) changes in $\mathcal{N}_\mathcal{T}$ due to shifts in the SML depth and the inner shelf boundary ($\mathcal{E}$). All terms in equation (5) are calculated and compared using discrete approximations appropriate for the model grid. Advective and diffusive fluxes are determined from model state vector output, recorded every 6 h. Changes to total nitrate as well as the contribution due to mixed layer deepening and inner shelf boundary adjustment are calculated using time differences between model output.

4. Results

4.1. Model Results

[16] As discussed by LC, physical transports are dependent on the Burger number, which combines three independent physical parameters. Here we investigate each component separately as they impact tracer advection in different ways, discussed in section 1. A total of 25 model runs are presented that encompass shelf slopes from 0.002 to 0.010 and buoyancy frequencies from 0.004 to 0.020 s^{-1}. The sensitivity to Coriolis frequency is also considered.

[17] Cross-shelf transport develops over several days and agrees well with the LC steady theory after day 9 (Figure 2), though BBL transport is greater in the model than the theory for higher Burger numbers ($\gtrsim 1$) and longer integration times. LC also noted this and found that bottom stress decreases with increasing Burger number, but not as much as predicted by the theory. In all cases, upwelling-favorable wind stress drives a subsurface structure consisting of an offshore region with approximately level isopycnals, a midshelf region characterized by sloping isopycnals, and the inner shelf zone

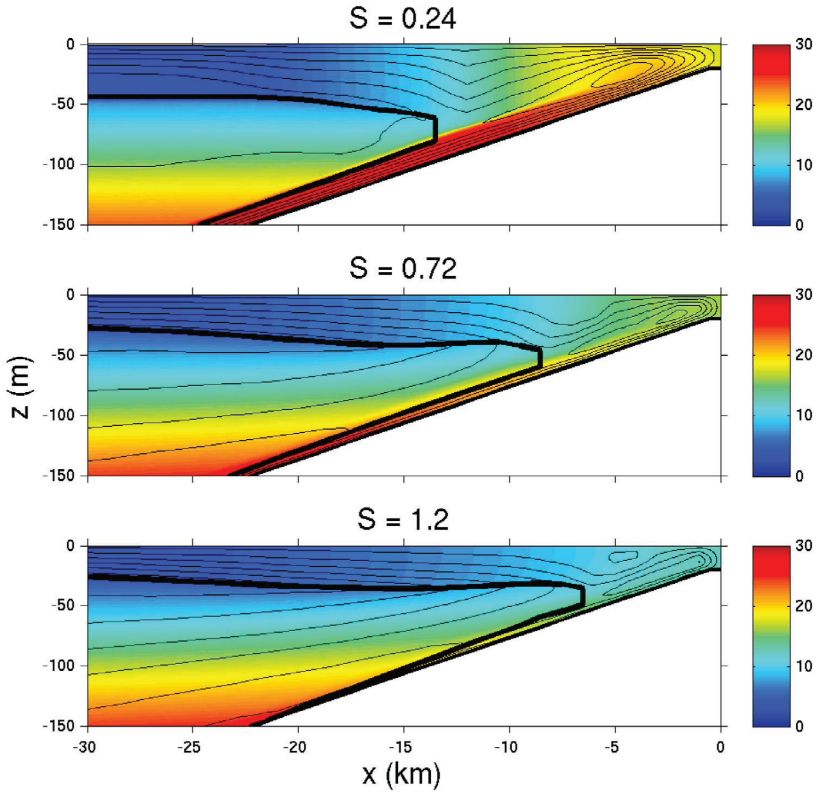

Figure 3. Mixed layers, inner shelf, nitrate, and streamlines are depicted as in Figure 1, for varying Burger numbers on day 10. For all, $\alpha = 0.006$. Buoyancy frequencies are (top) 0.004 s^{-1}, (middle) 0.012 s^{-1}, and (bottom) 0.020 s^{-1}.

where bottom and surface mixed layers merge. Under sustained surface forcing an upwelling front develops, as described by *Allen et al.* [1995]. The upwelling front is marked by strong turbulence and a locally deepened SML (deeper in weakly stratified waters) that typically sets the offshore boundary of the inner shelf. Inshore of the front the model produces onshore flow near the bottom, offshore flow near the surface, and some recirculation at middepths (Figure 3). In certain cases, such as the $S = 1.2$ case in Figure 3, recirculation occurs within the front. With time the front and associated coastal jet strengthen and move offshore at an approximately constant rate as with *Austin and Lentz* [2002]. Figure 4 shows the offshore expansion of the inner shelf with time, and its dependence on slope and stratification. Strong stratification and steep slope ($\alpha N \gtrsim 10^{-4}$ s^{-1}) produce an inner shelf that is confined close to shore, typically within 10 km even after 10–20 days of upwelling. In contrast, weak stratification and gently sloping topography can produce an inner shelf that rapidly extends its offshore reach. Coriolis frequency also impacts the inner shelf extent (not shown); at a given time, the inner shelf extends further offshore at lower latitudes.

4.1.1. Nitrate Fluxes

[18] At low Burger numbers, flow is concentrated in a thick BBL as evidenced by the cross-shelf stream function

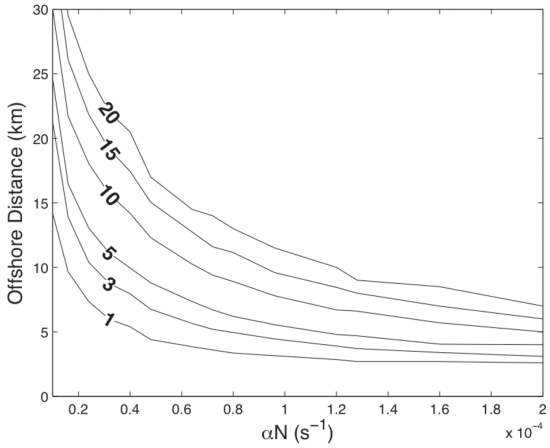

Figure 4. Evolution of the inner shelf and its dependence on Burger number. Distance is measured from the coast to the offshore boundary of the inner shelf. Contours indicate time in days.

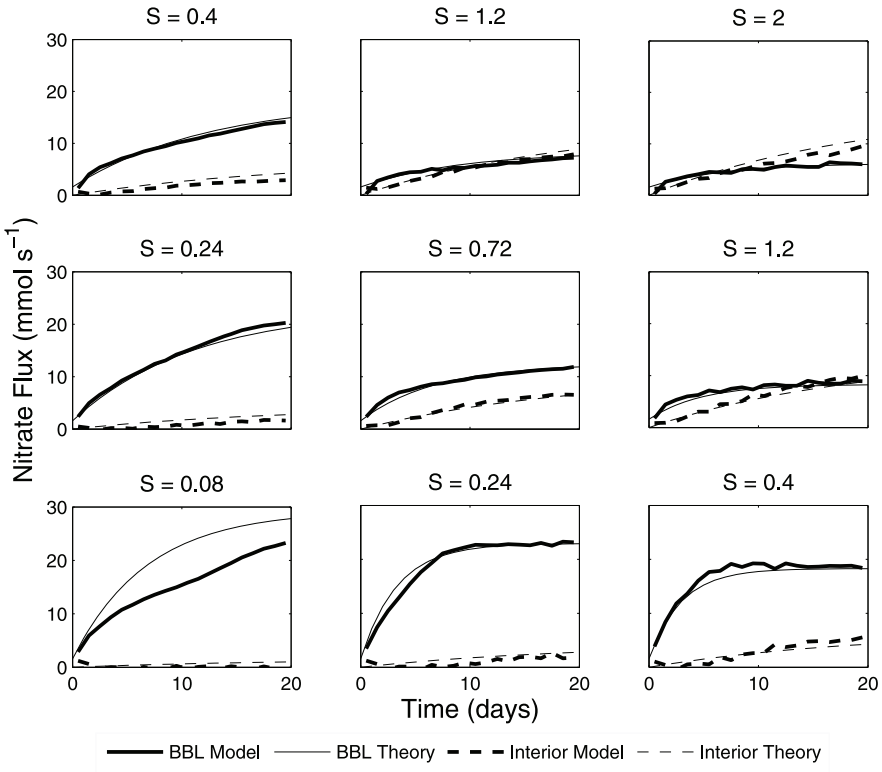

Figure 5. Time evolution of BBL and interior advective nitrate fluxes. Buoyancy frequency increases from bottom to top with values of 0.004, 0.012, and 0.020 s^{-1}. Topographic slope increases from left to right with values of 0.002, 0.006, and 0.010. Coriolis frequency in all cases is 10^{-4} s^{-1}. Thick lines are fluxes calculated from model output, and thin lines are fluxes calculated from the empirical model described by equation (8) and Table 2.

(Figure 3). Deep, high-nitrate (~30 μM) water is rapidly transported onshore in the BBL, mixes in the inner shelf, and moves offshore in the SML. Strong stratification (higher Burger number) produces a thin BBL and shifts streamlines to the interior. For S = 1.2, substantial upwelling of intermediate nitrate concentrations (5–15 μM) is visible offshore of the upwelling front, extending ~20 km from the coast. In all three cases shown in Figure 3, surface nitrate at the inner shelf boundary is ~10 μM on day 10. The cross-shelf nitrate gradient is stronger at low Burger numbers, producing a more rapid decrease in nitrate away from the upwelling front. Surface transport offshore of the active upwelling zone is independent of Burger number, though streamlines are concentrated in a shallower SML in strongly stratified systems.

[19] In the model, nitrate is a conserved passive tracer, with no sources or sinks. Nitrate fluxes are calculated through time, and nitrate is assumed to be available for biological uptake upon reaching the SML. Interior and BBL nitrate fluxes and their dependence on stratification and slope over the first 20 days of model runs are shown in Figure 5. At low Burger numbers a large fraction of transport is concentrated in the BBL and deep, nitrate-rich water is carried efficiently to the surface. Higher Burger numbers produce a greater fraction of onshore transport in the interior of the water column, increasing nitrate advection from the interior to the surface. Since bottom flow draws from deeper source waters than interior flow, upwelling in the BBL is typically the dominant contributor to total nitrate flux, even in cases where interior transport exceeds BBL transport. In our highest Burger number case (S = 2), the source of upwelled water is primarily the interior of the water column; however, interior and BBL nitrate fluxes are comparable through much of the run. In this case, weak BBL transport is able to produce significant nitrate flux when combined with high BBL nitrate concentrations.

[20] The results of Figure 5 are of course dependent on our choice of initial nitrate profile. The linearly increasing nitrate profile is a good qualitative representation, but arguably too simplistic for real systems. For comparison, we show the same model runs initialized with a real nitrate profile taken off the Oregon coast at ~45 N and obtained from the Global Ocean Ecosystems Dynamics (GLOBEC) database. This profile has nitrate concentrations that are low in the upper 20 m ($\leq$2.5 μM), increase rapidly below the SML to ~27 μM at 100 m depth, and increase gradually at greater

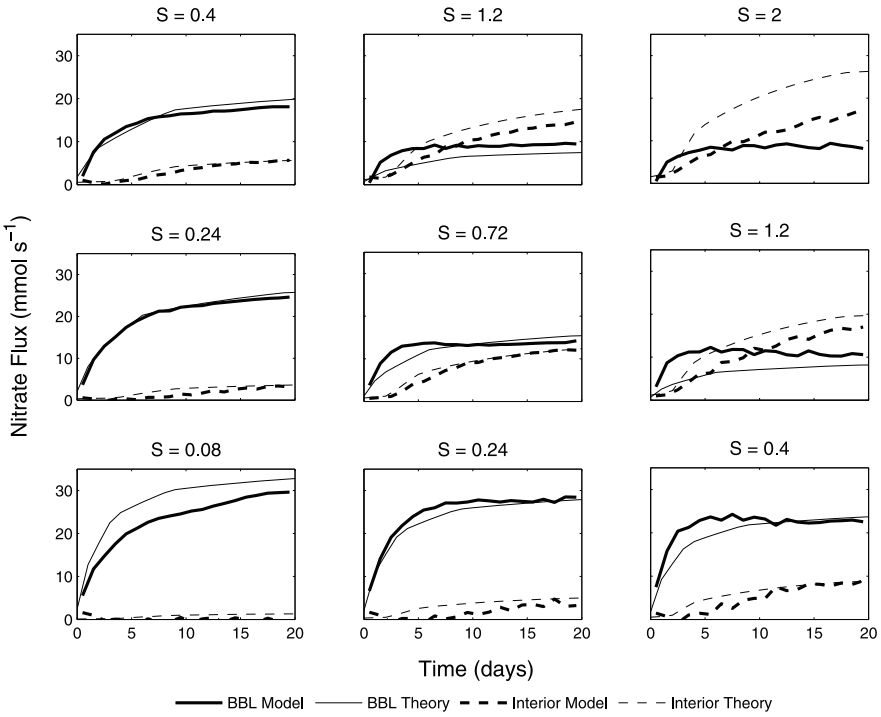

Figure 6. Empirical model of nitrate flux based on upwelling source depth. Slope, stratification, and Burger number are as in Figure 5. The initial nitrate profile is a real profile off the Oregon coast obtained from the GLOBEC database, rather than the idealized profile used for Figure 5. Actual nitrate fluxes as calculated from ROMS output are shown as thick solid and dashed lines for the BBL and interior, respectively. Thin solid and dashed lines are empirical model fluxes calculated from equations (9)–(11) and Table 2. Note that in the highest Burger number case ($S = 2.0$, top right), theoretical BBL transport, and therefore empirically modeled BBL nitrate flux, is zero.

depths, reaching 34 μM at 200 m. There are clear differences between results from the idealized profile (Figure 5) and the real one (Figure 6). For example, nitrate fluxes resulting from the real profile initially increase more rapidly owing to high nitrate concentrations available closer to the surface. However, the qualitative relationship between BBL and interior nitrate fluxes remains unchanged; the BBL dominates at lower Burger numbers and the two components are comparable in magnitude at higher Burger numbers.

[21] Figure 7 presents flux contributions from interior advection, BBL advection, and mixed layer deepening on day 15. The combination of bottom and interior advective fluxes, interior diffusion, and mixed layer deepening gives total nitrate available for new production in the SML. Interior and BBL nitrate fluxes are strongly dependent on Burger number; as Burger number increases, interior flux increases and BBL flux decreases. BBL flux is skewed slightly with weak slope transporting nitrate to the surface more efficiently than weak stratification (for a given Burger number, nitrate flux per unit upwelled volume is greater with weak slope than weak stratification). Similarly for interior flux, steep slope transports nitrate to the surface more efficiently than strong stratification. Vertical diffusion is a relatively small contributor to nitrate supply (1–3 mmol s^{-1}, not shown), but is greatest in weakly stratified water with weak topographic slope. As the SML deepens, it incorporates nitrate previously beneath it. This contribution is greater in weakly stratified conditions, as the mixed layer deepens more rapidly and reaches greater depth in a given time. It is also greater in regions of steep slope; strong interior transport carries high nitrate to the base of the SML where it is entrained as the SML deepens. In sum, total advective nitrate fluxes are greatest with weak stratification and slope ($S \ll 1$), diffusion is small but greater in weakly stratified waters, and nitrate added due to mixed layer deepening is greatest with steep slope and weak stratification. The net effect of these contributions is that total nitrate in the SML after a period of sustained upwelling is primarily dependent on stratification, with the most nitrate available in weakly stratified waters.

4.1.2. Upwelling Source Depth

[22] Understanding the source depth of upwelling allows for more general questions than those of macronutrient supply. To calculate source depth, we introduce a tracer C increasing linearly with depth, and define the "source tracer concentration" ($\mathcal{S}$) as tracer flux divided by volume transport. This quantity is determined at the inner shelf boundary

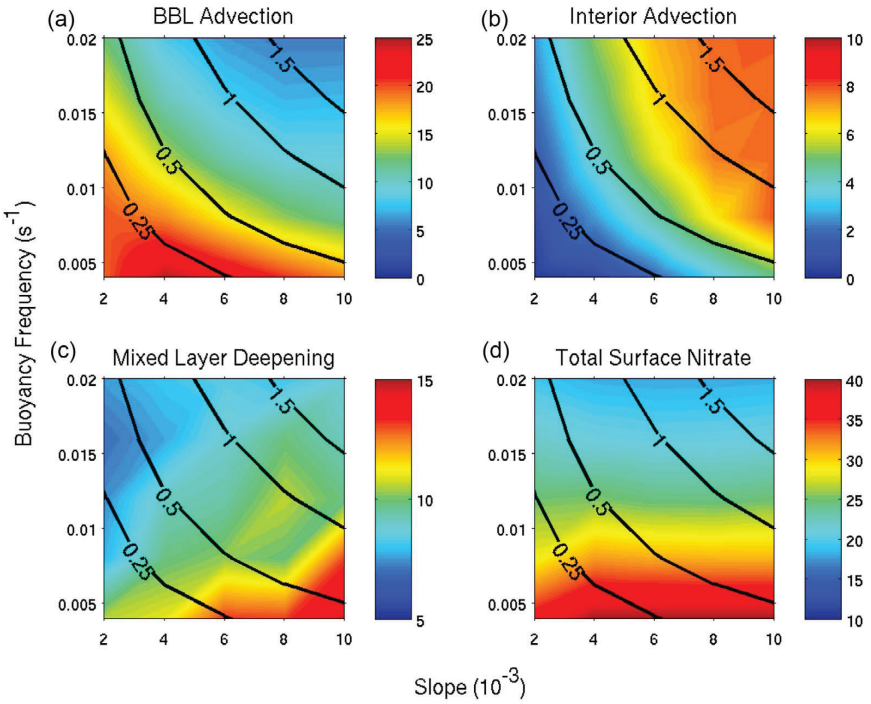

Figure 7. Snapshots of nitrate flux components (in color) on day 15, with Burger number indicated by contours. Nitrate fluxes due to advection in the (a) BBL and (b) interior (mmol s^{-1}), (c) flux due to mixed layer deepening (mmol s^{-1}), and (d) total nitrate in the surface mixed layer within 100 km of the coast on day 15 (10^3 mol N). Note different scales for each. The 25 model runs are represented covering slopes of 0.002–0.010 and buoyancy frequencies of 0.004–0.020 s^{-1}.

for BBL flux and at the base of the SML for interior flux. Specifically,

$$\mathcal{S}_{BBL} = \frac{\int_{z_b}^{z_{sml}} uC\Big|_{x_i}\, dz}{\int_{z_b}^{z_{sml}} u\Big|_{x_i}\, dz} \tag{6}$$

$$\mathcal{S}_{INT} = \frac{\int_{x_o}^{x_i} (\mathbf{u}\cdot\mathbf{n})C\Big|_{z_{sml}}\, dx}{\int_{x_o}^{x_i} (\mathbf{u}\cdot\mathbf{n})\Big|_{z_{sml}}\, dx}. \tag{7}$$

Because the initial tracer profile increases monotonically from the surface to the sea floor (unlike our idealized nitrate profile), source tracer concentration can be mapped to source depth. Of course, not all upwelled water originates exactly from this depth, but it is a useful integrated measure of the characteristic depth of upwelling at any given time.

[23] Figure 8 illustrates time evolution of interior and BBL source depth over 20 days of model simulations for a range of Burger numbers. Figure 9 shows snapshots of source depths in all 25 model configurations after 10 and 20 days of model integration. In the BBL, steep slope and weak stratification produce the greatest source depth. Strong BBL transport carries deep water onshore rapidly in weakly stratified waters. Also, since deep water is closer to shore in steep slope cases, it reaches the surface faster with the same horizontal velocity (compare Figure 1 to Figure 3 (top), which has the same stratification but different slope). In runs with weak stratification and steep slope, source depth exceeds 200 m by day 10 and nitrate advection in the BBL is approximately constant after this time (Figure 5). The asymptotic nitrate flux is set by the steady state BBL transport and maximum nitrate at depth (30 μM). By day 20, only strongly stratified cases have BBL transport originating from less than 200 m depth.

[24] The source depth of upwelled water in the interior depends primarily on topographic slope (Figure 9). Interior transport occurs throughout the region between bottom and surface mixed layers (Figure 3). As with BBL source water, steeper slope configurations have deeper water available at a given distance offshore. This deep water has a shorter path length to reach the upwelling zone than in weak slope cases and reaches the surface sooner with the same horizontal velocity. Stratification appears to become more important at longer times, with weak stratification producing deeper source water after 20 days. By the end of the model run, weak stratification over a steep shelf produces interior upwelling from the greatest depths, approximately 120 m.

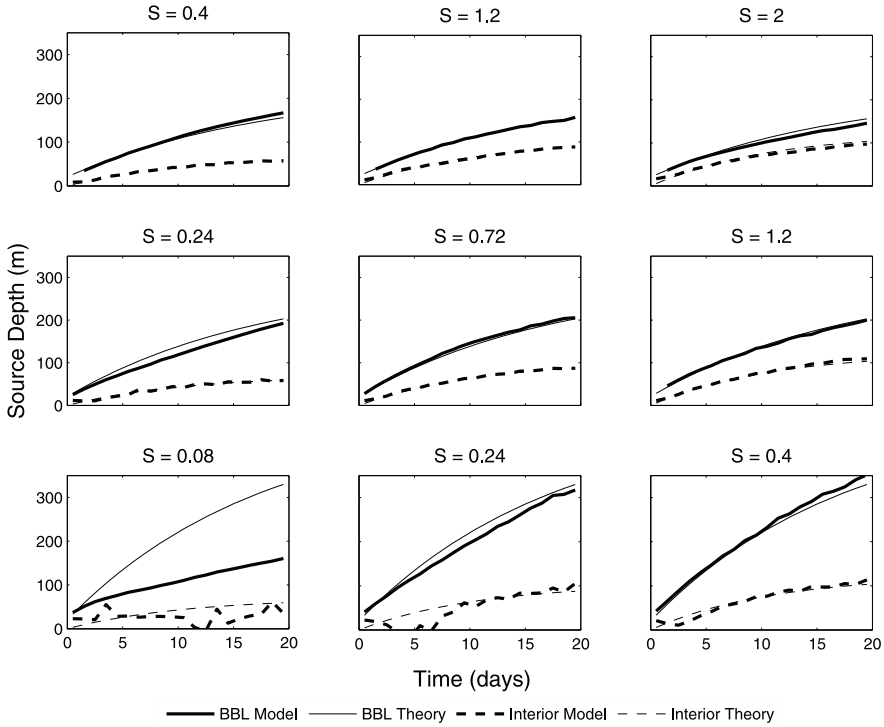

Figure 8. Time evolution of numerical model BBL (thick solid) and interior (thick dashed) upwelling source depths along with those predicted by the empirical model (thin lines). Empirical model approximations come from equation (9) with parameterizations in Table 2. Slope, stratification, and Burger number are as in Figure 5.

4.1.3. Sensitivity to Wind Stress and Latitude

[25] Thus far, Coriolis frequency and wind stress have been held constant at $f = 10^{-4}$ s^{-1} and $\tau = 0.1$ N m^{-2}, respectively. Since both vary significantly across global upwelling regions, their influence on results was investigated. Theoretical Ekman transport is proportional to wind stress, and in model runs where surface forcing is reduced, BBL and interior transport are reduced proportionally. However this transport reduction is not proportional to the nitrate flux reduction. For any model time, the source depth (and therefore nitrate concentration) is greater for a strongly forced case than a weakly forced one. Because reduced wind stress decreases upwelled volume as well as nitrate concentration within upwelled water, the net result is a nonlinear relationship between wind stress and advective nitrate flux (Figure 10). Assuming that nitrate flux scales like volume transport would overestimate flux for winds weaker than the reference case (τ_o) and underestimate it for stronger winds. This effect is independent of Burger number; nitrate flux is altered to the same degree in cases of wide ranging slope and stratification.

[26] The impact of changing Coriolis frequency is more complex. In this case, not only is Ekman transport affected, but also Burger number; both are proportional to $1/f$. At lower latitudes, Ekman transport increases, but a greater fraction derives from the interior. To assume that BBL flux should scale with $1/f$ (like transport) overestimates flux at latitudes lower than the reference (f_o) and underestimates it at higher latitudes (Figure 11). The opposite is true for interior flux. It is not our goal to provide an accurate measure of the scaling of nitrate flux with latitude, merely to point out that at low latitude, gains in nitrate flux due to stronger upwelling are partially offset by a shift in upwelling from the BBL to the interior.

4.2. Empirical Model

[27] For a given model latitude, surface forcing, and initial nitrate profile, the magnitude of each nitrate flux component into the SML is determined by topography and stratification. Bottom and interior advective fluxes increase rapidly with time before approaching an asymptotic value, and can be characterized by a simple expression of the type

$$F(t) = (F_m - F_0)\left(1 - e^{-t/T}\right) + F_0, \tag{8}$$

where nitrate flux (F) at time t is described by a characteristic maximum flux (F_m), initial flux (F_0), and time scale (T). Similarly, upwelling source depth as calculated in section 4.1.2 can be approximated by

$$d(t) = (d_m - d_0)\left(1 - e^{-t/T}\right) + d_0, \tag{9}$$

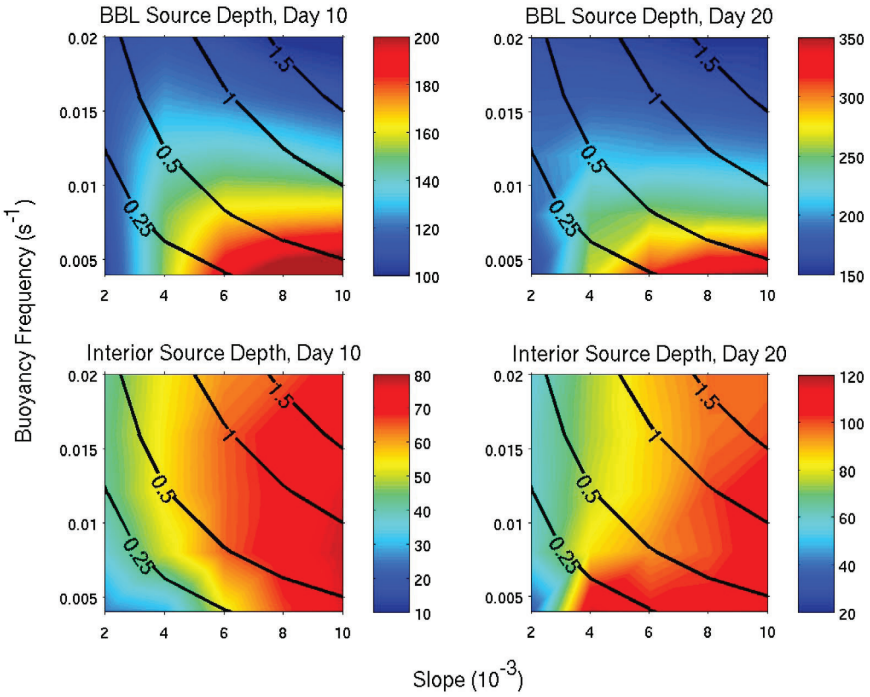

Figure 9. Upwelling source depths (m) for (top) BBL and (bottom) interior nitrate fluxes after 10 and 20 days, with Burger number indicated by contours. As in Figure 7, 25 model runs are represented spanning a range of slope and stratification. Note different color scales for each.

where the flux (F) terms in equation (8) are replaced by depth (d) terms in equation (9). For each model run, nitrate flux (or source depth) is fit using values of T, $F_0(d_0)$, and $F_m(d_m)$ that minimize model-data misfit in a least squares sense. These values are then parameterized by physical properties of the water column (α, N) as outlined in Table 2. As mentioned previously, the effect of Coriolis frequency on nitrate flux is complicated. All model experiments used for development of the empirical model have $f = 10^{-4}$ s^{-1}, so parameters that appear to vary with Burger number are reported as functions of αN rather than S. The F_0 and d_0 terms represent nonzero flux and source depth at $t = 0$ and are not strictly accurate for a system initiated from rest. However, immediately following the onset of upwelling favorable winds, a finite inner shelf region is established. Since we calculate BBL nitrate flux and source depth at the inner shelf boundary, the empirical model is best configured with a nonzero initial condition associated with the inner shelf extent shortly after initialization. While interior flux and source depth are independent of the inner shelf definition, an analogous effect could be produced by rapid development of the SML. We find this effect to be small and configure the interior flux and source depth equations with $F_0 = d_0 = 0$.

[28] The time scale for BBL nitrate flux evolution is not representative of the flow itself, but rather how quickly BBL transport draws from depths below the nitrate maximum at 200 m. Beyond this time no greater nitrate can be transported to the surface, even as source depth increases. Weak strati-

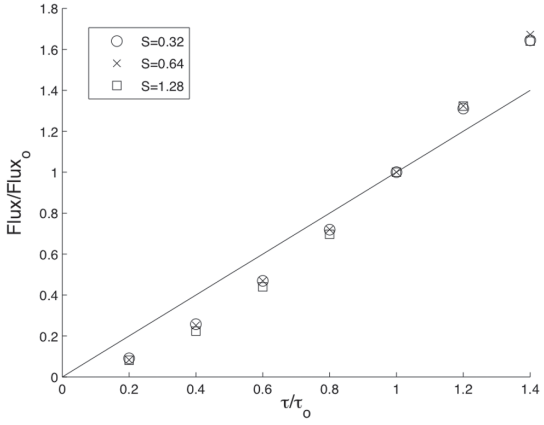

Figure 10. Scaling of BBL nitrate flux relative to wind stress. Surface wind stress and BBL flux are scaled by the base case where $\tau_o = 0.1$ N m^{-2}. A total of 21 model runs are shown; three Burger number configurations each run with seven wind stress magnitudes ranging from 20–140% of τ_o. The solid line plotted for reference is theoretical scaling of cross-shelf transport with wind stress. Flux ratios are averaged from day 10–15.

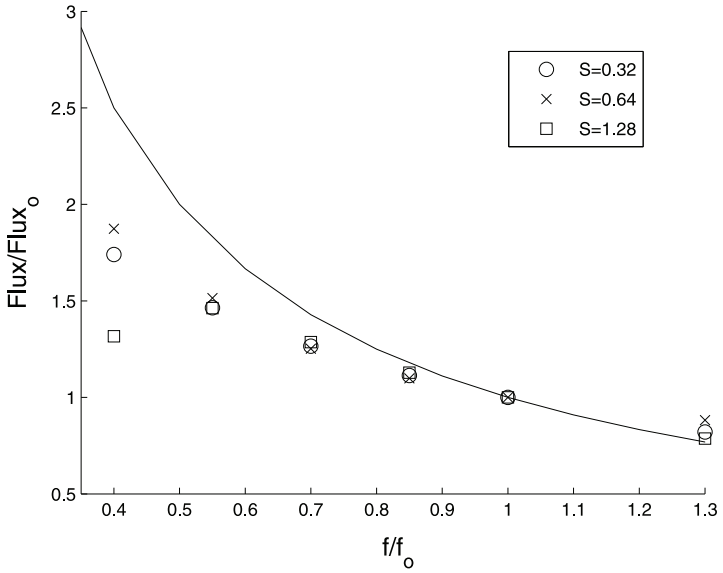

Figure 11. Scaling of BBL nitrate flux relative to Coriolis frequency. Scaling is performed as in Figure 10, with a base case of $f_o = 10^{-4}$ s^{-1}. Solid line indicates theoretical scaling of cross-shelf transport with Coriolis frequency. Note that Burger number values in the legend only apply to the base case, as Burger number changes with f.

fication concentrates transport in the BBL and steep slope allows deep water the shortest horizontal travel to reach the inner shelf. As a result, time scales for evolution of BBL nitrate flux increase with the ratio of N to α, from $T \approx 3$ days at $N/\alpha = 0.4$ s^{-1} to $T \approx 12$ days at $N/\alpha = 10$ s^{-1}. In the interior, source depths are shallower than those in the BBL, and nitrate flux is not quickly limited by the nitrate maximum at 200 m depth. For cases with significant interior nitrate flux ($S \geq 0.6$), time scales for nitrate flux evolution are fairly steady, with $T = 19.4 \pm 3.3$ days. Time scales for evolution of the BBL and interior source depth were also empirically determined and are $T = 17.6 \pm 2.6$ days and $T = 10.7 \pm 1.1$ days, respectively.

[29] Figure 5 shows fluxes produced by the numerical and analytical (equation (8)) models. Not surprisingly, maximum BBL nitrate flux is greatest with weak slope and stratification. Given sufficient time, BBL transport draws from below the nitrate maximum in all cases. Maximum BBL flux is therefore dependent on the fraction of onshore transport occurring in the BBL, shown by LC to decrease as αN increases. The analytical model overestimates BBL fluxes in the case of weakest slope and stratification ($\alpha = 0.002$, $N = 0.004$ s^{-1}) where an extremely thick BBL results in low onshore velocities even though total BBL transport is high. Consequently, deep nitrate-rich water reaches the inner shelf slowly. Agreement is good through the rest of the parameter range. As interior transport increases with αN, so does maximum interior nitrate flux. At $\alpha N = 0$, onshore flow occurs entirely in the BBL and interior nitrate flux vanishes. At $\alpha N = 2 \times 10^{-4}$ s^{-1} ($S = 2$ in our experiments), maximum steady state nitrate flux in the interior approaches 20 mmol s^{-1}, about two thirds the maximum BBL flux as S approaches zero.

[30] For constant wind stress and Coriolis frequency, maximum BBL source depth is set by stratification (Table 2). In contrast, maximum interior source depth is determined primarily by slope. The influence of slope is seen clearly on day 10 and day 20 (Figure 9), though stratification appears to become more important with time. If the empirical model were based on longer model runs, stratification would likely emerge in the interior source depth parameterization. Source depth estimates based on equation (9) and parameters in Table 2 are shown in Figure 8 and agree well with estimates obtained from the numerical model.

Table 2. Parameters for Analytical Nitrate Flux and Source Depth Expressions[a]

Modeled Parameter	F_0 or d_0 (mmol s^{-1} or m)	F_m or d_m (mmol s^{-1} or m)	T (days)
BBL NO_3 Flux	1.6 ± 0.8	$27.6e^{-\alpha N/5.1\times10^{-5}} + 5.7$	$11.9e^{-\alpha/0.45N} + 2.9$
Interior NO_3 Flux	0	$19.2(1 - e^{-\alpha N/9.4\times10^{-5}})$	19.4 ± 3.3
BBL Source Depth	20.5 ± 4.7	$495e^{-N/0.0080} + 182$	17.6 ± 2.6
Interior Source Depth	0	$104e^{-0.0058/\alpha} + 65$	10.7 ± 1.1

[a] F_o relates to flux parameters and d_o relates to source depth parameters. Similarly, F_m and d_m relate to flux parameters and source depth parameters, respectively. All expressions assume $f = 10^{-4}$ s^{-1}.

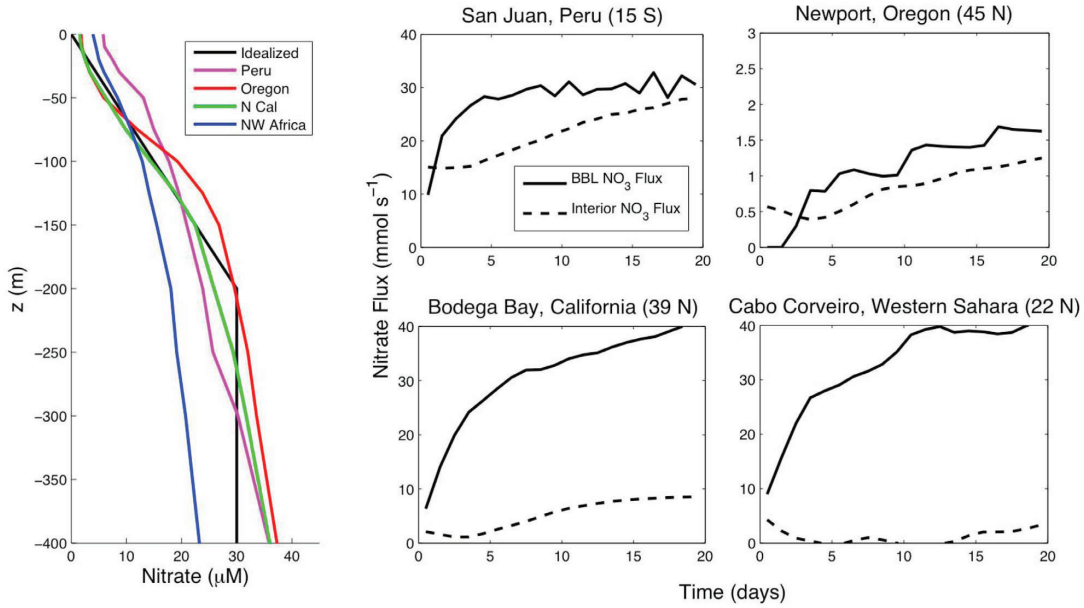

Figure 12. Idealized 2-D numerical model applied to global upwelling regions. (left) Annual average nitrate profiles for each region, gathered from the World Ocean Atlas 2005 database. Other parameters for each case (latitude, stratification, slope, wind stress) are outlined in Table 1. (right) Interior and BBL fluxes calculated from model output for each region. Note the scale for Oregon is different from the other cases.

[31] While equation (8) is able to accurately describe modeled nitrate fluxes, it is based on an idealized initial nitrate profile. To generalize the application of the empirical model to varied nitrate profiles, we represent nitrate flux as the product of theoretical steady state transport in the BBL or interior (U_{BBL} or U_{INT}) and initial nitrate concentration at a characteristic source depth ($[NO_3]_S$), obtained from the numerical model

$$F = U[NO_3]_S \tag{10}$$

$$U_{BBL} = \frac{\tau}{\rho_0 f}\frac{1 - S/2}{1 + S/2} \qquad U_{INT} = \frac{\tau}{\rho_0 f}\frac{S}{1 + S/2}. \tag{11}$$

LC derived equation (11), where τ is alongshore surface wind stress and ρ_0 is a reference density. This form has the advantage of being applied to any initial nitrate profile, based on the source depth evolution (equation (9)). Application of equations (10) and (11) to our test cases is shown in Figure 6 along with calculated nitrate fluxes. In these model runs, the idealized linear nitrate profile was replaced with a real profile taken off the Oregon coast. Agreement is good for interior flux estimates at all but the highest Burger numbers, and for BBL estimates on $0.16 \leq S \leq 1.2$. At high Burger numbers, divergence of modeled BBL transport from LC theory (Figure 2) causes the empirical model to underestimate BBL nitrate flux and overestimate the interior contribution.

4.3. Global Upwelling Regions

[32] Between the four EBC locations studied by LC, Coriolis and buoyancy frequencies vary almost threefold, shelf slopes change by a factor of six, and there is nearly an order of magnitude range in Burger number. It is reasonable that these parameters should strongly influence the productivity of upwelling regions and the differences between them. In order to investigate the simplified model in real upwelling systems, model runs were performed for the four locations described in LC. Stratification and topographic slope are still constant, but have magnitudes representative of each location. Surface forcing is also idealized, with no spatial or temporal variability, but its magnitude is determined from QuikSCAT data. For each location, we use daily wind stress for 2007–2008, and take the mean alongshore component from a three month upwelling season. Realistic nitrate profiles for each region are obtained from the World Ocean Atlas 2005 Database annual averages [*Garcia et al.*, 2006]. Figure 12 and Table 1 outline the input parameters for all cases. Results from the idealized model with the given configurations are shown in Figure 12. It is important to note that each case is a discrete location within an upwelling system, and is not representative of the system as a whole.

[33] Substantial differences in BBL and interior nitrate flux contributions between several upwelling sites are apparent. The two high Burger number locations, off Peru and Oregon, show significant contributions from the interior. BBL and interior fluxes off Peru are comparable over the first 20 days,

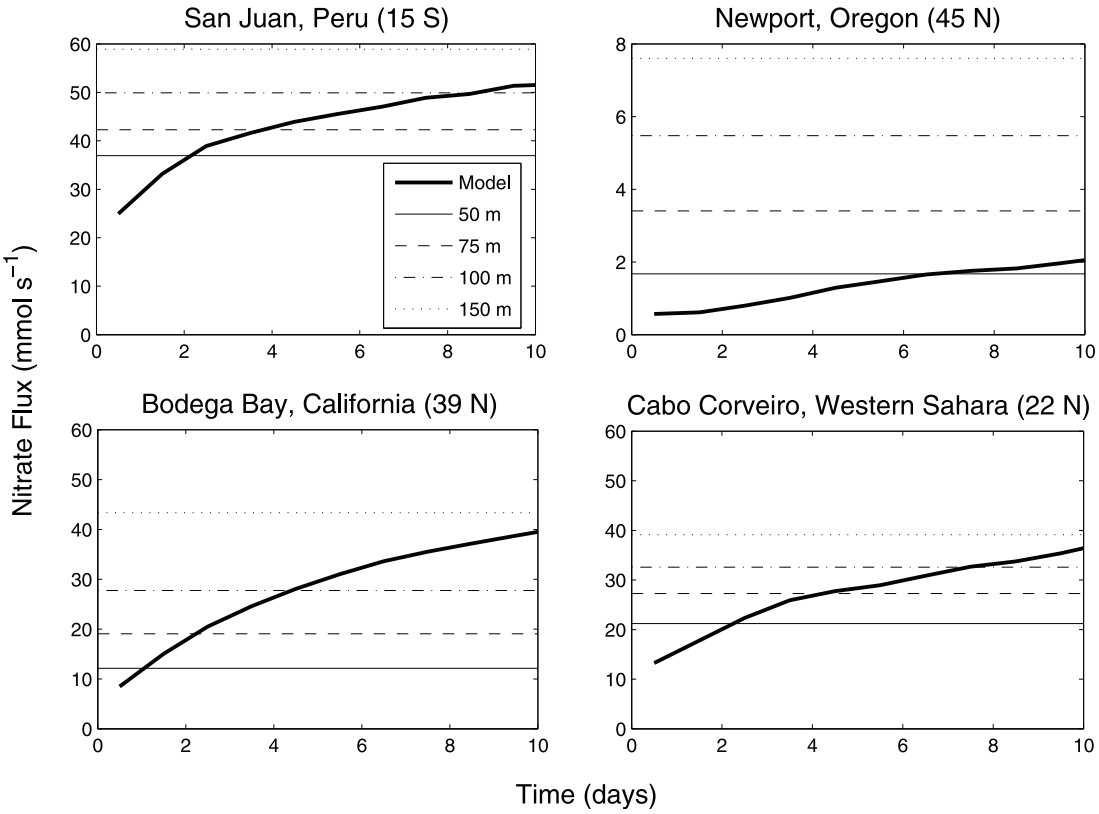

Figure 13. Total (interior and BBL) advective nitrate flux for locations in major global upwelling regions. Thick lines represent numerical model output. Additional estimates (thin lines) are calculated as the product of theoretical Ekman transport and nitrate concentration at various source depths. Ekman transport is estimated based on parameters in Table 1. Nitrate concentrations at 50, 75, 100, and 150 m depths come from the World Ocean Atlas 2005 database. Note the scale for Oregon is different from the other cases.

with steady BBL flux after a brief initial spin-up and interior flux that rises slightly with time. Nitrate concentration off Peru is relatively high in the upper 50 m, allowing rapid transport to the SML by strong interior flow. Interior and BBL nitrate fluxes are also comparable to each other at the Oregon site; however both are very low in magnitude due to the weak surface forcing used in the model. It should be noted that on an event scale, surface wind stress off Oregon can often reach 0.1–0.2 N m^{-2}, much higher than the mean value of 0.03 N m^{-2} used here. Nitrate fluxes associated with the higher event-scale wind stress could reach values on par with the other three locations shown in Figure 12. In contrast with the Peru and Oregon sites examined, the northern California and northwest Africa sites are dominated by BBL nitrate flux, with a negligible interior contribution in the latter case. Also, while Ekman transport off northern California is significantly less than that off northwest Africa (based on wind stress and latitude in Table 1), their BBL nitrate fluxes are approximately equal owing to the much richer deep nitrate stock of the Pacific relative to the Atlantic. At model day 10, total nitrate advection is highest at the Peru site (~50 mmol s^{-1}), slightly lower at the northern California and northwest Africa locations (~40 mmol s^{-1}), and much lower off Newport, Oregon (~2 mmol s^{-1}). Though transport in the Canary Current case is strong and entirely in the BBL, total flux is limited by low nitrate concentrations in the deep north Atlantic and a very weakly sloping shelf that makes deep water available only far offshore.

[34] Figure 13 illustrates nitrate flux dependence on upwelling source depth. During much of the first 10 days of upwelling, nitrate fluxes at our Peru and northwest Africa sites are bracketed by estimates using source depths of 50 m and 100 m. In comparison, source depth off northern California increases rapidly due to strong surface forcing, while the opposite is true in the weakly forced Newport, Oregon case. As reported elsewhere [*Messié et al.*, 2009], nitrate flux estimates in the California Current are much more sensitive to choice of source depth than either the Peru or Canary Currents. The increase in nitrate flux estimated using 100 m source depth compared to 50 m, for example, is highly dependent on region. In our test cases off Peru and northwest Africa, differences are 13.0 mmol s^{-1} (35%) and

11.4 mmol s^{-1} (54%), respectively. In the California Current, differences are 15.6 mmol s^{-1} (129%) for northern California and 3.8 mmol s^{-1} (228%) for Oregon.

5. Discussion

[35] *Lentz and Chapman* [2004] demonstrated that the structure of cross-shelf flow during upwelling is dependent on a topographic Burger number. As Burger number increases, bottom stress decreases and onshore transport shifts from the BBL to the interior of the water column. These findings motivated our investigation into the resulting impacts on nutrient supply in upwelling regions. For example, how do nutrient fluxes in strongly stratified, high-latitude waters off Oregon differ from those in weakly stratified, low-latitude waters over the steep continental shelf of Peru?

[36] The suite of numerical model simulations described here shows the dependence of interior, BBL, and total nitrate flux on topographic slope, stratification, wind stress, and latitude. The distinction of interior and BBL transport allows quantification of nitrate fluxes to discrete cross-shelf regions in the upwelling zone. Specifically, BBL transport supplies the inner shelf while interior transport supplies the mid- and outer shelf. For an idealized initial nitrate profile, interior and BBL advective nitrate fluxes vary with Burger number. Low Burger numbers produce a greater fraction of transport, and consequently nitrate flux, in the BBL while higher Burger numbers increase the interior contribution. Consequently, the inner shelf, often characterized by high productivity and retention inshore of the upwelling front, may be favored for production in low Burger number regions with a large fraction of onshore transport in the BBL. In contrast, strong stratification and a steeply sloping shelf may produce a relatively small inner shelf region with less nutrient input to fuel potential production. Vertical diffusion is a relatively small contributor to nitrate flux, but is greater in weakly stratified systems. Increased surface nitrate due to mixed layer deepening is greatest in weakly stratified cases, which produce the deepest mixed layers. It is also greater in steep slope cases where high nitrate is carried to the base of the SML by strong interior flow and subsequently entrained. These results are not specific to any particular region, but provide insight into how nitrate supply is affected by physical parameters that govern many upwelling systems.

[37] Observations, theory, and numerical model results show distinct bottom and interior cross-shelf flow regimes [*Smith*, 1981; *Lentz and Chapman*, 2004] and during sustained upwelling, source depths for each of these regimes increase with time (Figure 8). However, observational studies of upwelling fluxes are generally limited to choosing a single characteristic source depth for a given region [e.g., *Chavez and Barber*, 1987; *Walsh*, 1991; *Messié et al.*, 2009]. The sensitivity of nitrate flux to upwelling source depth is dependent on the local nitrate profile in the region of interest. On an event time scale of days, we find that source depth estimates of 50–100 m appear reasonable for all locations, though the northern California site reaches these depths quickly while the weak forcing used off Oregon produces relatively shallow source water (Figure 13). A thorough analysis of appropriate source depth for a given upwelling region should therefore consider not only physical characteristics of the region but also temporal variability of surface winds. Spectral analysis of the wind field at a given location would inform the choice of source depth by indicating a typical upwelling duration. Based on the intersection of offshore and inshore T-S diagrams, *Messié et al.* [2009] note typical upwelling source depths of 75, 60, and 100 m for the Peru, California, and Canary systems, respectively.

[38] The model runs described in section 4.3 examine upwelling fluxes at several discrete locations in major upwelling systems. Though separated by less than 1000 km, our two California Current sites (near Bodega Bay, California and Newport, Oregon) differ drastically in terms of modeled nitrate flux. The largest difference between the two is the magnitude of nitrate flux, which can be attributed to surface forcing. The mean upwelling favorable wind stress used to force our model is 0.18 N m^{-2} off northern California, compared to just 0.03 N m^{-2} off central Oregon. On an event scale, however, wind stress at Newport, Oregon can reach 0.1–0.2 N m^{-2}, producing nitrate fluxes similar to those modeled at our northern California site. In either case, the two locations differ significantly in the structure of onshore flow. Strong stratification off Newport, Oregon produces a Burger number more than double that at the northern California site. Consequently, there is substantial onshore transport in the interior off Oregon, and very little off northern California. It should be noted that while our chosen California Current sites show a steeper shelf off Oregon than northern California, this is actually counter to the general latitudinal trend in shelf width from California to Washington [*Hickey and Banas*, 2008]. Thus, selection of different sites could result in a higher Burger number off northern California, a lower Burger number off Oregon, and much more similar structures in cross-shelf transport. At both locations, and especially Newport, upwelling favorable winds persist over much less of the year than at the Peru and northwest Africa sites. The event-scale nitrate fluxes depicted in Figure 12 are therefore likely to be limited to the relatively short and intense spring/summer upwelling season. Also, the persistence of upwelling favorable alongshore winds is rarely longer than 10 days between relaxations or reversals [*Kudela et al.*, 2006], so upwelling source depth may be unlikely to reach the depths indicated by our model beyond 10 days.

[39] It is well known from previous modeling [*McCreary*, 1981; *Federiuk and Allen*, 1995] and observational [*Allen and Smith*, 1981; *Lentz*, 1994] studies that an alongshore pressure gradient, resulting from a poleward decrease in sea surface height, can modify dynamics of eastern boundary upwelling systems. LC have shown that for a given Burger number, bottom stress is reduced by an alongshore pressure gradient consistent with a poleward decrease in sea surface height, and for a given alongshore pressure gradient, the relative change to the bottom stress is larger for smaller Burger numbers. Our model does not include this effect but we consider here its qualitative impact. A reduction in bottom stress reduces BBL transport, effectively shifting the partitioning of onshore transport from the BBL to the interior. As a result, we expect the addition of an alongshore pressure gradient to be qualitatively similar, with respect to nutrient fluxes, to an increase in Burger number. The magnitude of this effect and its quantitative significance are left to a further study.

[40] The Canary Current site discussed in LC and used here to initialize the 'NW Africa' model has the lowest Burger

number (S = 0.19) of the four locations, due largely to its very weakly sloping shelf. At such low Burger number, approximately 90% of modeled transport occurs in the BBL (Figure 2), promoting efficient upwelling of macronutrients and in nature, potentially iron. *Messié et al.* [2009] show a strong latitudinal gradient at ~21°N for both nitrate at 60 m and estimated nitrate supply in the Canary Current. To the south, nitrate at 60 m reaches 20 μmol L^{-1} and nitrate flux due to coastal upwelling is 20–25 mmol s^{-1}. To the north, nitrate at 60 m drops to near zero and nitrate flux is ~5 mmol s^{-1}. Our Canary Current model is configured at 22°N, near the border of the north and south regions. While modeled fluxes (Figure 13) indicate this location is more representative of the south than the north, it likely underestimates nitrate fluxes south of 20°N. *Barton et al.* [1977] describe the offshore movement of the upwelling core in the Canary Current near Cabo Corveiro, where the coldest waters are initially near shore (as in our model), but migrate offshore with sustained upwelling favorable winds. The upwelling core ultimately remains at the shelf break (~100 m water depth) and inshore of this is a retentive and highly productive region [*Estrade et al.*, 2008]. Our linearized topography is unable to represent the impact of the shelf break; however the model does show a rapid offshore movement of the upwelling front given the slope and stratification at our northwest Africa location (Figure 4).

[41] Due to its low latitude and steep shelf, the Peru site has the highest Burger number of the four investigated here. Consequently, the interior contribution to nitrate flux is greater in this case than any other. At the Burger number of this site (S = 1.35), approximately 80% of volume transport is concentrated in the interior of the water column (Figure 2), and about half of all nitrate flux derives from the interior (Figure 12). The nitrate profile at our Peru location differs from the other regions in that high nitrate is available close to the surface. Following the onset of upwelling favorable winds, this nitrate is readily available and rapidly enters the SML from both the interior and BBL. In the first day of upwelling, advective nitrate flux off Peru is double that of any of the other locations. In brief periods of upwelling winds, this region may be able to fuel more production than others. However, the large fraction of interior transport may lead to conditions with insufficient iron available for efficient uptake of nitrate. As upwelling winds persist, source depth increases, but nitrate flux is affected little due to a relatively weak vertical nitrate gradient. Consequently, nitrate fluxes based on a constant source depth model are not particularly sensitive to selection of upwelling source depth.

[42] Not accounted for in our model are the shelf break and continental slope, both important components of boundary topography. It is interesting to speculate on how their inclusion may influence our results. The bottom slope is much greater over the continental slope than it is on the continental shelf; deep water offshore of the shelf break is therefore horizontally closer to shore than in our model. Upwelling circulation that draws from beyond the shelf break should reduce the time scale for deep water reaching the SML and increase overall nitrate flux. However, this effect may be complicated by changed upwelling dynamics near the shelf break, such as those outlined in the northwest Africa case. We leave quantitative evaluation of these effects to further study.

[43] While comparisons of modeled nitrate fluxes in the present analysis to ecosystem-scale studies of potential and observed productivity [*Carr*, 2002; *Carr and Kearns*, 2003; *Messié et al.*, 2009] are tempting, there are several important caveats in doing so: (1) our model experiments each represent an idealized 2-D approximation to a coastline with variable bathymetry and 3-D circulation (our topography omits important features such as the shelf break, continental slope, capes, and canyons); (2) each model run represents a single location within an upwelling ecosystem and not some average of the entire ecosystem; (3) this approach focuses on nitrate upwelling dynamics on an event scale, not a seasonal, annual, or interannual scale; (4) we do not consider upwelling driven by wind stress curl, whose contribution is uncertain, with estimates ranging from small [*Messié et al.*, 2009] to equal or greater than coastal upwelling [*Pickett and Paduan*, 2003; *Dever et al.*, 2006; *Rykaczewski and Checkley*, 2008]; and (5) only new production is supported by upwelled nitrate, not total primary production. The ratio of new to total primary production (the f ratio) may vary among upwelling regions based on factors such as light availability, mixed layer depth, limitation by other nutrients [*Messié et al.*, 2009], and wind speed [*Botsford et al.*, 2003]. Results presented here cannot characterize entire upwelling ecosystems in a spatially and temporally averaged sense, but do illustrate some differences between them.

[44] The analytical expressions presented in section 4.2 come from the combination of a previously developed steady state transport theory (LC) and diagnostics from our numerical model. Nitrate flux and source depth predicted by the diagnostic model are presented for ranges of shelf slope and stratification that cover those encountered in major global upwelling regions. Though empirical, the analytical model works well throughout most of the range of Burger numbers tested and has several benefits. First, it provides estimates of time-dependent nitrate (or other macronutrient) flux in upwelling regions as a function of topographic slope, stratification, and initial nutrient profile. Second, the asymptotic form of the analytic expressions allows for steady state estimates of flux and source depth. Third, it provides a basis for qualitative comparison of potential new production among upwelling regions based on their physical properties. Fourth, expressions for source depth can be applied to questions beyond nitrate flux, such as micronutrient supply. It is important to note that fluxes into the SML after 2 days of sustained upwelling are not equal to those after 10 days. Here, this temporal development is represented.

[45] In addition to comparisons between upwelling regions, one can apply the present approach to change in one region over time. Based on long-term temperature records in the CCS, *Palacios et al.* [2004] found increased thermal stratification near the coast from 1950–1993, presumably inhibiting upwelling of nutrients. However, increased upwelling-favorable winds due to greenhouse gas forcing have been hypothesized [*Bakun*, 1990] and supported in the CCS by observations [*Schwing and Mendelssohn*, 1997]. *Di Lorenzo et al.* [2005] concluded that any upwelling increase due to strengthened upwelling favorable winds over the last 50 years has been negated by increased stratification and thermocline deepening in the CCS. *Auad et al.* [2006] found the opposite in future projections, with an overall increase in upwelling due to dominance of increased upwelling favorable

winds. *García-Reyes and Largier* [2010] noted increased upwelling along the central California coast from 1982–2008. While it is beyond the scope of this paper, the idealized model could be configured with either past or projected winds, stratification, and nitrate profiles to provide an alternate prediction.

[46] Further, our idealized model approach may be applied to a number of questions not addressed here. The first, which has been discussed briefly, is the impact of shelf slope and stratification on micronutrient supply. *Johnson et al.* [1999] found that the primary source of iron in the CCS is resuspension and subsequent upwelling of particles in the BBL. As such, we expect upwelling sites with substantial onshore flow along the sediments to be iron replete. In areas of high Burger number and interior flow, iron limitation may curb productivity. One example is the contrast of the wide shelf and iron-replete conditions from Monterey Bay to Pt. Reyes with the narrow shelf and iron-deplete conditions off the Big Sur coast south of Monterey Bay [*Bruland et al.*, 2001]. A second question relates to hypoxia at upwelling sites. Hypoxic conditions have been frequently observed in the CCS over both the Oregon and Washington continental shelves [*Chan et al.*, 2008; *Connolly et al.*, 2010] and could be related to upwelling circulation. For example, strong stratification may produce onshore transport concentrated in the interior, thus limiting ventilation of bottom waters over the continental shelf and promoting hypoxia near the bottom. Alternatively, strong and prolonged BBL transport may entrain low-oxygen waters from the continental slope onto the shelf. Finally, the structure of cross-shelf flow has implications for redistribution of phytoplankton communities from the sediments and within the water column. During unfavorable growth conditions, mass sinking can be a survival mechanism for diatoms that remain viable longer in cold, dark water than warm, nutrient depleted water [*Smetacek*, 1985]. Dinoflagellates also react to unfavorable conditions by sinking, through the formation of nonmotile cysts. In high Burger number regions, sinking cells may find adequate nutrients and light just below the SML, as well as onshore flow that keeps cells entrained near the coast [*Batchelder et al.*, 2002]. Cells that sink to the sea floor may ultimately be carried onshore by BBL flow more efficiently in low Burger number regions. In either case, the structure of onshore flow could play an important role in transporting a small seed population to the SML when favorable growth conditions return.

[47] **Acknowledgments.** We gratefully acknowledge funding from the Gordon and Betty Moore Foundation and National Science Foundation grant OCE-0726858. Comments from two anonymous reviewers greatly improved the manuscript. We also thank Jon Zehr, Raphael Kudela, Jenny Lane, and Ryan Paerl for helpful discussions.

References

Allen, J. S., and R. L. Smith (1981), On the dynamics of wind-driven shelf currents, *Philos. Trans. R. Soc. A*, *302*, 617–634.

Allen, J. S., P. A. Newberger, and J. Federiuk (1995), Upwelling circulation on the Oregon continental shelf. Part I: Response to idealized forcing, *J. Phys. Oceanogr.*, *25*, 1843–1866.

Auad, G., A. Miller, and E. Di Lorenzo (2006), Long-term forecast of oceanic conditions off California and their biological implications, *J. Geophys. Res.*, *111*, C09008, doi:10.1029/2005JC003219.

Austin, J. A., and S. J. Lentz (2002), The inner shelf response to wind-driven upwelling and downwelling, *J. Phys. Oceanogr.*, *32*, 2171–2193.

Bakun, A. (1990), Global climate change and intensification of coastal ocean upwelling, *Science*, *247*, 198–201.

Barton, E. D., A. Huyer, and R. L. Smith (1977), Temporal variation observed in the hydrographic regime near Cabo Corveiro in the northwest African upwelling region, February to April 1974, *Deep Sea Res.*, *24*, 7–23.

Batchelder, H. P., C. A. Edwards, and T. M. Powell (2002), Individual-based models of copepod populations in coastal upwelling regions: Implications of physiologically and environmentally influenced diel vertical migration on demographic success and nearshore retention, *Prog. Oceanogr.*, *53*, 307–333.

Botsford, L W., C. A. Lawrence, E. P. Dever, A. Hastings, and J. L. Largier (2003), Wind strength and biological productivity in upwelling systems: An idealized study, *Fish. Oceanogr.*, *12*, 245–259.

Bruland, K. W., E. L. Rue, and G. J. Smith (2001), Iron and macronutrients in California coastal upwelling regimes: Implications for diatom blooms, *Limnol. Oceanogr.*, *46*, 1661–1674.

Carr, M. E. (2002), Estimation of potential productivity in eastern boundary currents using remote sensing, *Deep Sea Res. Part II*, *49*, 59–80.

Carr, M. E., and E. J. Kearns (2003), Production regimes in four eastern boundary current systems, *Deep Sea Res. Part II*, *50*, 3199–3221.

Chan, F., J. A. Barth, J. Lubchenco, A. Kirincich, H. Weeks, W. T. Peterson, and B. A. Menge (2008), Emergence of anoxia in the California Current large marine ecosystem, *Science*, *319*, 920.

Chapman, D. C., and S. J. Lentz (2005), Acceleration of a stratified current over a sloping bottom, driven by an alongshelf pressure gradient, *J. Phys. Oceanogr.*, *35*, 1305–1317.

Chavez, F. P., and R. T. Barber (1987), An estimate of new production in the equatorial Pacific, *Deep Sea Res. Part A*, *34*, 1229–1243.

Chavez, F. P., and M. Messié (2009), A comparison of eastern boundary upwelling ecosystems, *Prog. Oceanogr.*, *83*, 80–96, doi:10.1016/j.pocean.2009.07.032.

Chavez, F. P., and J. R. Toggweiler (1995), Physical estimates of global new production: The upwelling contribution, in *Upwelling in the Ocean: Modern Processes and Ancient Records*, edited by C. P. Summerhayes et al., pp. 313–320, John Wiley, New York.

Connolly, T. P., B. M. Hickey, S. L. Geier, and W. P. Cochlan (2010), Processes influencing seasonal hypoxia in the northern California Current System, *J. Geophys. Res.*, *115*, C03021, doi:10.1029/2009JC005283.

Dever, E. P., C. E. Dorman, and J. L. Largier (2006), Surface boundary layer variability off northern California, USA during upwelling, *Deep Sea Res. Part II*, *53*, 2887–2905.

Di Lorenzo, E., A. J. Miller, N. Schneider, and J. C. McWilliams (2005), The warming of the California Current System: Dynamics and ecosystem implications, *J. Phys. Oceanogr.*, *35*, 336–362.

Dugdale, R. C., and J. J. Goering (1967), Uptake of new and regenerated forms of nitrogen in primary productivity, *Limnol. Oceanogr.*, *12*, 196–206.

Estrade, P., P. Marchesiello, A. Colin de Verdiere, and C. Roy (2008), Cross-shelf structure of coastal upwelling: A two-dimensional expansion of Ekman's theory and a mechanism for innershelf upwelling shut down, *J. Mar. Res.*, *66*, 589–616.

Federiuk, J., and J. S. Allen (1995), Upwelling circulation on the Oregon continental shelf. Part II: Simulations and comparisons with observations, *J. Phys. Oceanogr.*, *25*, 1867–1889.

Garcia, H. E., R. A. Locarnini, T. P. Boyer, and J. I. Antonov (2006), *World Ocean Atlas 2005*, vol. 4, *Nutrients (Phosphate, Nitrate, and Silicate), NOAA Atlas NESDIS*, vol. 64, edited by S. Levitus, 396 pp., NOAA, Silver Spring.

García-Reyes, M., and J. Largier (2010), Observations of increased wind-driven coastal upwelling off central California, *J. Geophys. Res.*, *115*, C04011, doi:10.1029/2009JC005576.

Haidvogel, D. B., et al. (2008), Ocean forecasting in terrain-following coordinates: Formulation and skill assessment of the Regional Ocean Modeling System, *J. Comput. Phys.*, *227*, 3595–3624.

Hickey, B. M., and N. S. Banas (2008), Why is the northern end of the California Current System so productive?, *Oceanography*, *21*(4), 90–107.

Johnson, K. S., F. P. Chavez, and G. E. Friederich (1999), Continental-shelf sediment as a primary source of iron for coastal phytoplankton, *Nature*, *398*, 697–700.

Kudela, R. M., N. Garfield, and K. W. Bruland (2006), Bio-optical signatures and biogeochemistry from intense upwelling and relaxation in coastal California, *Deep Sea Res. Part II*, *53*, 2999–3022.

Laanemets, J., V. Zhurbas, J. Elken, and E. Vahtera (2009), Dependence of upwelling-mediated nutrient transport on wind forcing, bottom topography and stratification in the Gulf of Finland: Model experiments, *Boreal Environ. Res.*, *14*, 213–225.

Large, W. G., J. C. McWilliams, and S. C. Doney (1994), Oceanic vertical mixing: A review and a model with a vertical K-profile boundary layer parameterization, *Rev. Geophys.*, *32*, 363–403.

Lentz, S. J. (1992), The surface boundary layer in coastal upwelling regions, *J. Phys. Oceanogr.*, *22*, 1517–1539.

Lentz, S. J. (1994), Current dynamics over the northern California inner shelf, *J. Phys. Oceanogr.*, *24*, 2461–2478.

Lentz, S. J., and D. C. Chapman (2004), The importance of non-linear cross-shelf momentum flux during wind-driven coastal upwelling, *J. Phys. Oceanogr.*, *34*, 2444–2457.

McCreary, J. P. (1981), A linear stratified ocean model of the coastal undercurrent, *Philos. Trans. R. Soc. A*, *302*, 385–413.

Messié, M., J. Ledesma, D. D. Kolber, R. P. Michisaki, D. G. Foley, and F. P. Chavez (2009), Potential new production estimates in four eastern boundary upwelling ecosystems, *Prog. Oceanogr.*, *83*, 151–158, doi:10.1016/j.pocean.2009.07.018.

Palacios, D. M., S. J. Bograd, R. Mendelssohn, and F. B. Schwing (2004), Long-term and seasonal trends in stratification in the California Current, 1950–1993, *J. Geophys. Res.*, *109*, C10016, doi:10.1029/2004JC002380.

Pauly, D., and V. Christensen (1995), Primary production required to sustain global fisheries, *Nature*, *374*, 255–257.

Pickett, M. H., and J. D. Paduan (2003), Ekman transport and pumping in the California Current based on the U.S. Navy's high-resolution atmospheric model (COAMPS), *J. Geophys. Res.*, *108*(C10), 3327, doi:10.1029/2003JC001902.

Pollard, R., P. B. Rhines, and R. O. R. Y. Thompson (1973), The deepening of the wind-mixed layer, *Geophys. Fluid Dyn.*, *3*, 381–404.

Rykaczewski, R. R., and D. M. Checkley (2008), Influence of ocean winds on the pelagic ecosystem in upwelling regions, *Proc. Natl. Acad. Sci.*, *105*, 1965–1970.

Schwing, F. B., and R. Mendelssohn (1997), Increased coastal upwelling in the California current system, *J. Geophys. Res.*, *102*, 3421–3438.

Shchepetkin, A. F., and J. C. McWilliams (2005), The Regional Ocean Modeling System: A split-explicit, free-surface, topography following coordinates ocean model, *Ocean Modell.*, *9*, 347–404.

Smetacek, V. S. (1985), Role of sinking in diatom life-history cycles: Ecological, evolutionary and geological significance, *Mar. Biol.*, *84*, 239–251.

Smith, R. L. (1981), A comparison of the structure and variability of the flow field in three coastal upwelling regions: Oregon, Northwest Africa, and Peru, in *Coastal Upwelling*, pp. 107–118, edited by F. A. Richards, AGU, Washington, D. C.

Umlauf, L., and H. Burchard (2003), A generic length-scale equation for geophysical turbulence models, *J. Mar. Res.*, *61*, 235–265.

Walsh, J. J. (1991), Importance of continental margins in the marine biogeochemical cycling of carbon and nitrogen, *Nature*, *350*, 53–55.

C. A. Edwards and M. G. Jacox, Department of Ocean Science, University of California, Santa Cruz, 1156 High St., Santa Cruz, CA 95062, USA. (mjacox@ucsc.edu)

CHAPTER TWO

Upwelling source depth in the presence of nearshore wind stress curl

M. G. Jacox[1] and C. A. Edwards[1]

Received 27 December 2011; revised 16 March 2012; accepted 17 March 2012; published 5 May 2012.

[1] The influence of nearshore wind stress curl on the relative partitioning of bottom boundary layer (BBL) and interior transport within an idealized, two-dimensional coastal upwelling system is studied theoretically and using a numerical model. A nearshore reduction in upwelling favorable wind stress amplitude (1) reduces the width of the inner shelf, (2) reduces the local wind-driven Ekman transport, and (3) increases the cross-shelf momentum flux divergence. Relative BBL transport, defined as the transport entering the surface mixed layer (SML) from the BBL divided by offshore transport in the SML, decreases under reduced nearshore wind stress. This effect is dominated by the reduced local SML Ekman transport and to a lesser degree by local curl of surface and bottom stresses. We consider the quantitative impact for a range of shelf slopes, stratifications, and wind stress curl scales. The relative contribution of bottom boundary layer transport co-varies with upwelling source depth and is therefore expected to alter nutrient fluxes into the euphotic zone as well as the resultant biological response.

Citation: Jacox, M. G., and C. A. Edwards (2012), Upwelling source depth in the presence of nearshore wind stress curl, *J. Geophys. Res.*, *117*, C05008, doi:10.1029/2011JC007856.

1. Introduction

[2] Wind-driven upwelling of nutrient-rich subsurface water in eastern boundary currents (EBCs) may be forced by two mechanisms; coastal divergence in the surface layer due to equatorward winds at the coast, and Ekman pumping driven by cyclonic wind stress curl. The coastal divergence component (also referred to simply as coastal upwelling in this paper) occurs in a relatively narrow band next to the coast, resulting in strong vertical velocities nearshore. Ekman pumping (also referred to as curl-driven upwelling) may extend far offshore, driving lower upwelling velocities over a much larger area (up to 200–300 km in the California Current System (CCS) [*Pickett and Paduan*, 2003]). In the nearshore region of strong coastal upwelling, Ekman pumping is generally thought to be of little importance except in the vicinity of significant coastal promontories, where wind stress curl may produce upwelling rates on the same order as those due to alongshore winds [*Koracin et al.*, 2004]. Offshore of the narrow coastal band, weaker curl-driven upwelling dominates and vertical transport driven by the two components are of the same order when integrated over the entire upwelling region [*Enriquez and Friehe*, 1995; *Pickett and Paduan*, 2003; *Rykaczewski and Checkley*, 2008].

[3] Several studies have addressed the influence of nearshore curl not only on upwelling transport, but also on source waters and nutrient flux. In observations off Bodega Bay, CA, *Dever et al.* [2006] estimated curl-driven vertical nitrate flux divergence to be about half that due to alongshore winds at the coastal boundary, and total nitrate flux integrated over the area of positive curl to be several times higher than that from coastal upwelling. *Capet et al.* [2004] studied the upwelling response to two wind profiles in a realistic model off Central California; one with a much stronger nearshore drop-off in wind stress. They tracked vertical displacement of Lagrangian tracers in each case, and found that upwelling in the upper 100 m is primarily associated with intense, localized coastal upwelling, not vertically and horizontally distributed Ekman pumping. *Messié et al.* [2009] calculated nitrate fluxes in all four major EBCs from QuikSCAT winds and in-situ nitrate profiles, and estimated the curl-driven contribution to upwelled nitrate at just 21.5–31.4%. Conversely, in models of the Peru and California coasts, respectively, *Albert et al.* [2010] and *Song et al.* [2011] conclude that reduced equatorward winds nearshore (cyclonic wind stress curl) cause a shoaling of the nutrient-rich poleward undercurrent, increasing nutrient flux overall.

[4] Surface winds are routinely measured from a number of platforms, each valuable but with limitations. In situ measurements from moorings and aircraft are the most accurate, but data are sparse. Satellites offer much improved coverage, but data inshore of 25–50 km from the coast are unreliable and nearshore wind profiles are highly dependent on the satellite product used [*Croquette et al.*, 2007]. In modeled winds, the coastal curl band typically becomes stronger and narrower as resolution increases, and wind profiles do not necessarily converge at high resolution

[1]Department of Ocean Sciences, University of California, Santa Cruz, California, USA.

Corresponding Author: M. G. Jacox, Department of Ocean Science, University of California, 1156 High St., Santa Cruz, CA 95062, USA. (mjacox@ucsc.edu)

0148-0227/12/2011JC007856

Table 1. Parameters for Numerical Model Runs[a]

Run	α (10^{-3})	N (10^{-3} s^{-1})	S	ϵ (km)
1	2	4	0.08	0
2	2	12	0.24	0
3	2	20	0.40	0
4	6	4	0.24	0
5	6	12	0.72	0
6	6	20	1.2	0
7	10	4	0.40	0
8	10	12	1.2	0
9	10	20	2.0	0
10–18	2–10	4–20	0.08–2.0	10
19–27	2–10	4–20	0.08–2.0	20
28–36	2–10	4–20	0.08–2.0	40

[a]A total of 36 runs are represented to cover widely ranging shelf slope (α), stratification (N), and cross-shelf scale of wind stress curl (ϵ, as described by equation (2)). Runs 10–18, 19–27, and 28–36 are repeats of 1–9, except for changes in ϵ.

[*Capet et al.*, 2004]. Consequently, considerable uncertainty remains in the nearshore wind structure, and its variability in space and time.

[5] *Lentz and Chapman* [2004] demonstrated the dependence of cross-shelf transport structure on a topographic Burger number,

$$S = \frac{\alpha N}{|f|}. \tag{1}$$

The Burger number is dependent on the slope of the continental shelf, α, the buoyancy frequency, $N = \sqrt{(-g/\rho_0)\partial\rho/\partial z}$, where ρ is the fluid density, ρ_0 is a reference density and g is gravitational acceleration, and the Coriolis frequency, $f = 2\Omega\sin\phi$, where $\Omega = 7.29 \times 10^{-5}$ s^{-1} is Earth's rotation rate and ϕ is latitude. Low Burger numbers produce onshore flow concentrated in the bottom boundary layer (BBL), while increased Burger number shifts onshore flow to the interior. *Jacox and Edwards* [2011] investigated the influence of individual Burger number parameters on nutrient fluxes and source depth during upwelling and found results to be more complex than those for physical transport alone. The greatest source depths reached were in a weakly stratified water column with steeply sloping shelf. In both studies, however, only spatially uniform wind-forcing was considered. Here we use a simple idealized model, not specific to any particular region, to investigate the sensitivities of upwelling transport and source depth to changes in Burger number, two of its individual components (topography and stratification), and the structure of nearshore wind stress.

2. Methodology

[6] We use the Regional Ocean Modeling System (ROMS) [*Shchepetkin and McWilliams*, 2005] in a two-dimensional configuration (two alongshore grid points). Topographic bottom slope and initial stratification are spatially uniform for each model run and are varied between runs as outlined in Table 1. Further details of the model are presented in *Jacox and Edwards* [2011], which also notes several important model omissions such as a shelf break and an alongshore pressure gradient. The model configuration represents an oceanic eastern boundary and is illustrated schematically in Figure 1; here y is directed northward, x is directed eastward with $x = 0$ at the coastal boundary ($x < 0$ within the domain), and z is directed upward with the unperturbed ocean surface at z = 0. The ocean bottom is at depth $h = h_o - \alpha x$, where the coastal bottom depth h_o is assumed to be zero for purposes of the theory in section 3. It is convenient for clarity of presentation to place the system in the northern hemisphere with $f > 0$ and have negative surface stress ($\tau^{sy} < 0$) imply upwelling favorable conditions, though the derivation for $f < 0$ is straightforward and the discussion is general. For budgeting purposes, the model domain is divided into surface and bottom mixed layers, an interior, and the inner shelf where boundary layers converge. Bottom boundary layer (U^b) and surface mixed layer (U^s) transports are assumed equal to their Ekman transports, and the overall interior transport (U^i) is defined such that no net cross-shelf transport occurs for any x: $U^i = -(U^s + U^b)$. In the usual configuration of upwelling favorable wind stress considered here, U^s is negative, whereas U^b and U^i are positive.

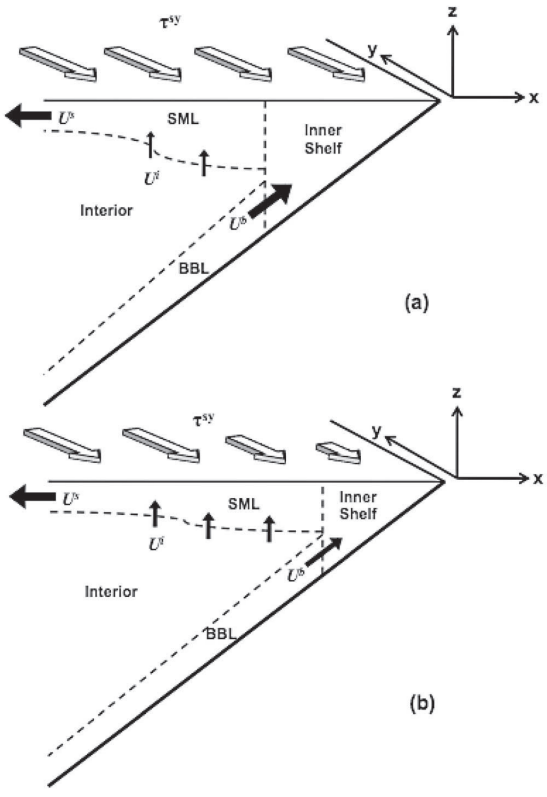

Figure 1. Schematic of model configuration and transport budget for (a) uniform winds and (b) a nearshore wind stress reduction (positive curl). The domain is divided into four regions: the surface mixed layer (SML), bottom boundary layer (BBL), interior, and inner shelf. Black arrows indicate BBL (U^b), interior (U^i), and surface (U^s) components of upwelling transport. The nearshore wind stress reduction produces a smaller inner shelf and shifts upwelling transport from the BBL to the interior. Transport far offshore in the SML is the same in both cases.

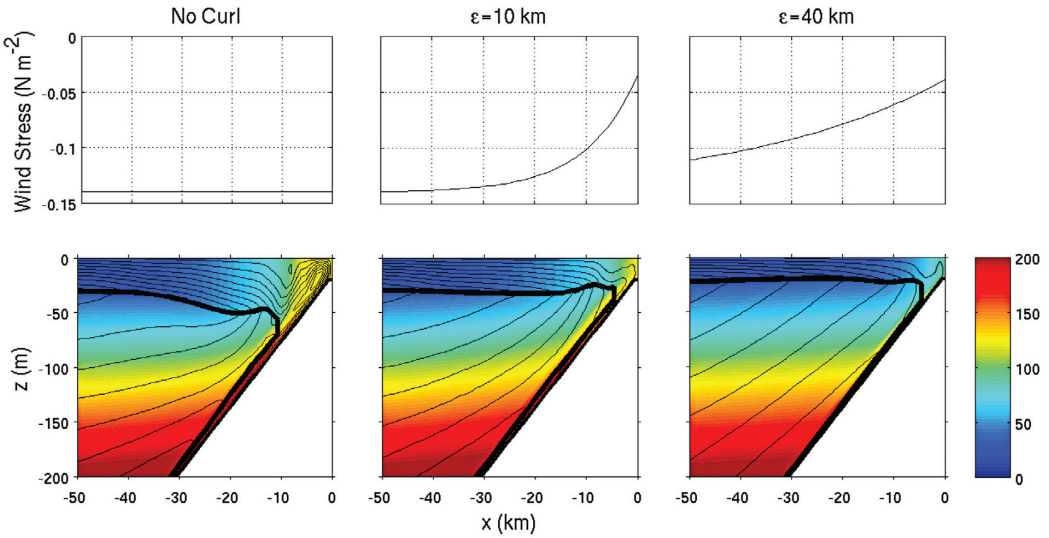

Figure 2. Upwelling response after 10 days is depicted under 3 wind patterns, for model simulations with $\alpha = 0.006$ and $N = 0.012\ s^{-1}$ (from left to right, runs 5, 14, and 32 in Table 1). (top) Cross-shelf structure of equator-ward wind stress; (bottom) streamlines (thin black lines) overlaid on "source depth tracer" concentration (color). The surface mixed layer, bottom boundary layer, and offshore extent of the inner shelf are marked by thick black lines.

[7] We represent the cross-shelf wind profile with an analytical function of the form

$$\tau^{xy} = \tau_c + (\tau_o - \tau_c)\left(1 - e^{x/\epsilon}\right), \tag{2}$$

where $\tau_c = -0.04\ \mathrm{Nm}^{-2}$ is the coastal wind stress, $\tau_o = -0.14\ \mathrm{Nm}^{-2}$ is the offshore value, and ϵ is the cross-shelf e-folding distance for wind stress. Model wind profiles are shown in Figure 2. In addition to curl-free runs ($\epsilon = 0$ km) we perform runs with $\epsilon = 10$, 20, and 40 km, where 90% of the curl is contained within 13, 46, and 92 km of the coast, respectively. These profiles are somewhat arbitrary, but their scales reasonably represent differences between wind products (e.g., QuikSCAT and RSM [*Song et al.*, 2011]) and between different resolutions of the same wind product (e.g., COAMPS at 3, 9, and 27 km [*Capet et al.*, 2004]).

[8] The efficacy of upwelling for bringing deep water to the surface is measured by the source depth of upwelled waters. In past modeling studies, source water has been studied by tracking floats released at various depths [*Capet et al.*, 2004] or running passive tracers from the surface mixed layer (SML) backward in time with an adjoint model [*Chhak and Di Lorenzo*, 2007; *Song et al.*, 2011]. Here, we use a passive tracer in the forward model to answer the question: at any given time, what is the origin depth of water entering the SML from below? This calculation is accomplished as described in *Jacox and Edwards* [2011], by initializing the model with a "source depth tracer" that increases linearly with depth (see Figure 2). Flux of this tracer into the SML divided by volume transport into the SML gives a characteristic source tracer concentration, which is mapped directly to source depth. Though not all upwelling originates from this particular depth, it is a useful integrated measure for characterizing source waters.

3. Theory

[9] We investigate here the relative partitioning of total transport between the BBL and the interior, as this partitioning directly impacts the origin of flux into the SML. Because U^s, U^b, and U^i all vary with cross-shelf position, it is useful to define $U_i^b = U^b(x_i)$ and $U_o^s = U^s(x_o)$, where x_i is the position of the inner shelf boundary and x_o represents a position sufficiently far offshore that surface wind stress is approximately its asymptotic value. Further, we define $\mathcal{R}_u = \left|U_i^b / U_o^s\right|$ as the metric that captures the partitioning of BBL transport of interest. $\mathcal{R}_u$ represents the fraction of total upwelled transport deriving from the BBL (entering the SML through the inner shelf and not through the interior). By definition $1 - \mathcal{R}_u$ represents the remaining fraction, which derives from the ocean interior and enters the SML broadly over the region $x_o < x < x_i$ (Figure 1).

[10] *Lentz and Chapman* [2004, hereinafter LC04] developed a simple steady state upwelling theory and focused on the importance of cross-shelf momentum flux divergence, a commonly overlooked component of the vertically integrated alongshore momentum balance. In the eastern boundary upwelling configuration, alongshore velocity is assumed to be equatorward and to decay with depth. The alongshore momentum transported offshore in the SML is therefore greater than that transported onshore below the SML, resulting in a net offshore momentum flux (illustrated in Figure 2 of LC04). Since momentum flux across the coastal boundary is zero, there must also be a nonzero

divergence of cross-shelf momentum flux. LC04 showed the importance of this term in determining cross-shelf flow structure for spatially uniform winds in the absence of an alongshore pressure gradient. At high Burger numbers, cross-shelf momentum flux divergence balances surface stress, and onshore flow is relatively high in the water column. At low Burger numbers, surface wind stress is balanced primarily by bottom stress and onshore flow is concentrated in the BBL. Here, we repeat the LC04 derivation, with modifications where necessary to include cross-shelf variation in surface and bottom stresses. We first briefly present the calculations leading to equation (7), which are identical to those of LC04 except for a change of coordinate system. Beyond equation (7), the additional calculations and assumptions required of our theoretical extension are described.

[11] We assume geostrophic balance between the cross-shelf pressure gradient and the Coriolis force associated with alongshelf flow, and thermal wind balance between the cross-shelf density gradient and vertical shear in the alongshelf flow. Both of these assumptions are observationally supported, as outlined in LC04. Integration of the thermal wind balance from the surface to depth z, assuming $\partial\rho/\partial x$ is vertically uniform, yields

$$v(z) \approx v^s + \frac{g}{f\rho_0}\frac{\partial \rho}{\partial x} z, \tag{3}$$

where v^s is alongshelf surface velocity.

[12] As described in section 2, cross-shelf transport is divided into surface- and bottom-stress driven Ekman layers, and an interior component. In the 2D configuration, vertically integrated cross-shelf transport is zero and the vertical structure of cross-shelf velocity is described by

$$u^s = \frac{\tau^{sy}}{\rho_o f \delta^s}, \qquad -\delta^s < z < 0, \tag{4}$$

$$u^i = -\frac{\left(\tau^{sy} - \tau^{by}\right)}{\rho_o f h}, \qquad -h < z < 0, \tag{5}$$

$$u^b = -\frac{\tau^{by}}{\rho_o f \delta^b}, \qquad -h < z < -h + \delta^b, \tag{6}$$

where each component of cross-shelf velocity is assumed to be vertically uniform (LC04) and δ^s and δ^b are surface and bottom boundary layer thicknesses, respectively. Using $v(z)$ from equation (3) and $u(z)$ from equations (4)–(6), we vertically integrate the product to estimate cross-shelf momentum flux:

$$\int_{-h}^{0} uv\, dz \approx \frac{g}{2\rho_0 f}\frac{\partial \rho}{\partial x}\left[\frac{\tau^{sy}}{\rho_0 f}\left(\delta^s - h\right) + \frac{\tau^{by}}{\rho_0 f}\left(\delta^b - h\right)\right], \tag{7}$$

where τ^{sy} and τ^{by} are surface and bottom stresses, respectively, and h is bottom depth. From equation (7), LC04 quantify cross-shelf momentum flux divergence assuming no cross-shelf variations in δ^s, δ^b, τ^{sy}, τ^{by}, or $\partial\rho/\partial x$. Here, we rework their theory allowing the stresses to be functions of the cross-shelf coordinate, x. Note that while LC04 initially developed the theory for application farther offshore, it predicts modeled BBL transport quite well at the inner shelf boundary, though $\mathcal{R}_u$ is underestimated at higher Burger numbers ($S > 1$). Examination of momentum budgets in our model runs shows that the assumption of geostrophic balance for cross-shelf momentum is still reasonable near the inner shelf boundary (defined in practice here as the location where SML and BBL are separated by <10 m). Also, for simplicity we retain the assumption that δ^s and δ^b are independent of x, though this is clearly an oversimplification (see Figure 2, for example). However, numerical model results show that $\partial\delta^b/\partial x$ and $\partial\delta^s/\partial x$ are generally much smaller than $\partial h/\partial x$, making the omission of those terms reasonable. Following the derivation of LC04, which assumes that the isopycnal slope is proportional to water depth divided by the baroclinic deformation radius,

$$\frac{\partial \rho/\partial x}{\partial \rho/\partial z} \approx \pm a\frac{h}{Nh/f} = \pm a\frac{f}{N}, \tag{8}$$

we find

$$\frac{\partial}{\partial x}\int_{-h}^{0} uv\, dz \approx -b\frac{|\tau^{sy}|}{\rho_0}\frac{S}{2}\left(1 + \frac{\tau^{by}}{\tau^{sy}}\right) \pm b\frac{x}{\rho_0}\frac{S}{2}\left(\gamma^s\frac{\partial \tau^{sy}}{\partial x} + \gamma^b\frac{\partial \tau^{by}}{\partial x}\right), \tag{9}$$

where the plus and minus signs correspond to $\tau^{sy} < 0$ (upwelling for $f > 0$) and $\tau^{sy} > 0$ (downwelling for $f > 0$) conditions, respectively. Here, the proportionality constant a is replaced by b, which also accounts for differences in cross-shelf and alongshelf velocity profiles from their assumed vertical structure (LC04), and γ^s and γ^b represent the fraction of the water column not in the SML and BBL, respectively:

$$\gamma^s = \frac{h - \delta^s}{h} \qquad \text{and} \qquad \gamma^b = \frac{h - \delta^b}{h}. \tag{10}$$

Typically $\gamma^s \sim 0.5$ at the inner shelf boundary and approaches 1.0 offshore, even for constant boundary layer thickness δ^s. The analogous BBL term scales similarly. In the curl free case, equation (9) reduces to that derived by LC04; the second term is an adjustment due to surface and bottom stress curls. Under steady state conditions and assuming no alongshore pressure gradient, the vertically integrated alongshore momentum equation can be written,

$$\frac{\partial}{\partial x}\int_{-h}^{0} uv\, dz = \frac{\tau^{sy}}{\rho_0} - \frac{\tau^{by}}{\rho_0}, \tag{11}$$

into which equation (9) can be substituted. Under upwelling conditions ($\tau^{sy} < 0$) of central interest to this study, the bottom stress is then expressed

$$\tau^{by} = \tau^{sy}\frac{1 - bS/2}{1 + bS/2} - \frac{bS/2}{1 + bS/2}\left(\gamma^s x\frac{\partial \tau^{sy}}{\partial x} + \gamma^b x\frac{\partial \tau^{by}}{\partial x}\right). \tag{12}$$

Again, the first term on the right is equal to that derived by LC04, though τ^{sy} is uniform in their theory whereas here it is a function of x. The second term represents an adjustment

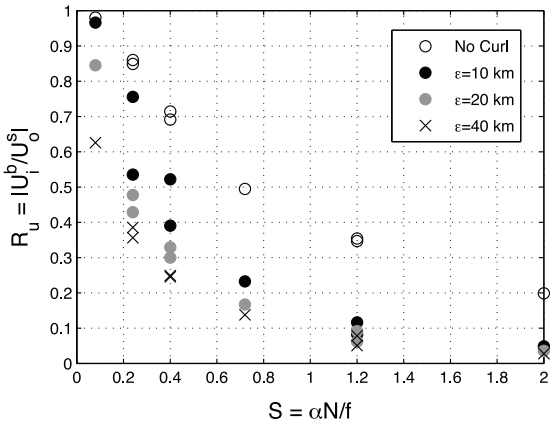

Figure 3. The relative contribution of bottom boundary layer transport to total upwelling transport after 10 days is shown as a function of Burger number. Markers indicate model results from four different surface forcings; the curl-free case and positive curl over three spatial scales.

due to local curl of surface and bottom stresses. For $f > 0$ and $\tau^{sy} < 0$, upwelling favorable conditions yield a negative bottom stress according to the first term. Positive wind and bottom stress curls result in a positive adjustment to this value according to the second term, because $x < 0$ within the domain. This reduction in bottom stress amplitude by the sum of stress curls indicates also an increase in the magnitude in the cross-shelf momentum flux divergence consistent with equation (11).

[13] Surface and bottom volume fluxes are given by Ekman transports associated with surface and bottom stresses, respectively. Far from shore, offshore surface transport in the curl case equals transport in the curl-free case,

$$U_o^s\big|_c = U_o^s\big|_{nc} = \frac{\tau_o^{sy}}{\rho_0 f} \qquad U_i^b = -\frac{\tau_i^{by}}{\rho_0 f}, \tag{13}$$

where subscripts c and nc indicate curl and no-curl cases, respectively, and subscripts o and i denote calculations at the offshore coordinate x_o and the inner shelf boundary x_i, respectively. From equations (12) and (13), the net change in relative transport $\mathcal{R}_u$ from the curl-free to the curl case is obtained:

$$\Delta\mathcal{R}_u = \mathcal{R}_{u,c} - \mathcal{R}_{u,nc} = -\mathcal{R}_{u,nc}\left(1 - \frac{\tau_{c,i}^{sy}}{\tau_{nc}^{sy}}\right) - \frac{x_i}{\tau_{nc}^{sy}} \frac{bS/2}{1 + bS/2}\left(\gamma^s \frac{\partial \tau_c^{sy}}{\partial x} + \gamma^b \frac{\partial \tau_c^{by}}{\partial x}\right)_i. \tag{14}$$

The terms on the right hand side of equation (14) describe two theoretical means by which a nearshore drop-off in alongshore wind stress alters $\mathcal{R}_u$ relative to the curl-free case. The first is a reduction in BBL transport associated with reduced surface Ekman transport at the inner shelf boundary. In the curl case, surface wind stress at the inner shelf boundary is less than that in the curl-free case. BBL transport at the inner shelf boundary is therefore reduced, proportionate to the surface wind stress reduction at that location. The first term on the right hand side of equation (14) is less than zero, indicating that a smaller fraction of total upwelled water derives from the bottom boundary layer at the inner shelf boundary, and a greater fraction arrives from the interior. This term is greatest when wind stress at the inner shelf boundary is small compared to that offshore. The second term represents a curl-driven increase in the cross-shelf momentum flux divergence, and is greater for strong curl and high Burger numbers. Since $x < 0$ in the domain and $\tau_{nc}^{sy} < 0$ for upwelling, positive stress curls result in a further reduction in relative BBL transport.

[14] A major limitation of this theory, discussed further by LC04, is that there is no interaction between cross-shelf circulation and an evolving density field. Rather, the cross-shelf scale of sloping isopycnals is assumed to be the baroclinic deformation radius, and isopycnal slope is therefore proportional to f/N. It is valuable, therefore, to compare the theory to a numerical model with time-dependent dynamics. We present this comparison in the following section.

4. Results

[15] Variable structure in cross-shelf flow imparted by different wind patterns is clearly illustrated in the streamlines of Figure 2. Vertical transport in the curl-free case is strong, concentrated close to the coast, and largely contained in the BBL. Wind stress reduction nearshore results in horizontally distributed upwelling under the region of positive curl, and weaker vertical transport. These effects become more prominent as the horizontal scale of curl increases. As predicted by the theory in section 3, there is a shift in transport from the BBL to the interior associated with weakened winds nearshore, and several reasons for this are evident in Figure 2. The first is a reduction in surface Ekman transport (and associated BBL transport) in the region of curl, as described by equation (14). At a given offshore position x, surface Ekman transport is reduced as the cross-shelf scale of curl increases, and $U^b(x)$ drops accordingly. Furthermore, weaker nearshore wind stress reduces the offshore extent of the inner shelf, placing its boundary (where U_i^b is defined) at a position closer to shore and under even lower wind stress. Second, the structure of the BBL flow itself is visibly altered by wind stress curl. Although BBL volume transport is theoretically independent of x in the curl-free case, model simulations show BBL transport increasing monotonically with decreasing distance from shore as the BBL entrains water from the interior. While a similar entrainment occurs offshore under cyclonic wind stress curl forcing, streamlines exit the BBL just offshore of the inner shelf, and this fluid enters the SML from the interior.

[16] Surface and bottom boundary layer transports are calculated from the model as vertical integrals of zonal velocity between relevant limits. This practice technically includes non-Ekman (i.e., interior) transport that occurs within the boundary layers, but this contribution is generally small, and we neglect the difference between this value and the pure Ekman transport used in the theory. In general, $\mathcal{R}_u$ decreases at higher Burger numbers, and with increased scale of wind stress curl (Figure 3). However, the point at which a change in curl scale effects greatest change in $\mathcal{R}_u$ is dependent on slope and stratification. In the most weakly

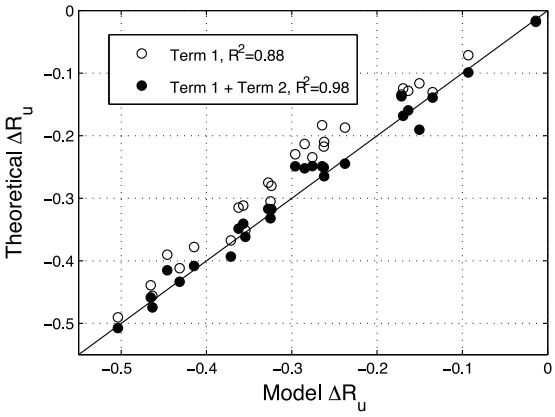

Figure 4. Change in $\mathcal{R}_u$ relative to the curl-free case is depicted for all 27 curl cases (runs 10–36 in Table 1), as measured in model simulations and predicted by theory. Terms 1 and 2 refer to the right-hand side of equation (14), with $b = 1$. Term 1 (Ekman transport adjustment) accounts for most of the shift in $\mathcal{R}_u$, and term 2 (cross-shelf momentum flux adjustment) improves model-theory agreement. Perfect agreement is indicated by solid line.

stratified, weakly sloping ($S = 0.08$) case, $\mathcal{R}_u$ changes little between the curl-free and $\epsilon = 10$ km cases, but substantially from $\epsilon = 10$ km to $\epsilon = 20$ km and from $\epsilon = 20$ km to $\epsilon = 40$ km. At high Burger numbers, effectively all the change occurs between the curl-free and $\epsilon = 10$ km cases, with little additional impact as ϵ is increased further. The key relationship here is between the cross-shelf scale of the curl and the position of the inner shelf boundary, where BBL transport enters the SML. In general, the inner shelf extends farther offshore with weaker stratification and reduced slope [*Jacox and Edwards*, 2011]. At our low Burger number extreme ($S = 0.08$), the inner shelf extends far (30–40 km) offshore and strong curl ($\epsilon = 10$ km) contained within that distance is effectively the same as no wind stress reduction in terms of transport partitioning. For $S = 2$, the inner shelf is confined extremely close to shore ($\lesssim$2 km), and curl over any of the three scales influences $\mathcal{R}_u$ similarly. In terms of fractional change in BBL transport, the greatest decrease is at high Burger numbers. While ~25% of upwelling transport for $S = 2$ in the curl-free case is BBL derived, its contribution drops to ~3% in the curl cases. As the BBL transport contribution to upwelling of deep waters is disproportionately high [*Jacox and Edwards*, 2011], this reduction in $|U_i^b|$ greatly reduces overall source depth.

[17] Figure 4 depicts the theoretical adjustment to BBL transport (equation (14)) as compared to numerical model results. Changes in Ekman transport at the inner shelf boundary (Term 1 in Figure 4) account for most of the transport partitioning adjustment, while the curl-driven change in cross-shelf momentum flux divergence (Term 2 in Figure 4) produces a smaller effect. Estimating the reduction in $\mathcal{R}_u$ by only the former process produces good model-theory agreement ($R^2 = 0.88$), which is further improved by including the latter effect ($R^2 = 0.98$). Contributions to Term 2 from wind stress curl and bottom stress curl are typically of similar scale. We note that bottom stress curl exists even in the curl-free wind stress case considered by LC04; however, its magnitude, and therefore its contribution to BBL transport, is generally small except at high Burger number.

[18] Though the theory presented here was developed for steady state, acceleration in the numerical model is significant even after 10 days, especially at high Burger numbers and farther offshore. Similarly, LC04 showed that at higher Burger numbers temporal acceleration contributes materially to the vertically integrated momentum budget,

$$\frac{\tau^{sy} - \tau^{by}}{\rho_0} = \frac{\partial}{\partial t}\int_{-h}^{0} v\,dz + \frac{\partial}{\partial x}\int_{-h}^{0} uv\,dz. \tag{15}$$

Their steady theory works well because, as they discuss, their estimate of the cross-shelf momentum flux divergence (with $b = 1$) overestimates that obtained numerically and partially accounts for temporal acceleration. In our numerical results we find that terms in the alongshelf momentum balance, when normalized by surface stress, are only slightly affected by wind stress curl. A small decrease in the amplitude of the bottom stress term is accompanied by modest adjustments of the integrals on the right hand side of equation (15). Therefore, changes to relative bottom stress are minor and are accurately predicted by equation (12).

[19] As stated previously, BBL transport draws from deeper than interior transport. It is not surprising therefore to see a general trend of increasing source depth with increasing $\mathcal{R}_u$ (Figure 5). Since $\mathcal{R}_u$ is dependent on Burger number (which includes shelf slope, stratification, and Coriolis frequency) as well as the scale of wind stress curl (Figure 3), all of these parameters also influence source depth. Increasing stratification or the scale of wind stress curl causes a decrease in $\mathcal{R}_u$ and, consequently, in upwelling source depth. However, the relationship between $\mathcal{R}_u$ and source depth is more complicated; for a given change in $\mathcal{R}_u$, the

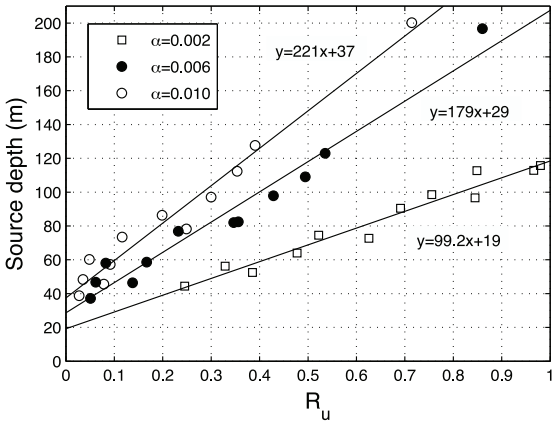

Figure 5. The relationship between $\mathcal{R}_u$ and mean upwelling source depth after 10 days is depicted for all 36 model runs. Model configurations with different shelf slope, α, are indicated by different marker types (each marker type includes 3 different stratifications and 4 different wind patterns), and linear fits are shown for each shelf slope.

change in source depth is greater with steeper shelf slope. For example, our results show that for $\Delta\mathcal{R}_u = 0.1$, source depth increases by 9.9, 17.9, and 22.1 m for α = 0.002, 0.006, and 0.010, respectively. As described in *Jacox and Edwards* [2011], water of a given depth is laterally closer to shore in steep slope cases, and reaches the inner shelf faster with the same horizontal velocity. As $\mathcal{R}_u$ decreases (high Burger number, weak nearshore winds), source depth decreases to a projected minimum of 20–40 m on day 10 in the case of no BBL transport. At the other extreme, where all transport derives from the BBL, source depths on day 10 reach 120–260 m, depending on shelf slope.

5. Discussion

[20] Through the suite of numerical model runs performed here, we investigated the effects of slope, stratification, and wind stress curl on upwelling source depth and partitioning of vertical transport. Ranges of slope and stratification were chosen to cover those seen in major global upwelling regions, and wind stress curl was varied over a range of scales that could be representative of spatial or temporal variability, different wind products, or different resolutions of the same wind product. We find that as the cross-shelf scale of curl increases, upwelling transport increasingly derives from the interior rather than the BBL, with the greatest fractional reduction in $\mathcal{R}_u$ at high Burger numbers. Mean upwelling source depth increases linearly with $\mathcal{R}_u$ for a given shelf slope, and increases more rapidly with $\mathcal{R}_u$ over steeper slopes.

[21] We find that evaluating the impact of nearshore curl on upwelling source depth requires consideration of not just the scale of the curl, but also the width of the inner shelf. Weak stratification and gradual shelf slope produce a wider inner shelf than strong stratification and steep slope, and consequently different scales at which changes in curl are most important. Reduction of $\mathcal{R}_u$ due to a nearshore wind stress drop-off is minimal if the drop-off occurs primarily over the inner shelf, and substantial if it occurs offshore of the inner shelf boundary. A third cross-shelf scale, the one over which coastal upwelling occurs, may be important for distinguishing the coastal and curl-driven upwelling components. Classifying coastal divergence as only the transport driven by the coastal wind stress would underestimate its contribution; upwelling associated with the mean wind stress over the width of the coastal upwelling zone may be a more accurate measure. However, we do not attempt to separate these components while exploring the impacts of nearshore curl on upwelling dynamics, and in fact they are not independent. In the nearshore curl region, Ekman pumping raises isopycnals in the interior of the water column, altering source waters for coastal upwelling and likely increasing resultant nutrient fluxes.

[22] By definition, the separation of U^b and U^i distinguishes flux to the inner shelf from that supplying the mid and outer shelf, offshore of the upwelling front. These regions are likely to support different biological communities, with larger plankton sustained by strong upwelling and substantial nutrient flux nearshore and smaller plankton supported by weaker offshore upwelling [*Rykaczewski and Checkley*, 2008]. Our results therefore suggest that the retentive inner shelf region, supporting larger plankton, should be wide and productive in the presence of weak stratification and wind stress that remains strong close to shore. Strong stratification and substantial nearshore wind stress reduction, on the other hand, should support smaller plankton in a large region of cyclonic wind stress curl. The effect of shelf slope is less clear in this regard due to a tradeoff between conditions favorable to growth of large plankton. Weaker slopes promote BBL transport and produce a wider inner shelf, but steeper slopes allow upwelling of deeper water, presumably richer in nutrients.

[23] Questions regarding the relative importance of curl-driven and coastal upwelling have persisted in the literature for at least a decade, generally in the form; (1) How does the reduction in nearshore wind stress (i.e., cyclonic curl) affect upwelling transport? and (2) How do changes in this structure alter the source waters for upwelling? However, modeling studies designed to address these questions have been performed in different regions, with different wind products, and using different metrics to quantify upwelling. For example, *Capet et al.* [2004] investigated a CCS model, used QuikSCAT winds for the "weak curl" case, released floats to quantify upwelling, and found that cyclonic curl does not compensate for reduced coastal wind stress. *Albert et al.* [2010] investigated the Peru current system, used QuikSCAT winds for the "strong curl" case, evaluated the efficacy of upwelling with nutrient and chlorophyll diagnostics from a biogeochemical model, and found decreased coastal divergence to be overcompensated by curl-driven upwelling. Though these studies and others seem to offer contrary conclusions on the relative importance of coastal and curl-driven upwelling, we believe their findings, in light of the present study, can be reconciled when differences in methods and upwelling metrics are considered. In general: (1) total upwelling transport is determined primarily by wind stress far offshore ($|x| \gg \epsilon$) rather than the curl structure, though the relative contribution of coastal divergence decreases as nearshore wind stress decreases, and (2) upwelling source depth is altered by the cross-shelf wind profile, and increases as high offshore winds extend closer to the coast. However, there are complex interactions between wind stress, stratification, and topography that exert important influence on upwelling dynamics (Figure 3) and make direct comparison between studies difficult. In addition, important dynamics not captured in the present study should be considered, including (1) though nutrients in the ocean typically increase with depth, nutrient fluxes are not necessarily coupled to source depth in EBCs, where decreased source depth may accompany a curl-driven shoaling of the nutrient-rich poleward undercurrent, (2) *Fennel and Lass* [2007] argued that decreased Ekman transport can actually be overcompensated by Ekman pumping due to inhibition of coastal upwelling by coastally trapped waves, and (3) the ability of an alongshore pressure gradient to modify upwelling dynamics has been well documented, and is not included in our 2D model.

[24] **Acknowledgments.** We gratefully acknowledge funding from the Gordon and Betty Moore Foundation and National Science Foundation grant OCE0726858. Comments from two anonymous reviewers greatly improved the manuscript. We also thank Jenny Quay for many helpful discussions.

References

Albert, A., V. Echevin, M. Lévy, and O. Aumont (2010), Impact of nearshore wind stress curl on coastal circulation and primary productivity in the Peru upwelling system, *J. Geophys. Res.*, *115*, C12033, doi:10.1029/2010JC006569.

Capet, X. J., P. Marchesiello, and J. C. McWilliams (2004), Upwelling response to coastal wind profiles, *Geophys. Res. Lett.*, *31*, L13311, doi:10.1029/2004GL020123.

Chhak, K., and E. Di Lorenzo (2007), Decadal variations in the California Current upwelling cells, *Geophys. Res. Lett.*, *34*, L14604, doi:10.1029/2007GL030203.

Croquette, M., G. Eldin, C. Grados, and M. Tamayo (2007), On differences in satellite wind products and their effects in estimating coastal upwelling processes in the south-east Pacific, *Geophys. Res. Lett.*, *34*, L11608, doi:10.1029/2006GL027538.

Dever, E. P., C. E. Dorman, and J. L. Largier (2006), Surface boundary-layer variability off Northern California, USA, during upwelling, *Deep Sea Res., Part II*, *53*, 2887–2905.

Enriquez, A. G., and C. Friehe (1995), Effects of wind stress and wind stress curl variability on coastal upwelling, *J. Phys. Oceanogr.*, *25*, 1651–1671.

Fennel, W., and H. U. Lass (2007), On the impact of wind curls on coastal currents, *J. Mar. Syst.*, *68*, 128–142.

Jacox, M. G., and C. A. Edwards (2011), Effects of stratification and shelf slope on nutrient supply in coastal upwelling regions, *J. Geophys. Res.*, *116*, C03019, doi:10.1029/2010JC006547.

Koracin, D., C. E. Dorman, and E. P. Dever (2004), Coastal perturbations of marine layer winds, wind stress, and wind stress curl along California and Baja California in June 1999, *J. Phys. Oceanogr.*, *34*, 1152–1173.

Lentz, S. J., and D. C. Chapman (2004), The importance of non-linear cross-shelf momentum flux during wind-driven coastal upwelling, *J. Phys. Oceanogr.*, *34*, 2444–2457.

Messié, M., J. Ledesma, D. D. Kolber, R. P. Michisaki, D. G. Foley, and F. P. Chavez (2009), Potential new production estimates in four eastern boundary upwelling ecosystems, *Prog. Oceanogr.*, *83*, 151–158, doi:10.1016/j.pocean.2009.07.018.

Pickett, M. H., and J. D. Paduan (2003), Ekman transport and pumping in the California Current based on the U.S. Navy's high-resolution atmospheric model (COAMPS), *J. Geophys. Res.*, *108*(C10), 3327, doi:10.1029/2003JC001902.

Rykaczewski, R. R., and D. M. Checkley (2008), Influence of ocean winds on the pelagic ecosystem in upwelling regions, *Proc. Natl. Acad. Sci.*, *105*, 1965–1970.

Shchepetkin, A. F., and J. C. McWilliams (2005), The Regional Ocean Modeling System: A split-explicit, free-surface, topography following coordinates ocean model, *Ocean Modell.*, *9*, 347–404.

Song, H., A. J. Miller, B. D. Cornuelle, and E. Di Lorenzo (2011), Changes in upwelling and its water sources in the California Current System driven by different wind forcing, *Dyn. Atmos. Oceans*, *52*, 170–191.

CHAPTER THREE

Potential Improvements to Remote Primary Productivity Estimation in the Southern California Current System

Abstract

A 26-year record of depth integrated primary productivity (PP) in the Southern California Current System (SCCS) is analyzed with the goal of improving satellite net primary productivity (PP) estimates. The ratio of integrated primary productivity to surface chlorophyll correlates strongly to surface chlorophyll concentration (chl_0). However, chl_0 does not correlate to chlorophyll-specific productivity, indicating that it is a proxy for vertical phytoplankton distribution rather than phytoplankton physiology. Modest improvements in PP model performance are achieved by tuning existing algorithms for the SCCS, particularly by parameterizing photosynthetic efficiency in the Vertically Generalized Production Model as a function of chl_0 and distance from shore. Much larger improvements are enabled by improving accuracy of subsurface chlorophyll and light profiles. In a simple vertically resolved production model, substitution of *in situ* surface data for remote sensing estimates offers only marginal improvements in model r^2 (from 0.54 to 0.56) and total $\log_{10}$ root mean squared difference (from .22 to .21), while inclusion of *in situ* chlorophyll and light profiles improves these metrics to 0.77 and 0.15, respectively. Autonomous underwater gliders, capable of measuring subsurface properties on long-term, long-range deployments, significantly improve PP model fidelity in the SCCS.

We suggest their use (and that of other autonomous profilers) in conjunction with satellites as a way forward for large-scale improvements in PP estimation.

Introduction

The satellite ocean color era began with the launch of the Coastal Zone Color Scanner (CZCS) in 1978. Several years later, with scientists using ocean color to estimate surface chlorophyll (chl_0), Eppley et al. (1985) examined relationships between chl_0 and euphotic zone integrated primary production (PP) in anticipation of attempts to quantity PP from satellites. In that paper they described variability in the ratio $F=PP/chl_0$, and suggested the simplest of satellite primary productivity algorithms (PPAs), where F is assumed constant and PP (gC m^{-2} d^{-1}) is the square root of chl_0 (mg m^{-3}). That model, which we refer to as the Eppley Square Root model (ESQRT), represents a baseline of both complexity and skill for PPAs.

In the subsequent decades, many PP models have been developed (see Saba et al., 2011 for 21 examples) in an effort to improve satellite productivity estimates. In addition to satellite estimates of surface chlorophyll (chl_0), they typically rely on satellite-derivable physical quantities such as sea surface temperature (SST) and photosynthetically available radiation (PAR), either directly or through the inclusion of physiological variables (e.g. quantum yield, carbon fixation rate) that are estimated from satellite-derived properties. A series of primary productivity algorithm round-robin (PPARR) comparisons (Campbell et al., 2002; Carr et al., 2006; Friedrichs et al., 2009; Saba et al., 2011) evaluates satellite algorithms of wide-ranging complexity,

from the ESQRT baseline to fully depth- and wavelength-resolved algorithms, and has produced several key findings: (i) model performance does not improve with model complexity, (ii) no particular model consistently outperforms the others, (iii) chl_0 captures primary productivity variability than any other parameter, (iv) models typically underestimate observed PP variability and may fail to capture broad scale regime shifts, and (v) average model skill is significantly lower in coastal waters than pelagic waters, partly due to increased uncertainty in satellite chlorophyll estimates, and partly to limitations of the algorithms.

Though PPAs have been evaluated in some coastal systems (e.g. Saba et al., 2011), none of the PPARR experiments include data from the California Current System (CCS), nor do they include other major upwelling ecosystems (Humboldt, Canary, Benguela). Kahru et al. (2009) conducted a scaled-down PPARR-like comparison, evaluating five PPAs in the SCCS, and found little difference between them. All were biased toward high productivity, and none captured more than 66% of the observed data variance.

In this paper we explore PP in the southern CCS (SCCS) with the goal of informing improved satellite PPAs. First, we update the Eppley et al. (1985) analysis of *in situ* productivity data in the SCCS. Their study was based on ~270 stations occupied from 1974-1983 within a region bounded approximately by Los Angeles and San Diego to the north and south, respectively, and up to 100 km offshore. We use over 25 years of PP data from the California Cooperative Oceanic Fisheries Investigations (CalCOFI), including over 1500 primary productivity casts from ~100

quarterly cruises since 1985, with spatial coverage throughout the southern California Bight and up to 600 km offshore. Next, we evaluate several existing PPAs for their performance against CalCOFI data and explore possibilities for improving their performance in the CCS. Finally, we provide suggestions for further improving PP estimates with the aid of autonomous subsurface platforms.

Methods

In situ Data

Since 1984, on-deck ^{14}C incubations have been performed on quarterly cruises as part of the CalCOFI program. Reported half-day (local noon to sunset) values, integrated over the euphotic depth, are multiplied by 1.8 to obtain equivalent 24 hr productivity (Eppley, 1992). Station locations for the dataset used in this paper are shown in Figure 1, totaling 1544 PP casts from 1985-2011. Additional parameters recorded on CalCOFI cruises and utilized here include SST, chlorophyll, light attenuation at depth, and distance from shore.

Satellite Data

Where available, satellite estimates of chl_0, SST, and PAR have been obtained for comparison with CalCOFI data. Chl_0 was derived by applying a recently developed empirical algorithm (Kahru et al., 2012), based on over 10,000 in situ measurements from the California Current, to SeaWiFS Level-3 remote sensing radiance. This algorithm produces values very similar to those from the current

standard OC4v6 algorithm for *in situ* $chl_0 < 1$ mg m^{-3} but significantly higher values for *in situ* $chl_0 > 1$ mg m^{-3}. PAR (mol quanta m^{-2} d^{-1}) was obtained from the standard SeaWiFS product (Frouin et al., 2003) for 1997-1999 and merged from multiple sensors (SeaWiFS, MODIS-Terra, MODIS-Aqua) for 2000-2010. For SST, we used the daily AVHRR Pathfinder 5 dataset described by Casey et al. (2010), and interpolated when measured SST values were missing. All three datasets were daily composites with 9 km global mapping. For each CalCOFI station, match-ups were sought for the nearest satellite pixel on the same day. If those data were not available, the search was continued forward and backward in time until the nearest valid dataset was found. Satellite match-ups were available for 723 CalCOFI PP stations.

Glider Data

Glider data was provided by D. Rudnick and comes from Spray gliders deployed by Scripps Institute of Oceanography. All available data was filtered to find vertical profiles in proximity to CalCOFI PP stations, subject to a range of spatial and temporal constraints. For each station, a mean fluorescence profile was obtained by averaging all glider profiles within the match-up criteria. Fluorescence was converted to chlorophyll according to Lavigne et al. (2012) assuming euphotic zone depth exceeds mixed layer depth, the predominant condition off the California coast (Frolov et al., 2012). The Lavigne et al. (2012) algorithm uses measured surface chlorophyll to calibrate the fluorescence profile, reducing uncertainty due to detector variability, drift on long deployments, and fluctuations in the relationship between fluorescence

and chlorophyll. Nonetheless, we assume that there is unquantified variability in the fluorescence data due to these factors.

Satellite Primary Productivity Algorithms

It is not our intention to replicate the PPARR comparisons specifically for the CCS. Instead, we evaluate several well-known models that we consider representative of the larger set of available PPAs in both methodology and performance. Each of the models tested includes physiological variables that may be tuned for the CCS as a first step toward improving model-data agreement.

The model described by Marra et al. (2003) (MARRA) is depth-resolved, and uses inputs of chl_0, SST, and PAR. It is based on chlorophyll-specific absorption, which is parameterized by SST, and maximum quantum yield, which is assumed constant for a given region. The vertical chlorophyll profile is estimated from surface concentration and is used along with non-photosynthetic absorption coefficients to calculate light attenuation with depth.

The widely used Vertically Generalized Production Model (VGPM) of Behrenfeld and Falkowski (1997) requires the same three inputs as MARRA, and uses latitude and time of year to calculate day length. It relates productivity to the optimal chlorophyll-specific carbon production rate (P^B_{OPT}), which is estimated by a seventh-order polynomial fit to SST. A number of VGPM variants have been proposed with alternate methods of estimating P^B_{OPT}, and we evaluate one proposed by Kameda and Ishizaka (2005) (VGPM-KI), which assumes the chlorophyll

concentration is made up of a small, stable component and a large, fluctuating component.

Statistics

To quantify model performance, we present a suite of statistical measures that have been employed routinely in past PPA comparisons. They are the determination coefficient (r^2), total root mean square difference (RMSD), centered-pattern RMSD (RMSDcp), and bias. All statistics are calculated on log-transformed data, and the total RMSD summed over *n* data points is

$$RMSD = \left(\frac{1}{n} \sum_{i=1}^{n} \left[\log(PP_M(i)) - \log(PP_I(i)) \right]^2 \right)^{1/2} \quad (1)$$

where PP_M and PP_I denote modeled and *in situ* primary productivity (mg m^{-2} d^{-1}), respectively. RMSD is a measure of total model skill, and captures a model's ability to accurately represent both the mean and variability of *in situ* data. We therefore also divide RMSD into two components,

$$RMSD^2 = RMSDcp^2 + Bias^2 \quad (2)$$

where Bias and RMSDcp capture model-data differences in the mean and variability, respectively.

To avoid evaluating new PPAs against the data with which they were developed, we divide the SeaWiFS-CalCOFI match-ups into one period for model development (1997-2004, n=399) and one for model validation (2005-2010, n=324). Statistics for PPA comparisons are calculated on the latter.

Results

Properties of the CalCOFI Dataset

We begin with an examination of the full *in situ* primary productivity dataset. Data are available year-round, with 72-254 PP casts available per month (mean is 154), except for June and December which had five casts and none, respectively, during our 26-year analysis window. Mean monthly PP over the entire CalCOFI domain exhibits seasonal variability with lower values from late fall to early spring (PP = 450-600 mg m^{-2} d^{-1} from September to March), higher values in the spring and late summer (800-850 mg m^{-2} d^{-1} for April, July, and August), and maximum productivity in May (~1400 mg m^{-2} d^{-1}) and June (~1200 mg m^{-2} d^{-1}), during peak upwelling season.

As in Eppley et al. (1985), we examine properties of the ratio $F = PP/chl_0$, a parameter of particular interest for remote sensing applications. Correct representation of F is the necessary link between satellite estimates of chl_0 and accurate PP estimates from depth-integrated PPAs. The analogous ratio for surface primary productivity (pp_0), $F_0 = pp_0/chl_0$, is of particular interest for depth-resolved PPAs.

When viewed against environmental variables, qualitative differences between F and F_0 are readily apparent (Figure 2). F is negatively correlated with chl_0 and more weakly positively correlated with SST. In contrast, F_0 is uncorrelated to chl_0 and has only very weak temperature dependence. One explanation for this discrepancy is the relationship of surface chlorophyll to the vertical chlorophyll profile. Typically, low chl_0 is associated with a deep chlorophyll max while high chl_0 is characteristic of surface-intensified phytoplankton blooms. The former has significant productivity at depth, and F is high, while the opposite is true for the latter. This paradigm indicates that the decrease of F with increasing chl_0 is a proxy for changes in the vertical distribution of phytoplankton, not a physiological effect, and explains why a similar pattern is not seen in F_0. The same explanation can be invoked for the increasing trend of F toward higher temperatures, since cold, upwelled waters near shore in the CCS are associated with higher chl_0. It should be noted, however, that increased growth rates at higher temperatures are expected outside of upwelling systems as well (Eppley, 1972; Behrenfeld and Falkowski, 1997), and we do see weak temperature dependence in F_0.

Though noisy, opposite trends are visible in F and F_0 when viewed as functions of distance from shore. F is on average higher farther from shore, in line with a trend toward low chl_0 and deep chlorophyll maxima offshore. F_0 decreases as distance from shore increases, with the mean offshore value approximately half that near the coast. In contrast to the trend in F, this result is likely a physiological response driven by a combination of nutrient availability and phytoplankton

community composition. Seasonal variability is present in both F and F_0, though more strongly for F_0, with a minimum in winter, increase in the spring, and peak in late summer/fall. Attributing seasonality in these ratios to a specific cause is difficult, as time of year may be a proxy for day length, PAR, or community structure, specifically the relative abundance of diatoms and dinoflagellates.

Performance of Existing PPAs

Model statistics for common PPAs (MARRA, VGPM, VGPM-KI) are given in Table 2 (with *in situ* chl_0 and SST inputs) and Table 3 (using SeaWiFS data). Differences between Tables 2 and 3 can be attributed to inaccuracies in satellite chlorophyll estimates, as differences in model performance using *in situ* rather than remotely sensed SST are negligible. The models are less sensitive to SST than chl_0, and *in situ*-satellite correlations are better for SST than for chl_0 (r^2=0.86 and 0.55, respectively). SeaWiFS PAR is used in all cases, as surface PAR is not reliably available on CalCOFI cruises.

None of the three PPAs tested here is clearly superior to the others. All are biased high and capture just under 60% of the total $\log_{10}$ data variance. MARRA and VGPM-KI have comparable RMSD, though MARRA represents the mean slightly better and the variability slightly worse than VGPM-KI. VGPM is even more biased than the others but has the lowest RMSDcp and ties for the best r^2, making it the ideal candidate for a purely empirical adjustment of model output (Kahru et al., 2009).

VGPM-KI is most sensitive to inaccuracies in chl_0, incurring the most significantly reduced determination coefficient when satellite chl_0 is used in place of *in situ* data.

VGPM and MARRA exhibit seasonally-dependent performance when evaluated within winter (Dec-Feb), spring (Mar-May), summer (Jun-Aug), and fall (Sep-Oct) periods (Table 4). While both models are biased high year-round, they are more so in the winter/spring, and less in the summer/fall. Neither model appears to fully capture the seasonal variability in chlorophyll-specific phytoplankton growth evident in Figure 2. Consequently, model bias is highest when chlorophyll-specific productivity is relatively low. Coefficients of determination range widely among seasons, with values highest values in spring (~0.75) and lowest in fall (~0.47). However, RMSD and RMSDcp do not follow the same pattern, and r^2 values are likely high in the spring largely due to it being the season of greatest PP variance.

Empirical Adjustment of PPAs

The simplest method of improving an existing PPA is an empirical adjustment of the model output to match *in situ* data (Kahru et al., 2009). The adjustment has no ecological basis, but improves performance. A next step is to improve the model's parameterizations of physiological variables, for example the quantum yield and chlorophyll-specific absorption terms in MARRA or the optimal photosynthetic efficiency term (P^B_{OPT}) in VGPM. The latter has been done before, with the original 7^{th}-order fit to SST replaced by alternate functions of SST, chl_0, or a combination of

the two (Friedrichs et al., 2009). Here, we calculated the value of P^B_{OPT} that would give perfect model-data agreement for each data point

$$P^B_{OPT,CALC} = \frac{PP}{0.66125 \cdot \frac{PAR}{PAR + 4.1} \cdot z_{eu} \cdot chl_0 \cdot d_{irr}} \quad (3)$$

and identified correlations with environmental data. Euphotic zone depth (z_{eu}) is estimated from chl_0 (Morel and Berthon, 1989) and day length (d_{irr}) is a function of latitude and time of year (Forsythe et al., 1995). Variables considered for parameterization of $P^B_{OPT,CALC}$ were chl_0, SST, PAR, latitude, and distance from shore. As in Eppley et al. (1985), SST did not offer significant improvement of the parameterization. PAR is strongly correlated with the already included d_{irr}, and offered no additional gains. We also found no significant relationship between $P^B_{OPT,CALC}$ and latitude. A clear relationship with chl_0 does exist, as expected from the upper left panel of Figure 2, and we find that for a given chl_0, $P^B_{OPT,CALC}$ is higher closer to shore, likely due to increased nutrient availability and a different phytoplankton community composition. Figure 3 illustrates this relationship, the basis for a southern California-specific VGPM variant (VGPM-SC). All CalCOFI sites are divided into three regimes based on their distance from the coast – near shore (<50 km), transition (50-250 km), and offshore (>250 km). Within each region, $P^B_{OPT,CALC}$ for 1997-2004 was fit as a power law function of chl_0, and resultant model performance for 2005-2010 is presented in Tables 2 and 3. All statistics for the new

model are improved over the original VGPM and other models, with the reduction of bias being a substantial benefit. Though the parameterization of P^B_{OPT} in VGPM-SC was developed empirically, it has a sound ecological basis.

Vertically Resolved Production Model

Given the luxury of vertically resolved *in situ* primary productivity measurements from the CalCOFI dataset, model-data productivity comparisons are possible at discrete depths as well for the euphotic zone integrated value. We take advantage of that resource here to examine the potential for development of a vertically resolved production model for the SCCS (VRPM-SC). Again, we start with the depth-integrated VGPM, which performed well when initially developed in a vertically-resolved form (Behrenfeld and Falkowski, 1997). We discard factors related to vertical generalization of the productivity profile to obtain a simple expression for depth-dependent productivity (pp_z),

$$pp_z = P_z^B \cdot chl_z \cdot d_{irr} \quad (4)$$

where P^B_z and chl_z are photosynthetic efficiency and chlorophyll concentration, respectively, at depth z. PAR is assumed to be the next most important factor influencing depth-dependent productivity, as we expect photoinhibition at high light levels and light limitation at depth. Though PAR profiles are not consistently available for CalCOFI data, productivity measurements are accompanied by reported

light levels, expressed as a percentage of the surface value. To estimate the vertical PAR profile, CalCOFI *in situ* light percentages are multiplied by SeaWiFS surface PAR.

Figure 4 shows the dependence of P^B_z on PAR at discrete depths (PAR_z), most significantly the light limitation below ~10 mol quanta m^{-2} d^{-1}. At higher light levels, P^B_z is noisy and ranges from 0-5 mg C mg chl^{-1} h^{-1}. Photoinhibition is difficult to discern for the full dataset, though maximum P^B_z values for individual profiles occur between 0 and 1.5 optical depths, consistent with previous analysis (Behrenfeld and Falkowski, 1997). We fit P^B_z to capture decreased photosynthetic efficiency at low light levels and the mean value at higher light levels, resulting in the final form of VRPM-SC:

$$pp_z = 2.9 \cdot chl_z \cdot d_{irr} \cdot \frac{PAR_z}{PAR_z + 2.6} \qquad (5)$$

While further parameterization of P^B_z could be attempted with the use of SST, latitude, or distance from shore, we focus on the impact of the vertical chlorophyll and PAR profiles, as outlined in the next section.

Importance of Chlorophyll and Light Profiles

The value of providing *in situ* chlorophyll and light profiles to PPAs is illustrated by incrementally improving the quality of input data to VRPM-SC. The base level of performance is that achieved with solely remote sensing inputs –

SeaWiFS chl_0 and PAR (Figure 5a). The vertical chlorophyll profile is estimated from chl_0 according to Wozniak et al. (2003) and light attenuation at depth is calculated from an empirically-derived chlorophyll dependent extinction coefficient, k_z (Parsons et al., 1984):

$$k_z = 0.04 + 0.0088 chl_z + 0.054 chl_z^{0.67} \quad (6)$$

By all metrics, model performance is slightly worse than that of VGPM-SC, but as good as or better than previously established PPAs (Table 3). This outcome is not surprising as those models include just one additional variable, SST, which does not improve model performance in the SCCS (Eppley et al., 1985; this study).

Substitution of CalCOFI chl_0 in place of SeaWiFS estimates represents the best satellite model performance achievable as remote sensing chlorophyll estimates improve, converging on perfect agreement with *in situ* data. However, comparison of Tables 2 and 3 indicates that uncertainty in satellite data is a relatively small contributor to model error, and the same holds true for VRPM-SC (Figure 5b). Total $\log_{10}$ RMSD and RMSDcp are reduced by just 2-3%, while r^2 improves marginally from 0.537 to 0.564. Additional performance gains may be possible with improved satellite PAR estimates, though they are likely to be small particularly for VGPM variants, which are inherently insensitive to PAR except at very low light levels.

In contrast to the relatively small error induced by uncertainty in chl_0, accurate representation of the chlorophyll depth profile improves model performance

significantly (Figure 5c). RMSD drops from 0.215 for PP estimates based on satellite chl_0 to 0.177 with known chlorophyll profiles – an improvement six times larger than that obtained by substituting *in situ* chl_0 for satellite data. RMSDcp and r^2 also improve dramatically, to 0.175 and 0.685 respectively, while bias remains small.

Finally, we explore model performance as influenced by uncertainty in the vertical light profile. With the addition of known PAR profiles in place of equation 6, VRPM-SC performance experiences yet another jump comparable to that achieved through inclusion of the chlorophyll profile (Figure 5d). As P^B is relatively insensitive to PAR above ~10 mol quanta m^{-2} d^{-1}, model improvements must be forced primarily by capturing light limitation at depth. RMSD and RMSDcp drop to 0.150, bias is negligible, and r^2 improves to 0.771. Accurate representation of chlorophyll and light profiles together represent a potential improvement in total model skill (RMSD) an order of magnitude greater than that possible from improved satellite chlorophyll estimates (Figure 5). Furthermore, much of the discrepancy between *in situ* and VRPM-SC PP estimates lies within the uncertainty of the *in situ* measurements. Saba et al. (2011) assumed uncertainties decreasing as a linear function of log(PP), from 50% for PP $\leq$ 50 mg C m^{-2} d^{-1} to 20% for PP $\geq$ 2000 mg C m^{-2} d^{-1}. In the best case scenario, given these uncertainties, model statistics for VRPM-SC (Figure 5d) improve to r^2=0.943 and RMSD=0.070.

The performance of satellite PPAs, relying solely on observable surface properties, is regulated by the relationship between chl_0 and PP, captured by the ESQRT model. More complex formulations employing additional parameters (SST,

PAR) offer only modest improvements in the SCCS (Kahru et al., 2009). In fact, when model performance is assessed individually for quarterly CalCOFI cruises, VGPM captures no more variance than that associated with chl_0 (Figure 6). Moderate improvement in r^2 seen when evaluation of model-data agreement extends over a year or more results from the inclusion of day length in VGPM, which captures seasonal variability in chlorophyll-specific productivity. VRPM-SC, on the other hand, is weakly influenced by the chl_0-PP relationship, and model performance is excellent on nearly all cruises (r^2>0.8 for 42 of 52 cruises, as compared to 12 of 52 for VGPM). While efforts to improve VGPM typically focus on tuning P^B_{OPT}, we find no correlation between model performance and the accuracy of P^B_{OPT} prediction (Figure 6). Accordingly, we turn our attention to improving our knowledge of vertical profiles.

Potential for Improving Chlorophyll Profiles

The potential of vertically resolved PPAs to improve productivity estimates, detailed above, is evident. However, these models suffer from one clear limitation: the scarcity of *in situ* vertical chlorophyll and PAR profiles. As a result, in large scale comparisons they demonstrate no clear performance edge over vertically integrated models (Friedrichs et al., 2009; Saba et al., 2011). Chlorophyll at depth is typically estimated from the surface value based on empirical relationships (Marra et al., 2003; Wozniak et al., 2003; Ostrowska et al., 2007), which assume a deep chlorophyll maximum accompanies low chl_0 and high surface chlorophyll is associated with a

relatively uniform vertical distribution in the surface mixed layer. While qualitative structural agreement with *in situ* data is good, discrepancies in the position or concentration of subsurface chlorophyll features influence PP estimates significantly.

In situ vertical chlorophyll profiles are sparse, though they are becoming more widely available thanks to vertical profiling floats and underwater gliders. The latter are capable of autonomous, long-range operation for several months while carrying a variety of oceanographic instruments including CTD sensors (conductivity, temperature, depth) and fluorometers. We explore here the potential of using glider data to improve PP estimates from a vertically resolved production model.

Application of glider data to PP estimates was initially constrained to glider profiles within 10 km and 10 days of CalCOFI sampling, and with available SeaWiFS match-ups. These constraints are slightly relaxed from decorrelation scales reported for the SCCS (4-8 km [Frolov et al., submitted] and 2-4 days [Abbott and Letelier, 1998; Frolov et al., submitted]) to exploit limited available data. A total of 38 CalCOFI PP stations had corresponding glider profiles within the 10 day/10 km window; locations for successful match-ups are shown in Figure 1. For this small sample we find that inclusion of glider chlorophyll profiles in VRPM-SC, in comparison to chl_0 alone, improves model performance. RMSD drops from 0.200 to 0.188 and r^2 increases from 0.52 to 0.59 (Table 5). This is a substantial portion (98% for r^2, 67% for RMSD) of the gain realized when chlorophyll is known at the exact location and depth of the productivity data, indicating the high quality of glider match-ups within the 10 km/10 day window (Figure 7). As match-up constraints are

relaxed, the power of gliders to effect positive change in model performance is reduced, though a modest improvement is seen even at time and space scales significantly longer than 10 days and 10 km. Although these gliders did not include light profiles, commercially available PAR sensors are routinely deployed on gliders and profiling floats; addition of that data would further improve the PP estimates.

Discussion

We examined properties of a 26-year primary productivity record, comprised of over 1500 stations throughout the SCCS. The ratio of integrated primary productivity to surface chlorophyll, a value of key significance for nearly all satellite PPAs (Lee et al., 1996 is one exception), correlated strongly to chl_0. The ratio of surface productivity to surface chlorophyll did not, however, indicating that the former is a proxy for variability in the vertical structure of productivity, not in phytoplankton physiology. The same appears to be true for correlations with other variables, often used in PPAs to parameterize the relationship between chl_0 and PP. These models seem to rely heavily on surface variables to represent subsurface features, and inherent limitations in that process may explain why model performance for a range of PPAs (MARRA, VGPM, and VGPM-KI) is similarly restricted. We found increased model skill with a VGPM variant relating P^B_{OPT} to chl_0 and distance from shore (Figure 3), with higher chlorophyll-specific productivity near shore presumably due to nutrient availability and phytoplankton community structure. Though improvements over existing PPAs are modest, the new model (VGPM-SC) is

a useful tool with a sound ecological basis. Its application is limited to the SCCS, but a similar approach may be valuable in other eastern boundary current systems.

Regardless of the method used to relate chl_0 to PP, satellite PPAs are inherently limited by their ignorance of vertical structure in the water column. Most of their power for PP estimation comes from the correlation of chl_0 to PP. This was noted at the outset of the satellite PP era by Eppley et al. (1985), whose observations produced the elegant but clearly limited ESQRT model, in which PP is a function of chl_0 alone. Several decades later, numerous models of varying complexity and regional specificity are available. However in the round robin comparison of Friedrichs et al. (2009), with 30 participating satellite and biogeochemical models, ESQRT was bested in total model skill (RMSD) by just one. Saba et al. (2011) found ESQRT to be among the best performing models in 5 of 10 regions across the globe. In our SCCS analysis, we find that VGPM performance is driven almost entirely by the correlation of PP and chl_0, and accurate prediction of P^B_{OPT}, the model's key physiological parameter, provides no clear improvement to PP estimates (Figure 6). It makes sense, then, that model fidelity would be enhanced more by accurate representation of the vertical structure than by further refinement of surface-based calculations. We used a very simple vertically resolved production model (VRPM-SC) to explore that point, and found that even without capturing any physiological variability (i.e. assuming P^B_z is constant unless light limited), substantially improved PP estimates are achieved by including *in situ* chlorophyll and light profiles (Figure 5).

Of course, the inherent obstacle in realizing potential gains described by Figure 5 is the provision of subsurface data. Autonomous technologies, including AUVs, profiling floats, and underwater gliders, are platforms that today are capable of that task. Gliders, first envisioned by Henry Stommel (1998), have achieved widespread use in long-range, months-long deployments. In 2011 alone, Scripps Institute of Oceanography launched Spray gliders (Sherman et al., 2001) on 45 missions, collecting a combined 3644 days (~10 years) of continuous data including over 23000 dives to depths of up to 1000 meters. A portion of those missions trace CalCOFI cruise lines, and we searched for opportunistic match-ups with CalCOFI PP casts. For 38 stations, CalCOFI and Spray data were found within 10 days and 10 km of each other. Improvements in VRPM-SC performance enabled by glider data were nearly equal to those attained using CalCOFI chlorophyll measured coincident with primary productivity, indicating the high quality of glider match-ups within the 10 day and 10 km constraints (Table 5, Figure 7). This result was not necessarily to be expected as spatial and temporal decorrelation scales reported for the SCCS are just 4-8 km (Frolov et al. submitted) and 2-4 days (Abbott and Letelier, 1998; Frolov et al., submitted), respectively.

Figure 7 illustrates the decline of glider benefit as spatial and temporal match-up constraints are relaxed. The increased model performance enabled by glider fluorescence data, as a percentage of the increase using CalCOFI chlorophyll profiles, decreases as distance between glider and PP data increases, most significantly beyond 20 km. However, even at separation distances up to 50 km, model performance is

improved by glider fluorescence profiles. Time lag between CalCOFI and glider data also limits performance gains, with a fairly consistent decline as separation increases. Beyond 40 days, inclusion of glider profiles actually resulted in worse model performance than an empirical estimation of the profile. In all cases, the gliders available for these comparisons were not equipped with PAR sensors, which appear to represent substantial potential improvement beyond that provided by fluorometers alone (Table 5). Though we were unable to assess the efficacy of glider-based PAR sensors, which must contend with operational issues such as self-shading and hull reflection, their use is not unprecedented (e.g. Rudnick et al., 2004).

An alternate platform of opportunity is the autonomous profiling float, illustrated by the global Argo program. Approximately 3000 Argo floats are deployed at any time, covering the ocean at ~3˚ resolution and performing vertical profiles of the ocean's upper 2000 m at 10-day frequency. While the core Argo measurements are temperature, salinity, and position, small numbers of "Bio-Argo" floats have been deployed with optical sensors for downward irradiance and chlorophyll-a fluorescence (Xing et al., 2011). Addition of fluorometers and PAR sensors to a greater portion of the Argo fleet could supplement and ground-truth satellite PP models, improving global productivity estimates.

While the analysis here demonstrates the feasibility of glider- or float-aided PP estimates, it is limited by our reliance on opportunistic match-ups between gliders and shipboard PP measurements. The true potential and limitation of autonomous vertical profilers in this capacity would be informed by coordinated process studies.

Similarly, determination of the optimal method to combine high vertical resolution *in situ* data with synoptic satellite surface coverage is beyond the scope of this study. Efforts of this nature have been carried out to improve the quality of subsurface chlorophyll estimation (Boss et al., 2008; Lavigne et al., 2012), and a similar effort for productivity is likely to be valuable.

The CCS, like other eastern boundary current systems, is an extremely dynamic environment, with spatially and temporally variable phytoplankton populations. Vertical chlorophyll structure at any time may reflect surface-dominated diatom blooms, vertically migrating dinoflagellates, low-light cyanobacteria, and a host of other communities. Vertically migrating species represent a particular challenge for satellites, and fundamental alteration of the PP to chl_0 ratio through changes in vertical phytoplankton distribution may accompany shifts in community structure (e.g. the 2004-2006 "age of dinoflagellates" in Monterey Bay). Moreover, empirical algorithms for estimating chlorophyll at depth have no chance of capturing unexpected subsurface features due to subduction of upwelled waters, which appears to be a common phenomenon in the CCS (Barth et al., 2002; Bograd and Mantyla, 2005). Similarly, estimation of subsurface PAR is particularly difficult in an optically complex (case 2) environment, where light attenuation is significantly influenced by constituents that do not covary with chlorophyll. In other oceanic regions, with more predictable vertical chlorophyll structure and less optical complexity, knowledge of *in situ* light and chlorophyll profiles may be of less importance and PP models may be capable of performing well with satellite data alone. Analyses similar to the one

performed here would be useful to determine the value of incorporating vertical profiles in specific regions.

Finally, even with complete knowledge of chlorophyll and light depth profiles, our ability to determine net primary productivity ultimately depends on understanding the factors governing phytoplankton growth, respiration, and mortality. Fortunately, the suite of satellite PPAs already available, through their functional forms and parameterizations, encompass an enormous body of knowledge surrounding those processes. Reducing uncertainty in subsurface chlorophyll and PAR simply enables a focus on representing those physiological effects, rather than finding proxies for vertical structure.

P^B_z	Carbon fixation rate at depth z (mg C (mg chl)$^{-1}$ hr^{-1})
P^B_{OPT}	Maximum carbon fixation rate within a water column (mg C (mg chl)$^{-1}$ hr^{-1})
$P^B_{OPT,VGPM}$	P^B_{OPT} calculated according to Behrenfeld and Falkowski [1997] (mg C (mg chl)$^{-1}$ hr^{-1})
$P^B_{OPT,CALC}$	P^B_{OPT} calculated from *in situ* PP, according to Equation 3 (mg C (mg chl)$^{-1}$ hr^{-1})
PP	Depth integrated primary productivity (mg C m^{-2} d^{-1})
PP_I	*In situ* measured PP (mg C m^{-2} d^{-1})
PP_M	Model estimated PP (mg C m^{-2} d^{-1})
pp_z	Primary productivity at depth z (mg C m^{-3} d^{-1})
pp_0	Primary productivity at depth nearest the surface (mg C m^{-3} d^{-1})
chl_z	Chlorophyll concentration at depth z (mg chl m^{-3})
chl_0	Chlorophyll concentration at depth nearest the surface (mg chl m^{-3})
d_{irr}	Day length (hr)
PAR	Photosynthetically available radiation (mol quanta m^{-2} d^{-1})
PAR_z	PAR at depth z (mol quanta m^{-2} d^{-1})
F	chl_0-specific PP (mg C m (mg chl)$^{-1}$ d^{-1})
F_0	chl_0-specific pp_0 (mg C (mg chl) d^{-1})
z_{eu}	Euphotic zone depth (m)
k_z	Optical attenuation coefficient for PAR at depth z (m^{-1})

Table 1: Notation for environmental and physiological variables.

Model	r^2	RMSD	RMSDcp	Bias
MARRA	.586	.245	.232	.080
VGPM	.586	.289	.205	.204
VGPM-KI	.566	.238	.207	.118
VGPM-SC	.620	.193	.193	.013

Table 2: Model statistics for CalCOFI stations with SeaWiFS match-ups, 2005-2010 (n=324). *In situ* chl_0 and SST and SeaWiFS PAR were used as model input.

Model	r^2	RMSD	RMSDcp	Bias
MARRA	.561	.249	.235	.083
VGPM	.555	.296	.212	.207
VGPM-KI	.514	.247	.217	.119
VGPM-SC	.585	.202	.201	.013

Table 3: Same as Table 2, but with SeaWiFS chl_0 and SST used in place of *in situ* data.

	VGPM				MARRA			
Season	**r^2**	**RMSD**	**RMSDcp**	**Bias**	**r^2**	**RMSD**	**RMSDcp**	**Bias**
Winter	.530	.312	.188	.249	.532	.258	.230	.118
Spring	.760	.293	.197	.217	.744	.247	.219	.114
Summer	.675	.271	.200	.182	.710	.205	.203	.027
Fall	.472	.263	.202	.168	.473	.231	.225	.051
All	.645	.285	.200	.203	.639	.236	.223	.076

Table 4: Seasonal performance of VGPM and MARRA models, run with *in situ* chl_0 and SST. Unlike in Tables 2 and 3, the full set of SeaWiFS-CalCOFI match-ups (1997-2010) was used to calculate statistics.

Chlorophyll Data	PAR Data	r^2	RMSD	RMSDcp	Bias
CalCOFI surface	SeaWiFS surface	.521	.200	.199	.016
Glider profile	SeaWiFS surface	.585	.188	.186	.027
CalCOFI profile	SeaWiFS surface	.586	.182	.182	.017
CalCOFI profile	CalCOFI profile	.735	.142	.141	-.015

Table 5: VRPM-SC statistics for CalCOFI stations with glider and SeaWiFS match-ups within 10 days and 10 km (n=38).

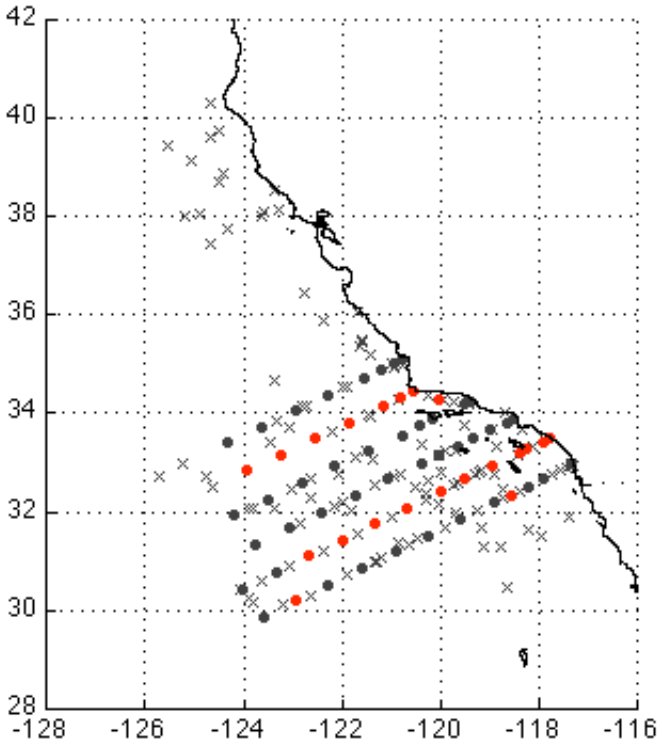

Figure 1: Map of CalCOFI primary productivity survey coverage from late 1985 to early 2011. A total of 1544 PP casts make up the dataset. Dots indicate regularly occupied stations (minimum of 5 times in this dataset, average of 22), while X's indicate stations occupied fewer than five times, typically only once or twice. Red markers denote stations identified for match-ups with Spray glider profiles.

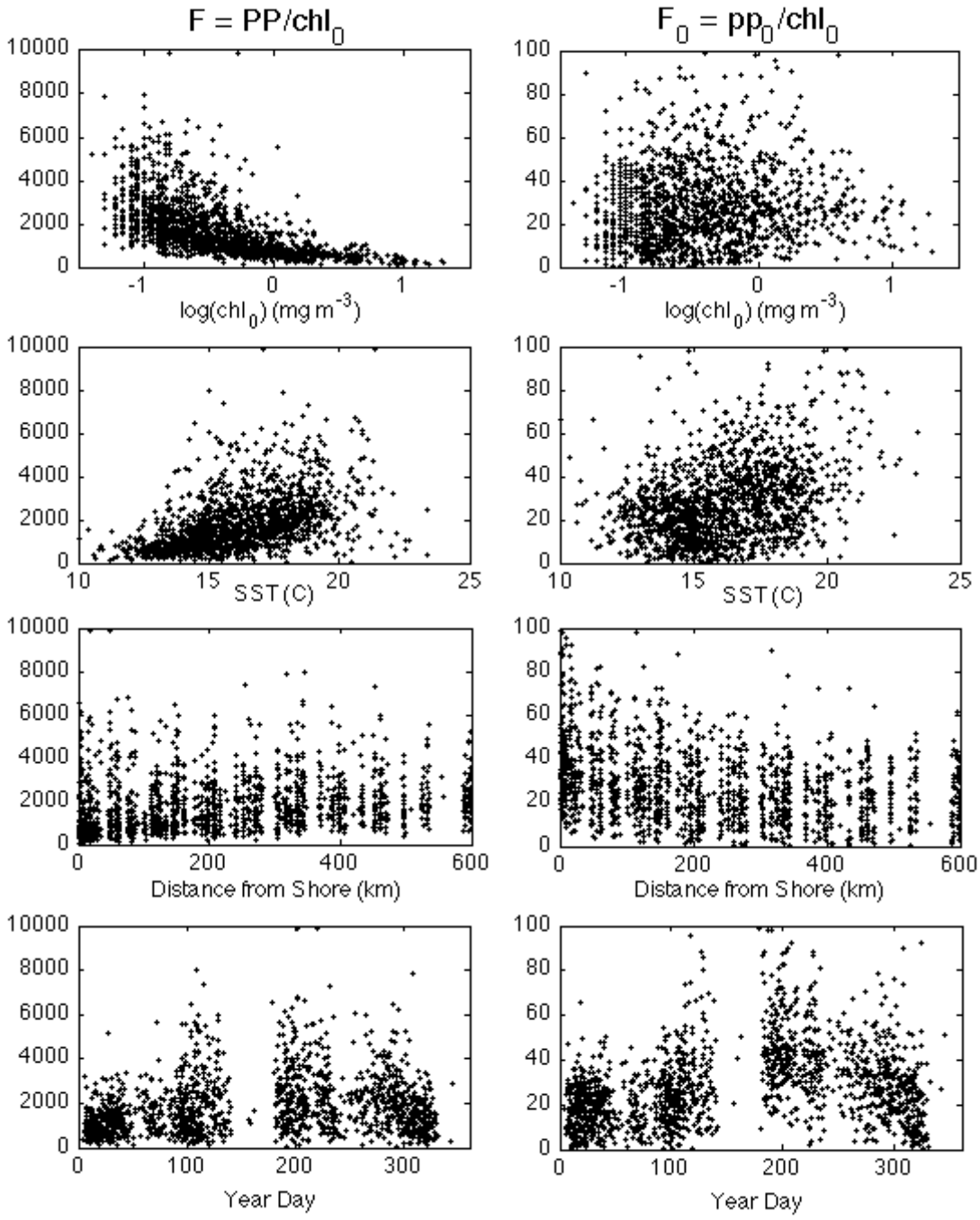

Figure 2: The ratios of integrated PP to surface chlorophyll (F, left panels) and surface PP to surface chlorophyll (F_0, right panels) are plotted against four parameters: surface chlorophyll, sea surface temperature, distance from shore, and time of year.

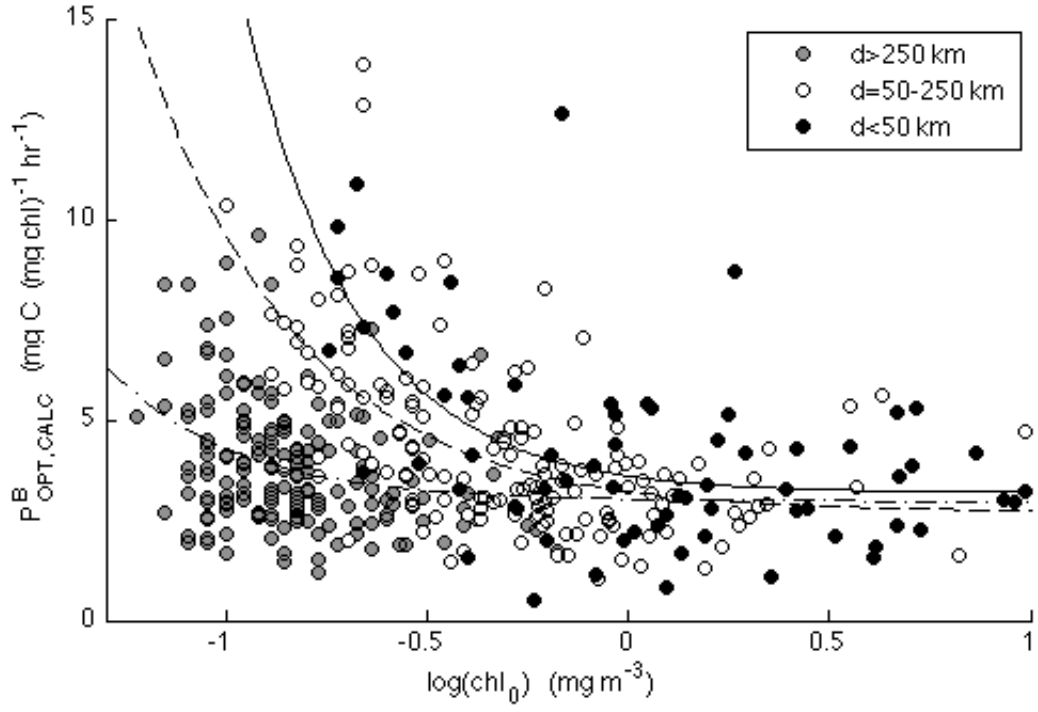

Figure 3: Calculated P^B_{OPT} values for VGPM were derived from *in situ* data according to Equation 3. Stations are divided into three regions by distance from shore, *d*. Solid, dashed, and dash-dot lines used for development of VGPM-SC are power law fits ($y=ax^b+c$) to nearshore (<50 km, a = 0.054, b = -1.38, c = 2.97), transition (50-250 km, a = 0.513, b = -1.13, c = 2.70), and offshore (>250 km, a = 0.410, b = -1.54, c = 3.19) regions, respectively. Data shown here is limited to 1997-2004, the period designated for model development.

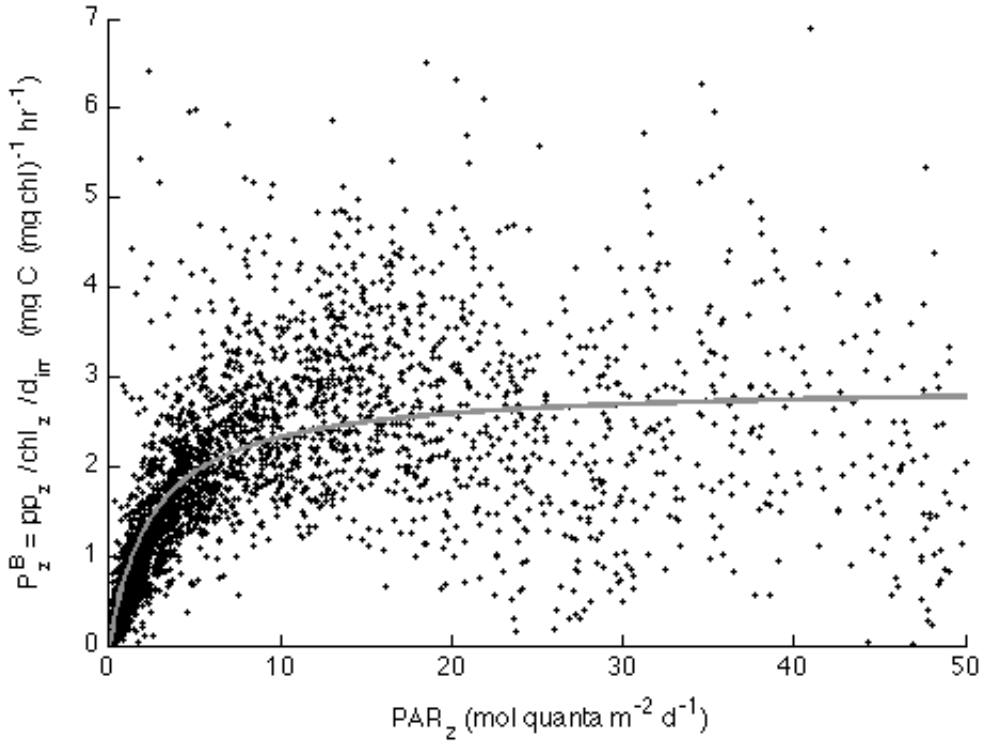

Figure 4: Dependence of photosynthetic efficiency at all depths, P^B_z, on PAR is shown for CalCOFI stations with SeaWiFS match-ups from 1997-2004. The grey line fit, used to develop the VRPM-SC algorithm, is described by $P^B_z = 2.9 \cdot PAR_z / (PAR_z + 2.6)$.

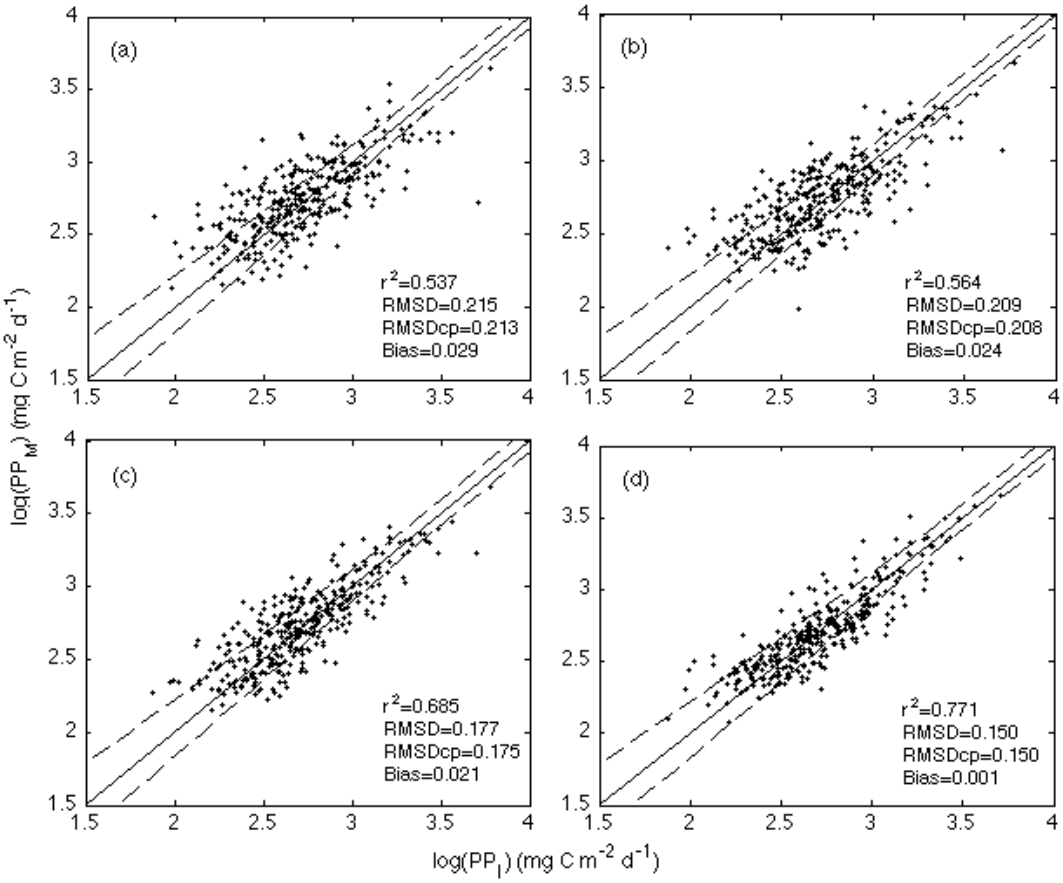

Figure 5: Dependence of VRPM-SC performance on available input data is shown for all 2005-2010 CalCOFI-SeaWiFS match-ups. In all cases, surface PAR comes from SeaWiFS. Additional inputs are (a) SeaWiFS chlorophyll and SST, (b) *in situ* surface chlorophyll and SST, (c) *in situ* chlorophyll vertical profile, (d) *in situ* chlorophyll and light profiles. Dashed lines indicate uncertainty bounds for *in situ* primary productivity measurement, estimated according to Saba et al. (2011).

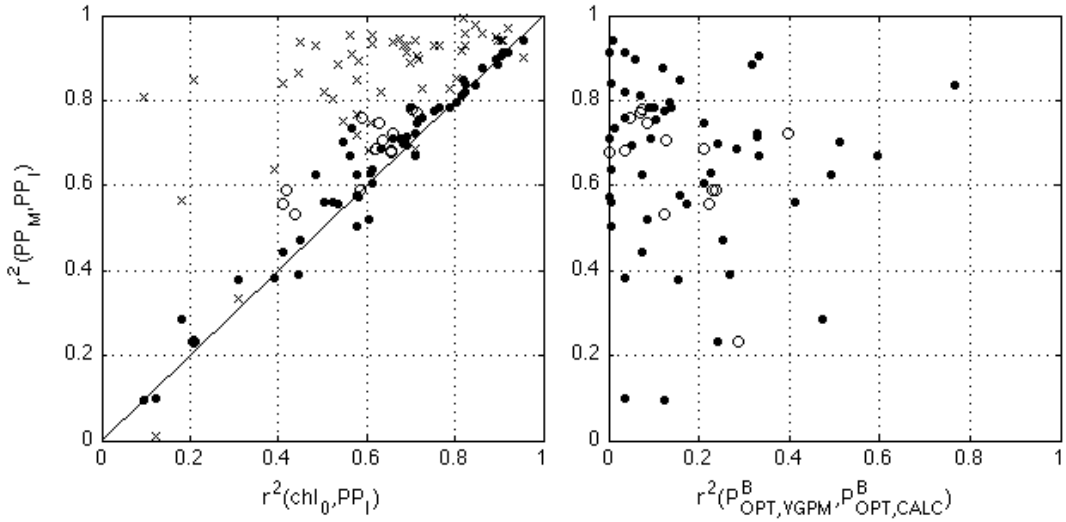

Figure 6: Impact of individual model components on PPA performance. On the horizontal axes are r^2 values for (left) surface chlorophyll correlation with PP, calculated on log-transformed variables, and (right) P^B_{OPT}, with the VGPM predicted value compared to the calculated value that would give perfect model-data agreement. In each panel, the vertical axis shows model performance as indicated by r^2 between modeled and measured PP. The model-data comparisons are calculated on each quarterly cruise for VGPM (solid dots) and VRPM-SC (X's), and on each year (1997-2010) for VGPM (open circles).

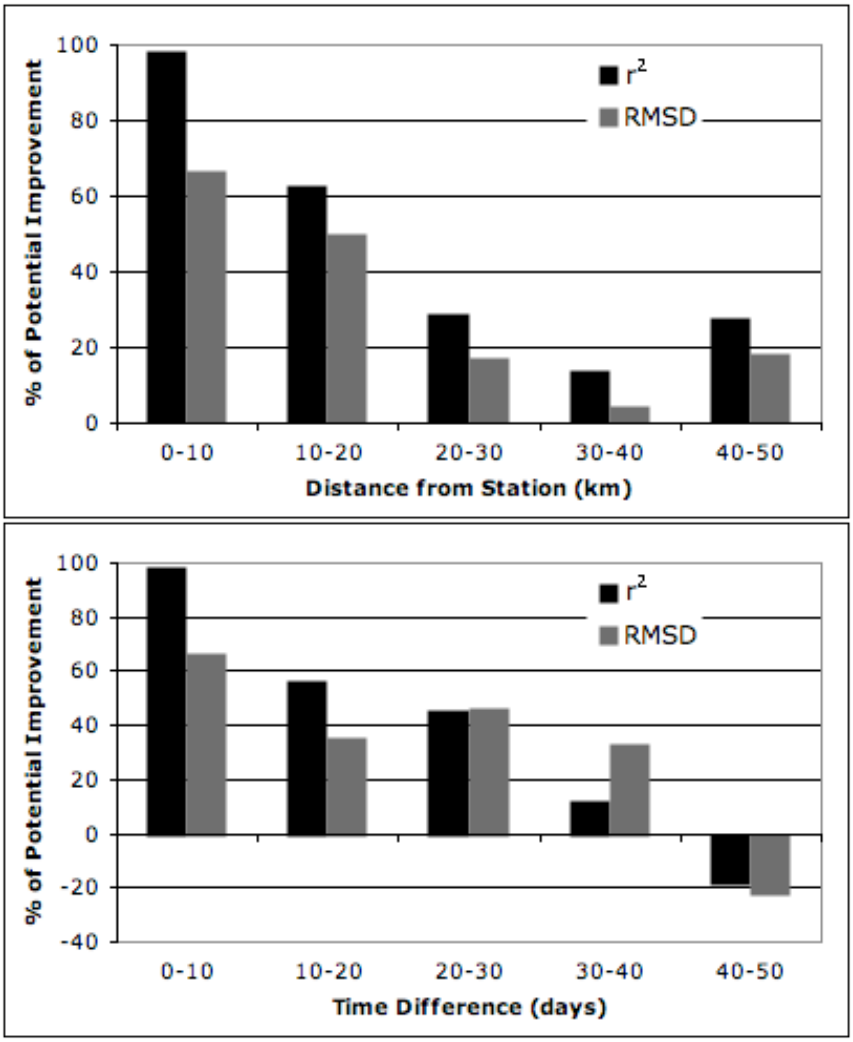

Figure 7: Efficacy of incorporating glider chlorophyll profiles to improve PP estimates is shown as a function of constraints on CalCOFI-glider match-ups. (top) Match-ups were constrained within 10 days, while distance between CalCOFI and glider data increased in 10 km increments. The numbers of match-ups in each bin were 38, 45, 55, 57, and 58, from closest to farthest. (bottom) Similarly, match-ups were constrained within 10 km, while increasing temporal disparities were considered. The numbers of match-ups in each bin, from shortest time to longest, were 38, 61, 56, 55, and 58. In each case, model improvements were measured relative to the case where only chl_0 was known, with vertical structure based on empirical relationships. The y-axis represents improvement in VRPM-SC performance achieved with glider chlorophyll profiles relative to improvement achieved with CalCOFI chlorophyll profiles (i.e. |Row2-Row1|/|Row3-Row1| in Table 5). Note that much more improvement is possible with the addition of known PAR profiles.

References

Abbott, M. R. and Letelier, R. M. (1998) Decorrelation scales of chlorophyll as observed from bio-optical drifters in the California Current, Deep Sea Research Part II, 45, 1639–1667, doi:10.1016/S0967-0645(98)80011-8.

Barth, J. A., Cowles, T. J., Kosro, P. M., Shearman, R. K., Huyer, A. and Smith, R. L. (2002) Injection of carbon from the shelf to offshore beneath the euphotic zone in the California Current, Journal of Geophysical Research, 107, C6, 3057, doi:10.1029/2001JC000956.

Behrenfeld, M. and Falkowski, P. (1997) Photosynthetic rates derived from satellite-based chlorophyll concentration, Limnology and Oceanography, 42 (1), 1–20.

Bograd, S. J. and Mantyla, A. W. (2005) On the subduction of upwelled waters in the California Current, Journal of Marine Research, 63, 863-885.

Boss, E., Swift, D., Taylor, L., Brickley, P., Zaneveld, R., Riser, S., Perry, M. and Strutton, P. (2008) Observations of pigment and particle distributions in the western North Atlantic from an autonomous float and ocean color satellite, Limnology and Oceanography, 53, 2112–2122.

Campbell, J., Antoine, D., Armstrong, R., Arrigo, K., Balch, W., Barber, R., Behrenfeld, M., Bidigare, R., Bishop, J., Carr, M.-E., Esaias, W., Falkowski, P., Hoepffner, N., Iverson, R., Kiefer, D., Lohrenz, S., Marra, J., Morel, A., Ryan, J., Vedernikov, V., Waters, K., Yentsch, C. and Yoder, J. (2002) Comparison of algorithms for estimating ocean primary production from surface chlorophyll, temperature, and irradiance, Global Biogeochemical Cycles, 16, 1035, doi:10.1029/2001GB001444.

Carr, M. E., Friedrichs, M. A. M., Schmeltz, M., Aita, M. N., Antoine, D., Arrigo, K. R., Asanuma, I., Aumont, O., Barber, R., Behrenfeld, M., Bidigare, R., Buitenhuis, E. T., Campbell, J., Ciotti, A., Dierssen, H., Dowell, M., Dunne, J., Esaias, W., Gentili, B., Gregg, W., Groom, S., Hoepffner, N., Ishizaka, J., Kameda, T., Le Quéré, C., Lohrenz, S., Marra, J., M´elin, F., Moore, K., Morel, A., Reddy, T. E., Ryan, J., Scardi, M., Smyth, T., Turpie, K., Tilstone, G., Waters, K. and Yamanaka, Y. (2006) A comparison of global estimates of marine primary production from ocean color, Deep Sea Research Part II, 53, 741–770.

Casey, K. S., Brandon, T. B., Cornillon, P. R. and Evans, R. (2010) The past, present and future of the AVHRR Pathfinder SST program, in Oceanography from Space: Revisited, eds. V. Barale, J.F.R. Gower, and L. Alberotanza, Springer. DOI: 10.1007/978-90-481-8681-5_16.

Eppley, R. (1972) Temperature and phytoplankton growth in the sea. Fisheries Bulletin, 70, 1063-1085.

Eppley, R., Steward, E., Abbott, M. and Heyman, U. (1985) Estimating ocean primary production from satellite chlorophyll: introduction to regional differences and statistics for the Southern California Bight. Journal of Plankton Research 7, 57–70.

Eppley, R. W. (1992) Chlorophyll, photosynthesis and new production in the Southern California Bight, Progress in Oceanography, 30, 117 – 150, doi:10.1016/0079-6611(92)90010-W.

Forsythe, W. C., Rykiel Jr., E. J., Stahl, R. S., Wu, H.-I. and Schoolfield, R. M. (1995) A model comparison for daylength as a function of latitude and day of year, Ecological Modeling, 80(1), 87-95.

Friedrichs, M. A. M., Carr, M.-E., Barber, R. T., Scardi, M., Antoine, D., Armstrong, R. A., Asanuma, I., Behrenfeld, M. J., Buitenhuis, E. T., Chai, F., Christian, J. R., Ciotti, A. M., Doney, S. C., Dowell, M., Dunne, J., Gentili, B., Gregg, W., Hoepffner, N., Ishizaka, J., Kameda, T., Lima, I., Marra, J., Mélin, F., Moore, J. K., Morel, A., O'Malley, R. T., O'Reilly, J., Saba, V. S., Schmeltz, M., Smyth, T. J., Tjiputra, J., Waters, K., Westberry, T. K. and Winguth, A. (2009) Assessing the uncertainties of model estimates of primary productivity in the tropical Pacific Ocean, Journal of Marine Systems, 76, 113–133.

Frolov, S., Ryan, J. P. and Chavez, F. P. (2012) Predicting euphotic-depth-integrated chlorophyll-*a* from discrete-depth and satellite-observable chlorophyll-*a* off central California, Journal of Geophysical Research, 117, C05042, doi:10.1029/2011JC007322.

Frolov, S., Kudela, R. M. and Bellingham, J. G. (submitted) Monitoring of harmful algal blooms in the era of diminishing resources: a case study of the U.S. West Coast.

Frouin, R., B. A. Franz and Werdell, P. J. (2003) The SeaWiFS PAR product, In Algorithm Updates for the Fourth SeaWiFS Data Reprocessing, ed. by S. B. Hooker and E. R. Firestone, NASA/TM-2003-206892, 22.

Kahru, M., Kudela, R. M., Manzano-Sarabia, M. and Mitchell, B. G. (2009) Trends in primary production in the California Current detected with satellite data, Journal of Geophysical Research, 114, C02004, doi:10.1029/2008JC004979.

Kahru, M., Kudela, R. M., Manzano-Sarabia, M. and Mitchell, B. G. (2012) Trends in the surface chlorophyll of the California Current: Merging data from multiple ocean color satellites, Deep Sea Research Part II in press.

Kameda, T. and Ishizaka, J. (2005) Size-fractionated primary production estimated by a two-phytoplankton community model applicable to ocean color remote sensing, Journal of Oceanography, 61, 663–672.

Lavigne, H., D'Ortenzio, F., Claustre, H. and Poteau, A. (2012) Towards a merged satellite and in situ fluorescence ocean chlorophyll product, Biogeosciences, 9, 2111–2125.

Lee, Z. P., Carder, K. L., Marra, J., Steward, R. G. and Perry, M. J. (1996) Estimating primary production at depth from remote sensing, Applied Optics, 35(3), 463–474, doi:10.1364/AO.35.000463.

Marra, J., Ho, C. and Trees, C. (2003) An alternative algorithm for the calculation of primary productivity from remote sensing data. LDEO Technical Report #LDEO-2003-1.

Morel, A. and Berthon, J. F. (1989) Surface pigments, algal biomass profiles, and potential production of the euphotic layer: Relationships reinvestigated in view of remote-sensing applications, Limnology and Oceanography, 34(8), 1545-1562.

Ostrowska, M., Majchrowski, R., Stoń-Egiert, J., Woźniak, B., Ficek, D. and Dera, J. (2007) Remote sensing of vertical phytoplankton pigment distributions in the Baltic: new mathematical expressions. Part 1: Total chlorophyll *a* distribution, Oceanologia, 49 (4), 471–489.

Parsons, T. R., Takahashi, M. and Hargrave, B. (1984) Biological Oceanographic Processes, Pregamon Press, New York: 233 pp.

Rudnick, D. L., Davis, R. E., Eriksen, C. C., Fratantoni, D. M. and Perry, M. J. (2004) Underwater gliders for ocean research, Marine Technology Society Journal, 38 (2), 73-84.

Saba, V. S., Friedrichs, M. A. M., Antoine, D., Armstrong, R. A., Asanuma, I., Behrenfeld, M. J., Ciotti, A. M., Dowell, M., Hoepffner, N., Hyde, K. J. W., Ishizaka, J., Kameda, T., Marra, J., Mélin, F., Morel, A., O'Reilly, J., Scardi, M., Smith Jr., W. O., Smyth, T. J., Tang, S., Uitz, J., Waters, K. and Westberry, T. K. (2011) An evaluation of ocean color model estimates of marine primary productivity in coastal and pelagic regions across the globe, Biogeosciences, 8, 489–503, doi:10.5194/bg-8-489-2011.

Sherman, J., Davis, R. E., Owens, W. B. and Valdes, J. (2001) The autonomous underwater glider 'Spray', IEEE Journal of Oceanic Engineering, 26, 437-446.

Stommel, H. (1989) The Slocum mission, Oceanography, 2, 22-25.

Woźniak B., Dera J., Ficek D., Majchrowski R., Ostrowska, M. and Kaczmarek S. (2003) Modelling light and photosynthesis in the marine environment, Oceanologia, 45 (2), 171–245.

Xing, X., Morel, A., Claustre, H., Antoine, D., D'Ortenzio, F., Poteau, A. and Mignot, A. (2011) Combined processing and mutual interpretation of radiometry and fluorimetry from autonomous profiling bio-Argo floats: Chlorophyll a retrieval, Journal of Geophysical Research, 116, C06020, doi:10.1029/2010JC006899.

DISSERTATION CONCLUSION

The first chapter of this dissertation represents the first comprehensive, systematic exploration into the relationship between upwelling water origins, nutrient fluxes, and physical parameters that are highly variable in space and/or time – namely the topographic slope of the continental shelf, background stratification of the water column, latitude, and wind stress magnitude. Upwelling transport was partitioned into bottom boundary layer (BBL) and interior components, distinguishing nutrient supply to the inner shelf from that to the mid- and outer-shelf, with the upwelling front dividing the two. These are two distinct biological growth regimes, with the area inshore of the upwelling front being a retentive zone and the offshore region being more susceptible to horizontal advection to the open ocean. I showed how the Burger number and its individual components (stratification, shelf slope, and Coriolis frequency) modulate upwelling source depth and fluxes from the BBL and interior, as well as the spatial extent of the inner shelf. Low Burger numbers (weak stratification and slope, high latitude) promote BBL transport over interior transport, and a wide inner shelf. The greatest source depths and nutrient fluxes are found with weak stratification and steeply sloping shelves - weak stratification enhances BBL transport and the steep shelf places deep, nutrient-rich water laterally close to shore. Model runs designed to represent specific locations in major upwelling systems showed significant qualitative and quantitative regional differences in nitrate flux. Sites off northern California and northwestern Africa, with Burger numbers of 0.43 and 0.19

respectively, had comparable nitrate fluxes that were dominated by the BBL contribution in both cases. Sites off Peru and Oregon were high Burger number sites, 1.35 and 0.95 respectively, owing to low latitude and a steep shelf off Peru and strong stratification off Oregon. Consequently, upwelled nitrate fluxes were distributed much more evenly between the interior and BBL in these cases, though the flux magnitude was an order of magnitude higher off Peru due to its lower latitude, higher wind stress, and relatively high nitrate concentration close to the surface.

As part of chapter one, I developed empirical analytical models of upwelling source depth and nitrate flux as functions of shelf slope and stratification. A further dependence on latitude and wind stress magnitude was explored briefly in chapter one and more thoroughly later along with time-varying wind stress (not shown). The forms of these analytical expressions are informative in themselves, as they shed light on the physical parameters controlling time scales for evolution of volume and tracer fluxes, as well as steady-state values that may be reached in the presence of sustained upwelling-favorable winds. However, the potential also exists for a novel and exciting application of this type of analytical model, in service of a "biologically available" upwelling index. The Coastal Upwelling Index (CUI) described by Bakun (1973) provides estimates of the volume of water upwelled along the coast based on surface atmospheric pressure fields. It is a widely-used tool, but provides information on upwelled volume only, not on the source of upwelled waters. To translate CUI to nutrient flux, one must assume some characteristic source depth for upwelling and multiply upwelled volume by nutrient concentration at that depth (Messié et al., 2009;

Macías et al., 2012). A "biologically available" upwelling index, of particular interest for studies on coastal productivity, might take into account the local stratification, latitude, topography, and characteristic nutrient profile to produce a time series of upwelled nutrients. The development and validation of such an index is complicated, but the simple analytical upwelling expressions presented here are promising.

Applications for the type of modeling investigation carried out in chapter one extend far beyond what is presented here. The current model configuration and systematic approach can be used to compare disparate regions or project changes in a region based on evolving ocean properties and atmospheric forcing. Some simple additions to the model would open up the realm of possible study even further. An oxygen component would enable investigation into bottom water ventilation and the possible development of hypoxic conditions, a growing concern in many ocean ecosystems. An iron component, concentrated near the sediments rather than distributed throughout the water column like nitrate, would allow exploration of factors controlling iron limitation, which has been observed in certain pockets of EBCs (Bruland et al., 2001). Similarly, a simple representation of phytoplankton cells could be used to examine ideal conditions for retention over the continental shelf versus advection offshore, or for reseeding of resting cysts from the sediments to the euphotic zone.

Chapter two was a logical and important extension of the work published in chapter one. The impact of a nearshore wind stress reduction (cyclonic wind stress curl) was examined, again relative to the partitioning of upwelling transport between

BBL and interior, and consequent upwelling source depth. A simple theory, formulated by extending the work of Lentz and Chapman (2004) to cases with spatially-varying bottom and surface stresses, predicts alteration of the upwelling transport through two mechanisms. The first and more significant is a local reduction of the wind-driven Ekman transport, dependent on the ratio of surface wind stress at the inner shelf boundary to the offshore value. The second is a curl-driven increase in the cross-shelf momentum flux divergence, dependent on Burger number, cross-shore position, local surface and bottom stress curls, and offshore wind stress magnitude. Both serve to increase the contribution of transport from the ocean interior while diminishing the fraction of total upwelling derived from the BBL ($\boldsymbol{R_u}$). Numerical model simulations support the theoretical estimation of changes in $\boldsymbol{R_u}$ due to wind stress curl, with extremely good model-theory agreement (R^2=0.98). Further, $\boldsymbol{R_u}$ is linearly related to upwelling source depth for a given shelf slope, with greater source depth accompanying an increased BBL transport contribution. Curl-driven changes in $\boldsymbol{R_u}$ are therefore expected to influence nutrient fluxes and resultant biological growth.

The relative importance of coastal divergence and curl-driven upwelling has been a popular topic in recent years for a number of reasons; (i) the two components may support distinct biological communities, (ii) they are likely to respond in different ways to climate trends and fluctuations, and (iii) our understanding of the near shore wind structure, especially the intensity of wind stress curl, is poor. Space-borne scatterometers have the greatest potential to provide spatial wind structure, but

nearshore data are unreliable due to coastal contamination and vary significantly among satellite products (Croquette et al., 2007). In an effort to reconcile extensive and often contradictory literature on the subject of coastal and curl-driven upwelling, I employed an idealized numerical model along with a simple upwelling theory in a mechanistic investigation of upwelling dynamics. Rather than attempt to quantify coastal and curl-driven upwelling, I conducted a study to elucidate the sensitivity of upwelling dynamics to oceanic (stratification), topographic (shelf slope), and atmospheric (wind intensity and structure) variability. Similar to chapter one, the findings of this study may be applied to regional comparisons, quantification of trends over time (e.g., due to increased stratification or coastal wind stress), or implications of improved realism in nearshore wind data products. In any case, the research of chapter two contributes to a framework within which these changes can be evaluated. Taking the admittedly simplified view that deeper source waters can potentially support more new production, factors expected to promote biological production overall are weak stratification, a steep shelf, and wind stress that remains strong close to shore. Complex relationships exist between these variables, however, and may preferentially support either the inshore (inner shelf) or offshore biological communities. Also, the 2D formulations of both the model and theory ignore important 3D effects such as eddy activity, an alonsgshore pressure gradient, and the poleward undercurrent., all of which must be considered in realistic applications.

In the final chapter of this dissertation, I explored characteristics of primary productivity (PP) in the southern CCS (SCCS), performance of existing primary

productivity algorithms (PPAs), and the potential for improving PP estimates. A thorough investigation of PP in the SCCS, and its correlation to environmental parameters, was last performed by Eppley et al. (1985). Chapter 3 updated their study with the benefit of 1544 vertically resolved PP casts obtained on 26 years of quarterly CalCOFI cruises and found some results similar to theirs. Namely, surface chlorophyll (chl_0) captures more PP variability than any other factor, there is a seasonal pattern in the ratio $F=PP/chl_0$, and SST is of limited value for improving PP estimates. Comparison of F to the ratio of surface productivity to chl_0, $Fs=PP_0/chl_0$, demonstrated that correlation between F and other parameters, particularly chl_0, is largely driven by variability in vertical phytoplankton distribution. Thus, parameterization of F with chl_0 or SST, as is commonly done in satellite PPAs, may primarily be using these variables as proxies for vertical structure rather than as indicators of phytoplankton physiology. In the SCCS, I found chlorophyll-specific growth (as indicated by Fs) to be correlated more strongly to time of year and distance from shore than SST or chl_0.

Several satellite PPAs were evaluated against in situ data and, as is generally the case in these comparisons (Friedrich et al., 2009; Kahru et al., 2009; Saba et al., 2011), I found no clear winner in terms of model skill. Furthermore, when evaluated on individual cruises, one of the most widely-used PPAs (Behrenfeld and Falkowski, 1997) correlated no better with observed PP than did chl_0. In other words, it captured no more of the data variance than that associated with chl_0. The most successful modification to the algorithm, in which chlorophyll specific productivity is a function

of chl_0 and distance from shore, resulted in modest statistical improvements over existing satellite PPAs.

The main focus of this work was a much more fertile path to improved PP estimates, specifically improved accuracy of vertical chlorophyll and light profiles. Model performance achieved with known profiles was well above any surface-based estimates, with r^2 reaching approximately 0.8 for the entire CalCOFI data set, and potentially as high as 0.94 when uncertainties in PP measurement were considered. Given that the power of chl_0 to estimate PP is much greater than any other surface variable we investigated, it makes sense that knowledge of chlorophyll at depth would vastly improve estimates of subsurface productivity, and integrated productivity by extension. Provision of accurate PAR profiles further improves PP estimates by capturing light limitation of phytoplankton growth at depth. In both cases, the CCS is a region where estimation of subsurface properties from surface data is likely to be difficult. Chlorophyll profiles are influenced by a wide range of phytoplankton communities with varying vertical distributions, including dinoflagellate species whose vertical migration may be motivated by complex combinations of light, temperature, and nutrient availability (Heaney and Eppley, 1981), and physical processes including subduction of surface blooms (Barth et al., 2002; Bograd and Mantyla, 2005). Modeling of light attenuation is also complicated in the optically complex CCS waters, where alteration of optical properties by dissolved organic matter and other constituents does not correlate to phytoplankton

abundance. My findings on the value of accurate subsurface chlorophyll and light data are therefore of particular importance in the CCS and similar systems.

In order to implement the improvements described above, I identified opportunistic match-ups between CalCOFI PP casts and autonomous underwater glider profiles, and evaluated the efficacy of glider data for improving performance of a vertically resolved production model. Glider profiles that passed within 10 km and 10 days of PP casts improved model skill nearly as much as chlorophyll measured coincident with productivity. As match-up constraints were relaxed, glider data continued to prove beneficial with separation of up to 50 km or 40 days, well beyond the SCCS decorrelation scales of 4-8 km and 2-4 days (Abbott and Letelier, 1998; Frolov et al., submitted). This finding should serve as motivation to exploit gliders, and their rapidly expanding presence, for large-scale improvements in PP estimates. Furthermore, I showed that addition of PAR sensors to the glider instrument suite significantly increases their potential utility. Measurement of PAR from gliders is not without difficulty, but has precedent and should be prioritized. Finally, synergistic use of gliders (or autonomous profiling floats such as ARGO) and satellites is of demonstrable value for subsurface chlorophyll measurement, and will no doubt prove the same for primary productivity.

References

Abbott, M. R. and Letelier, R. M. (1998) Decorrelation scales of chlorophyll as observed from bio-optical drifters in the California Current, Deep Sea Research Part II, 45, 1639– 1667, doi:10.1016/S0967-0645(98)80011-8.

Bakun, A. (1973) Coastal upwelling indices, west coast of North America, 1946–71. U.S. Department of Commerce, NOAA Technical Report NMFS–SSRF–671.

Barth, J. A., Cowles, T. J., Kosro, P. M., Shearman, R. K., Huyer, A. and Smith, R. L. (2002) Injection of carbon from the shelf to offshore beneath the euphotic zone in the California Current, Journal of Geophysical Research, 107, C6, 3057, doi:10.1029/2001JC000956.

Behrenfeld, M. and Falkowski, P. (1997) Photosynthetic rates derived from satellite-based chlorophyll concentration, Limnology and Oceanography, 42 (1), 1–20.

Bograd, S. J. and Mantyla, A. W. (2005) On the subduction of upwelled waters in the California Current, Journal of Marine Research, 63, 863-885.

Bruland, K. W., Rue, E. L. and Smith, G. J. (2001) Iron and macronutrients in California coastal upwelling regimes: Implications for diatom blooms, Limnololgy and Oceanography, 46, 1661–1674.

Croquette, M., Eldin, G., Grados, C. and Tamayo, M. (2007) On differences in satellite wind products and their effects in estimating coastal upwelling processes in the south-east Pacific, Geophysical Research Letters, 34, L11608, doi:10.1029/2006GL027538.

Eppley, R., Steward, E., Abbott, M. and Heyman, U. (1985) Estimating ocean primary production from satellite chlorophyll: introduction to regional differences and statistics for the Southern California Bight. Journal of Plankton Research, 7, 57–70.

Friedrichs, M. A. M., Carr, M.-E., Barber, R. T., Scardi, M., Antoine, D., Armstrong, R. A., Asanuma, I., Behrenfeld, M. J., Buitenhuis, E. T., Chai, F., Christian, J. R., Ciotti, A. M., Doney, S. C., Dowell, M., Dunne, J., Gentili, B., Gregg, W., Hoepffner, N., Ishizaka, J., Kameda, T., Lima, I., Marra, J., Mélin, F., Moore, J. K., Morel, A., O'Malley, R. T., O'Reilly, J., Saba, V. S., Schmeltz, M., Smyth, T. J., Tjiputra, J., Waters, K., Westberry, T. K. and Winguth, A. (2009) Assessing the uncertainties of model estimates of primary productivity in the tropical Pacific Ocean, Journal of Marine Systems, 76, 113–133.

Frolov, S., Kudela, R. M., and Bellingham, J. G. (submitted) Monitoring of harmful

algal blooms in the era of diminishing resources: a case study of the U.S. West Coast.

Heaney, S. I. and Eppley, R. W. (1981) Light, temperature, and nitrogen as interacting factors affecting diel vertical migrations of dinoflagellates in culture, Journal of Plankton Research, 3 (2), 331-344, doi:10.1093/plankt/3.2.331.

Kahru, M., Kudela, R. M., Manzano-Sarabia, M. and Mitchell, B. G. (2009) Trends in primary production in the California Current detected with satellite data, Journal of Geophysical Research, 114, C02004, doi:10.1029/2008JC004979.

Lentz, S. J. and Chapman, D. C. (2004) The importance of non-linear cross-shelf momentum flux during wind-driven coastal upwelling, Journal of Physical Oceanography, 34, 2444–2457.

Macías, D., Franks, P. J. S., Ohman, M. D. and Landry, M. R. (2012) Modeling the effects of coastal wind- and wind–stress curl-driven upwellings on plankton dynamics in the Southern California current system, Journal of Marine Systems, Volume 94, 107-119, doi:10.1016/j.jmarsys.2011.11.011.

Messié, M., Ledesma, J., Kolber, D. D., Michisaki, R. P., Foley, D. G. and Chavez, F. P. (2009) Potential new production estimates in four eastern boundary upwelling ecosystems, Progress in Oceanography, 83, 151–158, doi:10.1016/j.pocean.2009.07.018.

Saba, V. S., Friedrichs, M. A. M., Antoine, D., Armstrong, R. A., Asanuma, I., Behrenfeld, M. J., Ciotti, A. M., Dowell, M., Hoepffner, N., Hyde, K. J. W., Ishizaka, J., Kameda, T., Marra, J., Mélin, F., Morel, A., O'Reilly, J., Scardi, M., Smith Jr., W. O., Smyth, T. J., Tang, S., Uitz, J., Waters, K. and Westberry, T. K. (2011) An evaluation of ocean color model estimates of marine primary productivity in coastal and pelagic regions across the globe, Biogeosciences, 8, 489–503, doi:10.5194/bg-8-489-2011.